

# Strain engineering and epitaxial stabilization of halide perovskites

<https://doi.org/10.1038/s41586-019-1868-x>

Received: 12 April 2019

Accepted: 19 November 2019

Published online: 8 January 2020

Yimu Chen<sup>1,8</sup>, Yusheng Lei<sup>1,8</sup>, Yuheng Li<sup>1</sup>, Yugang Yu<sup>2</sup>, Jinze Cai<sup>2</sup>, Ming-Hui Chiu<sup>3</sup>, Rahul Rao<sup>4</sup>, Yue Gu<sup>2</sup>, Chunfeng Wang<sup>1</sup>, Woojin Choi<sup>5</sup>, Hongjie Hu<sup>2</sup>, Chonghe Wang<sup>1</sup>, Yang Li<sup>1</sup>, Jiawei Song<sup>2</sup>, Jingxin Zhang<sup>2</sup>, Baiyan Qi<sup>2</sup>, Muyang Lin<sup>1</sup>, Zhuorui Zhang<sup>1</sup>, Ahmad E. Islam<sup>4</sup>, Benji Maruyama<sup>4</sup>, Shadi Dayeh<sup>1,2,5</sup>, Lain-Jong Li<sup>3,6</sup>, Kesong Yang<sup>1</sup>, Yu-Hwa Lo<sup>2,5</sup> & Sheng Xu<sup>1,2,5,7\*</sup>

Strain engineering is a powerful tool with which to enhance semiconductor device performance<sup>1,2</sup>. Halide perovskites have shown great promise in device applications owing to their remarkable electronic and optoelectronic properties<sup>3–5</sup>. Although applying strain to halide perovskites has been frequently attempted, including using hydrostatic pressurization<sup>6–8</sup>, electrostriction<sup>9</sup>, annealing<sup>10–12</sup>, van der Waals force<sup>13</sup>, thermal expansion mismatch<sup>14</sup>, and heat-induced substrate phase transition<sup>15</sup>, the controllable and device-compatible strain engineering of halide perovskites by chemical epitaxy remains a challenge, owing to the absence of suitable lattice-mismatched epitaxial substrates. Here we report the strained epitaxial growth of halide perovskite single-crystal thin films on lattice-mismatched halide perovskite substrates. We investigated strain engineering of  $\alpha$ -formamidinium lead iodide ( $\alpha$ -FAPbI<sub>3</sub>) using both experimental techniques and theoretical calculations. By tailoring the substrate composition—and therefore its lattice parameter—a compressive strain as high as 2.4 per cent is applied to the epitaxial  $\alpha$ -FAPbI<sub>3</sub> thin film. We demonstrate that this strain effectively changes the crystal structure, reduces the bandgap and increases the hole mobility of  $\alpha$ -FAPbI<sub>3</sub>. Strained epitaxy is also shown to have a substantial stabilization effect on the  $\alpha$ -FAPbI<sub>3</sub> phase owing to the synergistic effects of epitaxial stabilization and strain neutralization. As an example, strain engineering is applied to enhance the performance of an  $\alpha$ -FAPbI<sub>3</sub>-based photodetector.

$\alpha$ -FAPbI<sub>3</sub> is epitaxially grown on a series of mixed methylammonium lead chloride/bromide (MAPbCl<sub>x</sub>Br<sub>3-x</sub>) single crystalline substrates by the inverse temperature growth method<sup>16</sup>. The resulting MAPbCl<sub>x</sub>Br<sub>3-x</sub> substrates, with different compositional ratios and thus lattice parameters, are grown by solutions with different Cl/Br precursor molar ratios (Supplementary Fig. 1)<sup>17</sup>. We note that the strain in the epilayer is determined not only by the lattice mismatch, but also by the relaxation mechanisms. Lattice distortion relaxes the strain, so the region near the heteroepitaxy interface has the highest strain, which gradually drops at regions distant from the interface. The total elastic strain energy increases as the film grows thicker, until it eventually crosses the threshold energy for structural defect generation, and dislocations will form to partially relieve the misfit<sup>18</sup>. A slow growth rate of the epilayer is chosen, as a higher rate will increase the defect concentration in the epilayer. The crystalline quality of the substrates is carefully optimized, as the defects in the substrates can propagate into the epilayer (Extended Data Fig. 1).

Heteroepitaxial growth leads to controllable film thickness, preferential growth sites and orientations, compatible fabrication protocols

with existing infrastructures and scalable large-area device applications. Figure 1a shows optical images of a series of MAPbCl<sub>x</sub>Br<sub>3-x</sub> substrates with a layer of epitaxial  $\alpha$ -FAPbI<sub>3</sub> film on the top. The epilayer has a uniform thickness with a well defined film–substrate interface (Fig. 1b). The film topography can reveal the growth mechanism and sometimes the defects caused by strain relaxation. On the one hand, a sub-100 nm  $\alpha$ -FAPbI<sub>3</sub> thin film shows a clear interface (Fig. 1b), and a well defined terrain morphology, with a step height close to the size of a  $\alpha$ -FAPbI<sub>3</sub> unit cell, indicating layer-by-layer growth behaviour of the epitaxial  $\alpha$ -FAPbI<sub>3</sub> (Extended Data Fig. 2a, b). A 10- $\mu$ m film, on the other hand, shows non-conformal growth, indicating strain relaxation by dislocation formation (Extended Data Fig. 2c, d).

The crystallographic relationships between the MAPbCl<sub>x</sub>Br<sub>3-x</sub> substrates and the epitaxial  $\alpha$ -FAPbI<sub>3</sub> thin films are illustrated by high-resolution X-ray diffraction (XRD) (Fig. 1c). In their freestanding form, both  $\alpha$ -FAPbI<sub>3</sub> and MAPbCl<sub>x</sub>Br<sub>3-x</sub> have a cubic structure<sup>19,20</sup>. The lattice parameters of freestanding  $\alpha$ -FAPbI<sub>3</sub> and MAPbCl<sub>x</sub>Br<sub>3-x</sub> substrates (both with *Pm3m* space group) are calculated to be 6.35 Å (Supplementary Fig. 1) and 5.83–5.95 Å, respectively. The ratio *x* for each

<sup>1</sup>Department of Nanoengineering, University of California San Diego, La Jolla, CA, USA. <sup>2</sup>Materials Science and Engineering Program, University of California San Diego, La Jolla, CA, USA.

<sup>3</sup>Physical Science and Engineering Division, King Abdullah University of Science and Technology, Thuwal, Saudi Arabia. <sup>4</sup>Materials and Manufacturing Directorate, Air Force Research Laboratory, Wright Patterson Air Force Base, Dayton, OH, USA. <sup>5</sup>Department of Electrical and Computer Engineering, University of California San Diego, La Jolla, CA, USA. <sup>6</sup>School of Materials Science and Engineering, University of New South Wales, Sydney, New South Wales, Australia. <sup>7</sup>Department of Bioengineering, University of California San Diego, La Jolla, CA, USA. <sup>8</sup>These authors contributed equally: Yimu Chen, Yusheng Lei. \*e-mail: shengxu@ucsd.edu

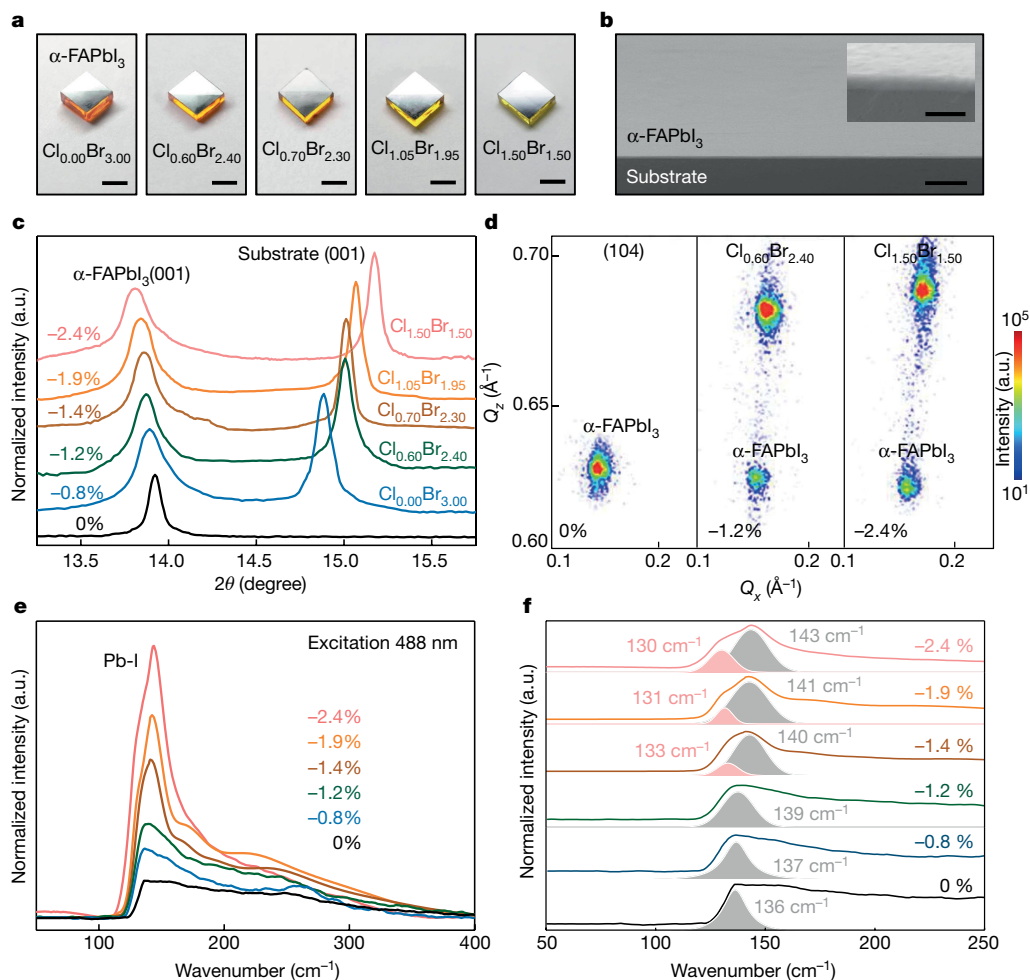


**Fig. 1 | Epitaxial  $\alpha$ -FAPbI<sub>3</sub> thin films and structural characterizations.**

**a**, Optical images of the as-grown epitaxial  $\alpha$ -FAPbI<sub>3</sub> thin films. The high transparency of the substrates and the smooth surfaces of the thin films demonstrate their high quality. Scale bars, 4 mm. **b**, A cross-sectional scanning electron microscope (SEM) image of the epitaxial thin film with controlled uniform thickness. Scale bar, 2  $\mu\text{m}$ . Inset, magnified SEM image of the heterostructure showing a well defined interface. Scale bar, 200 nm. **c**, High-resolution XRD  $\omega - 2\theta$  scan of the (001) peaks of the epitaxial samples on different substrates showing the increasing tetragonality with increasing lattice mismatch. **d**, Reciprocal space mapping with (104) asymmetric reflection of the  $\alpha$ -FAPbI<sub>3</sub> for different lattice mismatches with the substrate. The results show a decrease in the in-plane lattice parameter as well as an

increase in the out-of-plane lattice parameter with larger compressive strain.  $Q_x$  and  $Q_z$  are the in-plane and out-of-plane reciprocal space coordinates. **e**, Confocal Raman spectra of the epitaxial layer at different strains. We attribute the evolution of the shape and intensity of the peak with strain to the increase in lattice tetragonality under higher strain. We note that the broad peak at approximately 250  $\text{cm}^{-1}$  is attributed to the Pb-O bond induced by laser oxidation. **f**, Fitting analysis of the Raman peaks. The peak at 136  $\text{cm}^{-1}$  from the strain-free sample (black line) is attributed to the Pb-I bond. With increasing compressive strain, the peak gradually blueshifts as the bond becomes more rigid, and finally splits into a main peak that blueshifts (owing to in-plane bond contraction) and a shoulder peak that redshifts (owing to out-of-plane bond extension). (a.u., arbitrary units).

composition is then calculated to be 0–1.50, according to the Vegard's Law (Supplementary Table 1). As  $x$  increases, the MAPbCl <sub>$x$</sub> Br <sub>$3-x$</sub>  (001) peaks shift to a higher  $2\theta$  angle, indicating a decrease in the lattice parameters of the substrate and therefore an increase in the lattice mismatch (Fig. 1c and Supplementary Table 2). Meanwhile, the  $\alpha$ -FAPbI<sub>3</sub> (001) peak shifts to a lower  $2\theta$  angle, indicating an increase in the out-of-plane lattice parameter as the in-plane compressive strain increases. When  $x$  exceeds 1.50, the strain energy dramatically increases, and the epitaxial growth becomes less thermodynamically favourable.  $\alpha$ -FAPbI<sub>3</sub> then randomly crystallizes on the substrate (Supplementary Fig. 2). Peak broadening of the epitaxial  $\alpha$ -FAPbI<sub>3</sub> is therefore induced by the epitaxial strain and the reduction in film thickness, instead of by the strain-induced dislocations or the strain relaxation (Supplementary Fig. 3). Figure 1d shows the reciprocal space mapping of strain-free and strained  $\alpha$ -FAPbI<sub>3</sub> thin films with different lattice mismatch with the substrate. An increase of tetragonality of the lattice is evident as the compressive strain increases.

The corresponding strain levels of the  $\alpha$ -FAPbI<sub>3</sub> in those three cases are calculated to be 0%, -1.2% and -2.4%, respectively, on the basis of the lattice distortion (where the negative sign denotes compressive strain). The Poisson's ratio is determined to be around 0.3, which is consistent with the reported value<sup>21</sup>.

We also studied the structure of  $\alpha$ -FAPbI<sub>3</sub> at different strains (between 0% and -2.4%, on different substrates) by Raman spectroscopy (Fig. 1e). Control experiments exclude any Raman signals from the substrates (Supplementary Fig. 4). The peak at around 136  $\text{cm}^{-1}$  in Fig. 1e, which originated from the stretching of the lead-iodine bond<sup>22</sup>, increases in intensity and broadens in width as the strain increases. The cubic structure of the strain-free  $\alpha$ -FAPbI<sub>3</sub> is less Raman-active, and the detectable signal is usually broad and weak. When in-plane compressive strain increases, the inorganic framework gradually gains tetragonality and produces a stronger Raman signal with a clearly distinguishable shape. Interestingly, at around -1.4% strain, the peak at 136  $\text{cm}^{-1}$  starts to split into two: a main peak at about 140  $\text{cm}^{-1}$  and a

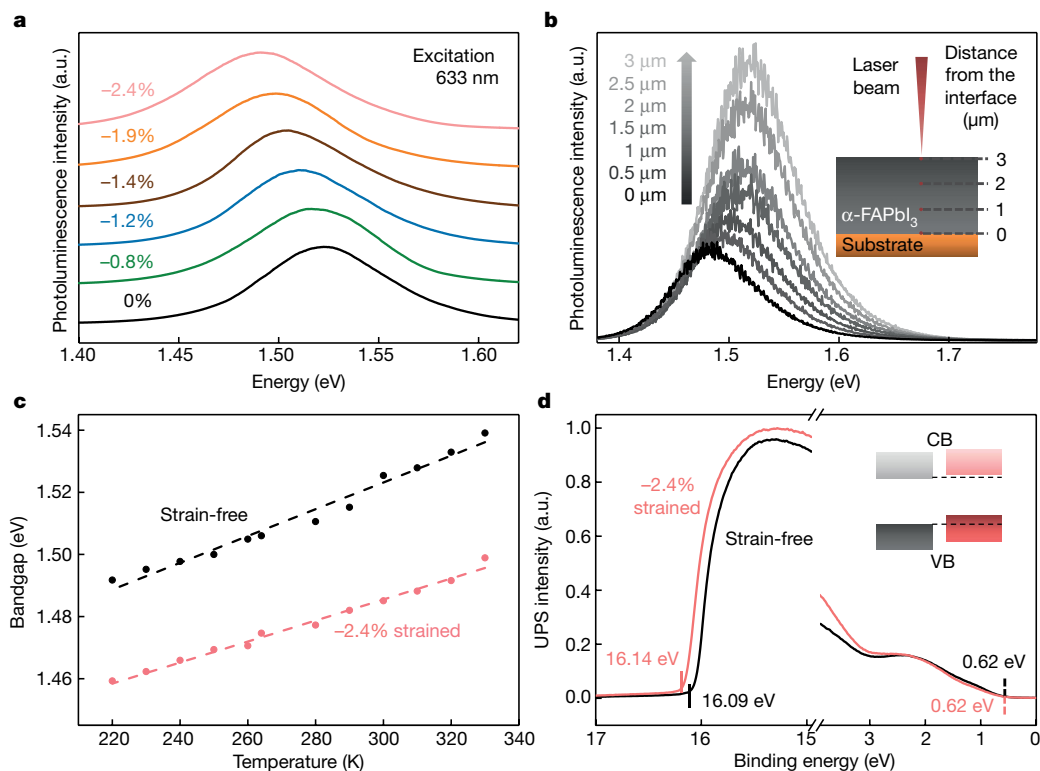


**Fig. 2 | Optical properties.** **a**, Photoluminescence spectra of  $\alpha$ -FAPbI<sub>3</sub> at different strains. The redshift of the photoluminescence peak with increasing strain is due to bandgap reduction under compressive strain, consistent with the first-principles calculations. **b**, Focal-point-dependent confocal photoluminescence spectra of a 3- $\mu$ m-thick film. When the focal point of the laser (indicated by the red point in the schematic; inset) moves towards the epitaxial interface, the photoluminescence emission peak shifts from about 1.523 eV to about 1.479 eV, owing to the large compressive strain close to the interface. **c**, Temperature-dependent photoluminescence spectra of a -2.4% strained and a strain-free sample. The bandgap of the strain-free sample shows

a stronger temperature dependence than the strained sample, indicating that the substrate can reduce the lattice deformation that is caused by the temperature change. **d**, UPS spectra of a -2.4% strained and a strain-free sample. The Fermi level and the VBM of the samples can be extracted from the intersections of the curves with the horizontal axis, marked by the solid and dashed vertical lines, respectively. The results reveal that compressive strain increases the VBM more than it does the CBM, owing to the enhanced interaction of lead 6s and iodine 5p orbitals under the compressive strain. Inset, the schematic band diagram of the -2.4% strained and strain-free samples. CB, conduction band; VB, valence band.

shoulder at about 133 cm<sup>-1</sup> (Fig. 1f). When the strain is further increased to -2.4%, these two peaks shift to 143 cm<sup>-1</sup> and 130 cm<sup>-1</sup>, respectively. We attribute the blueshift of the main peak to the compression of the in-plane lead-iodine bond, and the redshift of the shoulder peak to the stretching of the out-of-plane lead-iodine bond. This result is also supported by the simulated Raman spectra by first-principles calculations (Supplementary Fig. 4c, d). We also studied the Raman spectra of  $\alpha$ -FAPbI<sub>3</sub> of various thicknesses on MAPbCl<sub>1.50</sub>Br<sub>1.50</sub> (Supplementary Fig. 4f). The results are consistent: a strong, sharp peak is detected from a sub-100-nm film with -2.4% strain, and a weak, broad peak is detected from a film of around 2  $\mu$ m, where the misfit strain is relaxed near the film surface.

Photoluminescence spectra (Fig. 2a) reveal changes in the bandgap of sub-100-nm epitaxial  $\alpha$ -FAPbI<sub>3</sub> thin films under different strains (between 0% and -2.4%, on different substrates). The photoluminescence peak of  $\alpha$ -FAPbI<sub>3</sub> gradually shifts from about 1.523 eV at 0% strain to about 1.488 eV at -2.4% strain, corresponding to a reduction of about 35 meV in the bandgap. We exclude the possible contributions to this photoluminescence redshift from thickness-dependent bandgap<sup>23,24</sup>, reabsorption<sup>25</sup> or halide migration<sup>26</sup> (detailed discussions in the Supplementary Information). The bandgap change is consistent with the first-principles calculations and absorption measurements (Extended Data Fig. 3). The photoluminescence peak in Fig. 2a also broadens with increasing strain (Supplementary Fig. 5), which is not due to possible charge transfer between the epitaxial  $\alpha$ -FAPbI<sub>3</sub> and the substrate (Supplementary Fig. 6).

Temperature-dependent photoluminescence studies suggest that the emission peak broadening originates from the reduced crystalline quality and the enhanced carrier-phonon coupling under the strain (Extended Data Fig. 4).

Additionally, we studied confocal photoluminescence spectra at different locations in an  $\alpha$ -FAPbI<sub>3</sub> film of around 3  $\mu$ m on a substrate of MAPbCl<sub>1.50</sub>Br<sub>1.50</sub> (Fig. 2b). The photoluminescence peak shifts from about 1.479 eV when the laser is focused at the interface where the local strain is high, to about 1.523 eV at 3  $\mu$ m from the interface where the strain is relaxed. As a control, the photoluminescence redshift in a strain-free sample is less obvious (from about 1.516 eV to about 1.523 eV, Supplementary Fig. 7a), which is attributed to reabsorption<sup>25</sup>. In the strained sample, we exclude elastic relaxation although halide perovskites are much softer than conventional semiconductors<sup>27</sup>. Our finite element analysis simulation results show that the elastic relaxation for a 3- $\mu$ m-thick  $\alpha$ -FAPbI<sub>3</sub> thin film is negligible: only around 0.09% (Supplementary Fig. 8). Thickness-dependent in-plane XRD is used to study the critical thickness at which the strain will start to be plastically relaxed (Extended Data Fig. 5). The results show that the critical thickness is much less than the thickness we used in this study and, therefore, the relaxation can be attributed to plastic relaxation by the formation of dislocations. Photoluminescence measurements from samples of different thicknesses show a similar trend (Supplementary Fig. 9), indicating that the strain is relaxed by dislocations when the film grows thicker. Temperature-dependent photoluminescence studies indicate that the bandgap of  $\alpha$ -FAPbI<sub>3</sub>

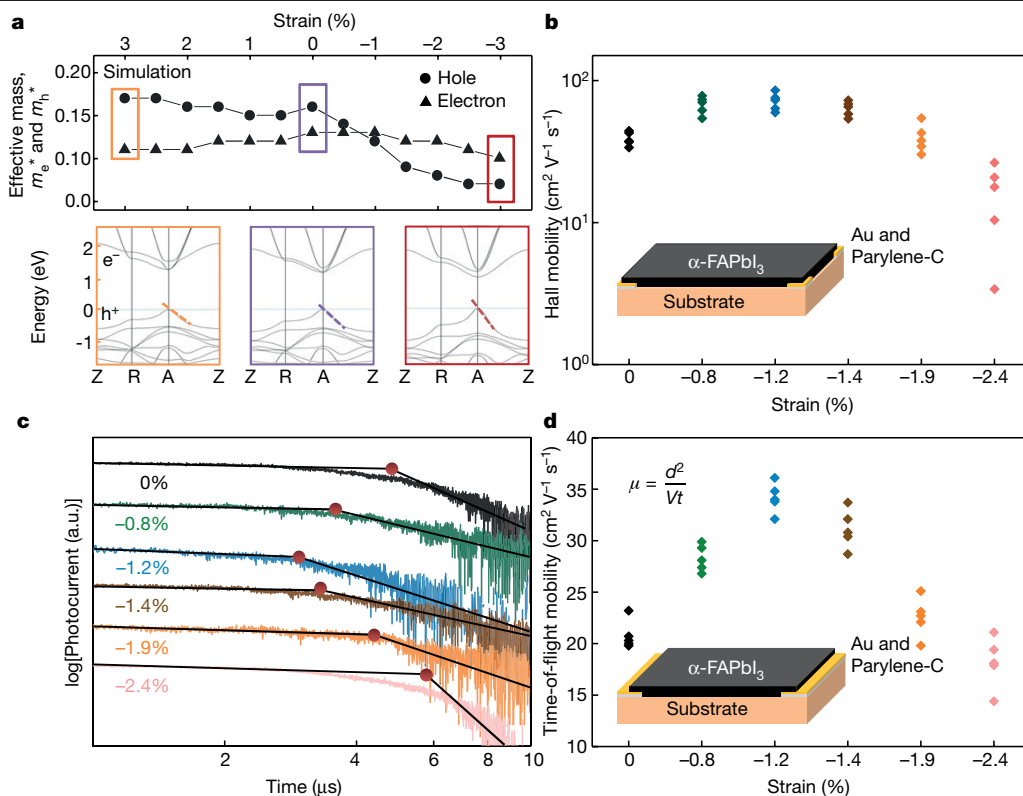


**Fig. 3 | Electronic properties.** **a**, Calculated effective masses of the carriers at different strains, and electronic bandstructures under three strain levels (3%, 0% and -3%). The electron effective mass ( $m_e^*$ ) remains relatively stable with the change in strain, while the hole effective mass ( $m_h^*$ ) decreases with increasing compressive strain. The dashed lines represent the dispersivity of the valence band; a less dispersive valence bandstructure indicates a smaller hole effective mass. The Z, R and A points are high-symmetry points in the first Brillouin zone of the tetragonal lattice. Bottom panels with coloured borders represent three typical examples with different strains. **b**, Hole mobilities by Hall effect measurements showing that  $\alpha$ -FAPbI<sub>3</sub> with strain of -1.2% has the highest hole mobility. Coloured symbols correspond to the strain as in **c**. The decrease of the hole mobility with strain higher than -1.2% is attributed to the increase of dislocation density. Number of experiments,  $n = 5$  for each strain. Inset, the

structure of the measurement setup (gold, yellow; parylene-C, grey), not to scale. **c**, Transient photocurrent curves of the epitaxial  $\alpha$ -FAPbI<sub>3</sub> under different strains. The transient photocurrent curves are plotted on a log-log scale. The carrier transit time—that is, the inflection point of the photocurrent curve—is marked by a solid red circle. The inflection point indicates the point at which the charge transport carriers switch from the majority to the minority carriers. Lines are guides to the eye. **d**, Plots of calculated carrier mobilities as a function of the strain magnitudes. The inset equation,  $\mu = d^2/Vt$ , transforms the carrier transit time to the carrier mobility, where  $\mu$  is the calculated time-of-flight carrier mobility,  $d$  is the target region thickness,  $V$  is the applied voltage and  $t$  is the measured carrier transit time. Number of experiments,  $n = 5$  for each strain. Inset, schematic measurement setup. Coloured symbols correspond to the strain as in **c**.

under both 0% and -2.4% strain shows a strong temperature dependence, owing to the soft nature of  $\alpha$ -FAPbI<sub>3</sub> (Fig. 2c and Extended Data Fig. 4)<sup>7</sup>. The strained-sample bandgap is less temperature-dependent compared to that of the strain-free sample, because the smaller thermal expansion coefficient of the substrate compared to the epitaxial layer introduces a constraint<sup>28</sup> (detailed discussions in the Supplementary Information).

Ultraviolet photoelectron spectroscopy (UPS) reveals the bandstructure evolution of the  $\alpha$ -FAPbI<sub>3</sub> under strain (see Fig. 2d for 0% and -2.4% strain and Extended Data Fig. 6 for other strains). All samples exhibit p-type behaviour (see Supplementary Information for more details). The Fermi level and the valence-band maximum (VBM) of the samples can be extracted from the UPS data. The results show that strain of -2.4% lifts the VBM upward by about 50 meV compared to the strain-free scenario. Considering the change in the bandgap (about 35 meV, Fig. 2a), the -2.4% strain pushes the conduction-band minimum (CBM) upward by about 15 meV compared to the strain-free scenario. The VBM mainly consists of lead 6s and iodine 5p orbitals, and the enhanced coupling between these orbitals under compressive strain pushes the VBM upward<sup>29</sup>. The CBM, which consists mostly of nonbonding localized states of Pb *p* orbitals, is less sensitive to the deformation of the PbI<sub>6</sub> octahedrons<sup>7</sup>. Therefore, the in-plane compressive strain increases the VBM more than it does the CBM.

The lattice deformation can alter the electronic bandstructure and therefore also the carrier dynamics. The effective mass of charge carriers can be assessed by the band curvature extracted from first-principles calculations<sup>30</sup>. Figure 3a shows the calculated results of the electron effective mass,  $m_e^*$ , and hole effective mass,  $m_h^*$  (the top panel) and three typical electronic bandstructures (the bottom panels) under different strains. On the one hand, the  $E$ - $k$  dispersion of the conduction band remains relatively unaltered, and  $m_e^*$  shows only a slight variation under strain between 3% and -3%. On the other hand, compressive strain can modulate the  $E$ - $k$  dispersion of the valence band and considerably reduce  $m_h^*$ .

To validate these calculations, Hall effect carrier mobilities of the  $\alpha$ -FAPbI<sub>3</sub> thin films under strain of between 0% and -2.4% are measured (Fig. 3b). Finite element analysis simulation results show that potential carrier transfer from the substrate to the epitaxial layer is negligible, owing to an insulating layer (Parylene-C) and the energy barrier between the epitaxial layer and the substrate (Supplementary Fig. 10). All samples measured by the Hall effect show a p-type character, which is consistent with the UPS results. Of all strain levels tested, films under -1.2% strain on a MAPbCl<sub>0.60</sub>Br<sub>2.40</sub> substrate have the highest hole mobility (Fig. 3b). Further increasing the strain results in a drastic drop in the hole mobility, because of the higher dislocation densities that arise at higher strain levels. We note that the devices for



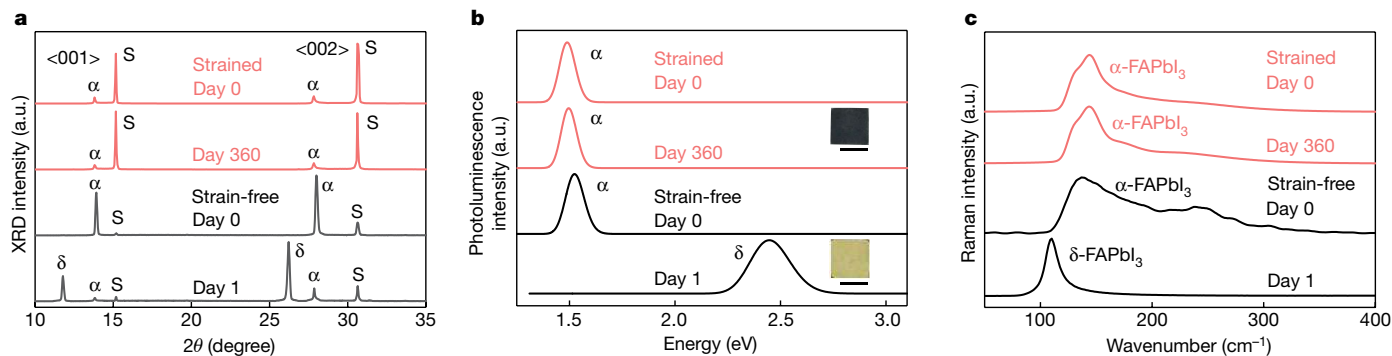


**Fig. 4 | Epitaxial stabilization.** **a**, Phase stability comparison of thin (sub-100 nm,  $\sim 2.4\%$  strained; pink) and thick (about  $10\ \mu\text{m}$ , strain-free; black) epitaxial  $\alpha\text{-FAPbI}_3$  on  $\text{MAPbCl}_{1.50}\text{Br}_{1.50}$  substrates by XRD.  $\alpha$ ,  $\alpha\text{-FAPbI}_3$ ;  $\delta$ ,  $\delta\text{-FAPbI}_3$ ; S, substrate. The thin, strained sample shows better phase stability (red curves). For the thick, strain-free sample, the (001) peak for  $\alpha\text{-FAPbI}_3$  at  $13.92^\circ$  is the same as the strain-free sample in Supplementary Fig. 1a, which indicates that the top surface of the thick sample is fully relaxed (day 0, black curve). The X-ray can penetrate about  $10\text{--}20\ \mu\text{m}$  into the halide perovskites, which explains why the substrate peaks are more intense in the thin sample than in the thick sample. The thick, strain-free sample shows signs of a phase transition to  $\delta\text{-FAPbI}_3$  after 24 h (lower black curve). **b**, Phase stability study by photoluminescence spectroscopy. Re-measurement of the thin, strained sample after 360 d (lower pink curve) shows no obvious photoluminescence peak shift, but does show a slight decrease in peak intensity owing to its natural

degradation into  $\text{PbI}_2$  (ref. <sup>16</sup>). For the thick, strain-free sample, the photoluminescence spectrum shows an emission peak close to  $1.52\ \text{eV}$ , similar to that in the strain-free  $\alpha\text{-FAPbI}_3$  bulk crystal shown in Fig. 2a, indicating a full strain relaxation in the thick sample. Re-measurement after 24 h (lower black curve) shows that the thick film undergoes a transition from the  $\alpha$  phase to the  $\delta$  phase. Insets, optical images of the two samples, showing clear visual clues of the phase stability in the thin, strained sample (black  $\alpha$  phase) and the phase transition in the thick, strain-free sample (yellow  $\delta$  phase) after 24 h. Scale bars,  $2\ \text{mm}$ . **c**, Phase stability study by Raman spectroscopy. The Raman characteristics of the thin, strained sample show a peak at  $143\ \text{cm}^{-1}$  with no substantial difference after 360 d; the thick, strain-free sample (peak at  $136\ \text{cm}^{-1}$ ) shows signs of a phase transformation to  $\delta\text{-FAPbI}_3$  after 24 h, as revealed by its signature peak at  $108\ \text{cm}^{-1}$ .

Hall effect measurements have an epitaxial-layer thickness larger than the critical thickness to ensure sufficient contact area between the halide perovskite and the bottom electrode. Therefore, a high strain level will induce a high concentration of dislocations that degrade the hole mobility.

To validate the Hall mobility, we carried out time-of-flight measurements. The transient photocurrents after single excitation are plotted logarithmically in Fig. 3c. The carrier transit time shows the smallest value of the film under  $\sim 1.2\%$  strain. The calculated carrier mobility is plotted as a function of the strain applied (Fig. 3d, see the Supplementary Information for calculation details), and shows a similar trend to that given by the Hall effect. We note that the absolute mobility values from the time-of-flight and Hall effect measurements differ, owing to experimental uncertainties in the type and quality of electronic contacts made during the fabrication processes<sup>31</sup>. The space-charge-limited-current method can quantify trap density<sup>32</sup>. Results show that a higher strain level leads to a higher trap density (Extended Data Fig. 7 and Supplementary Fig. 11), which explains the observed decrease in mobility under a higher strain magnitude. Capacitance–frequency ( $C\text{--}\omega$ ) spectroscopy is also used to cross-check the trap density (Supplementary Fig. 12), the results of which correspond well with those obtained by the space-charge-limited-current method.

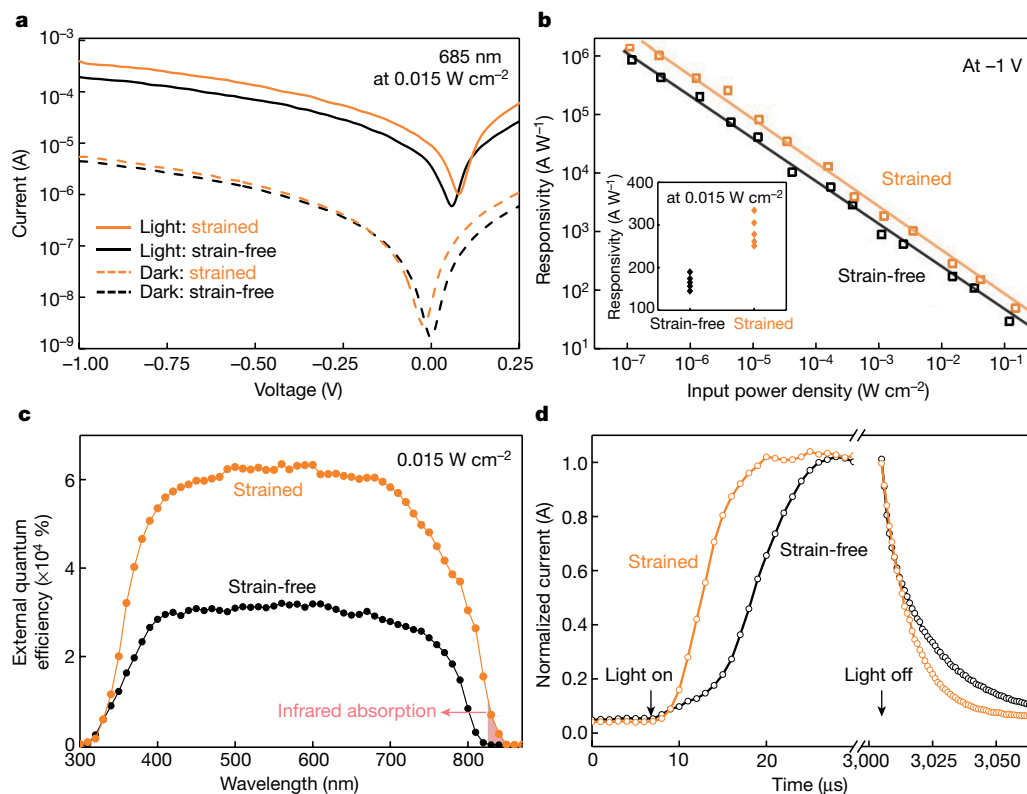
It is widely accepted that  $\alpha\text{-FAPbI}_3$  crystals are metastable at room temperature and can quickly phase transform to photo-inactive  $\delta\text{-FAPbI}_3$  within approximately 24 h (ref. <sup>16</sup>), owing to its internal lattice strain and low entropy<sup>19,33</sup>. Existing strategies for  $\alpha\text{-FAPbI}_3$  stabilization, including alloying<sup>26</sup> and surface passivation<sup>34</sup>, either widen the bandgap or raise the carrier transport barrier by introducing nonconductive ligands (detailed discussions in the Supplementary Information). However, the epitaxial  $\alpha\text{-FAPbI}_3$  thin film exhibits long-lasting phase stability at room temperature.

Figure 4a shows XRD results of a sub-100-nm epitaxial  $\alpha\text{-FAPbI}_3$  thin film that is stable for at least 360 d after growth (red curves in Fig. 4a). In the  $10\text{-}\mu\text{m}$  epitaxial thick film (far beyond the threshold thickness at which the strain is fully relaxed), the stabilization effect disappears: after 24 h, XRD peaks from  $\delta\text{-FAPbI}_3$  can be detected (black curves in

Fig. 4a). The phase stability of the strained  $\alpha\text{-FAPbI}_3$  is also verified by photoluminescence (Fig. 4b) and Raman spectroscopy (Fig. 4c). A possible stabilization effect from incorporating bromine or chlorine into the  $\alpha\text{-FAPbI}_3$  can be excluded, because those foreign ions would stabilize the  $\alpha$ -phase regardless of the epilayer thickness. X-ray photoelectron spectroscopy (XPS) measurements showing the absence of bromine and chlorine provide additional evidence that this is not the origin of the stability (Extended Data Fig. 8).

The mechanism of the stable thin  $\alpha\text{-FAPbI}_3$  can be explained by two reasons. First, the interfacial energy of cubic  $\alpha\text{-FAPbI}_3$ /cubic substrate is much lower than that of hexagonal  $\delta\text{-FAPbI}_3$ /cubic substrate, which is the most critical factor for the stabilization effect (Supplementary Fig. 13, Supplementary Table 3, and see Supplementary Information for details). The epitaxial lattice is constrained to the substrate owing to the strong ionic bonds between them and, therefore, the lattice is restricted from the phase transition. Second, the driving force of the  $\alpha$ -to- $\delta$  phase transition is believed to be the internal tensile strain in the  $\alpha\text{-FAPbI}_3$  unit cell, which can induce the formation of vacancies and subsequent phase transition<sup>35</sup>. In this study, the epitaxial film is under compressive strain, which neutralizes the effect of the internal tensile strain. Therefore, the synergistic effect of the low-energy coherent epitaxial interface and the neutralizing compressive strain are the key to  $\alpha\text{-FAPbI}_3$  stabilization. As a control, epitaxial  $\alpha\text{-FAPbI}_3$  thin film is removed from the substrate (Supplementary Fig. 14); the removed  $\alpha\text{-FAPbI}_3$  transforms to the  $\delta$  phase within 24 h.

We demonstrate high-responsivity photodetectors as a use case of the strain engineered  $\alpha\text{-FAPbI}_3$  thin film. Figure 5a shows the current–voltage ( $I\text{--}V$ ) characteristics of a strain-free device and a device under  $\sim 1.2\%$  strain. The dark current at  $-1\ \text{V}$  in the strained device is around 15% higher than that in the strain-free one, indicating the higher defect density of the strained device. However, the photocurrent in the strained device increases by approximately 180% compared to the strain-free device. We attribute the photocurrent increase to higher carrier mobility and better alignment of VBM to the Fermi level of the gold electrode under compressive strain (Supplementary Fig. 15).



**Fig. 5 | Photodetector characterizations of the  $\alpha$ -FAPbI<sub>3</sub> thin films.**

**a**,  $I$ - $V$  characteristics of Au/ $\alpha$ -FAPbI<sub>3</sub>/indium tin oxide photoconductor structured photodetectors. The dark current and photocurrent of the  $-1.2\%$  strained detector are about 15% and 180% higher than those of its strain-free counterpart. Detectors are tested with a 685-nm laser under  $0.015 \text{ W cm}^{-2}$ . **b**, Comparison of responsivity of the  $-1.2\%$  strained and strain-free photodetectors. The responsivity of both devices shows an increasing trend with decreasing incident power, as the chances of carrier recombination go down at low illumination intensities<sup>36</sup>. The strained device yields a higher

responsivity owing to higher carrier mobility and better band alignment. Inset, the statistical average of the detector performance. Number of experiments,  $n = 5$  for each strain value. **c**, External quantum efficiency spectra of the  $-1.2\%$  strained and strain-free photodetectors showing that the strained photodetector yields a higher external quantum efficiency as well as a broader absorption spectrum (Extended Data Fig. 9d), owing to enhanced carrier mobility and bandgap reduction. **d**, Response times of the photodetectors, with faster rise and fall times for the  $-1.2\%$  strained ( $9 \mu\text{s}$  and  $34 \mu\text{s}$ ) than the strain-free ( $14 \mu\text{s}$  and  $50 \mu\text{s}$ ) device due to the enhanced carrier mobility and transport.

Responsivity of the two photodetectors—defined as the change in photocurrent per unit of illumination intensity—is measured at various illumination intensities (Fig. 5b). The responsivity of the strained device, which reaches a maximum of  $1.3 \times 10^6 \text{ A W}^{-1}$  at an incident power density of  $1.1 \times 10^{-7} \text{ W cm}^{-2}$ , is almost twice of that of the strain-free device. This is again attributed to the enhanced carrier mobility and the better band alignment of the strained device. The responsivity of this strained device is, to our knowledge, the highest reported for a  $\alpha$ -FAPbI<sub>3</sub> device under similar measurement conditions (for example, applied voltage and incident power (Supplementary Table 4)). Similar to the trend in Hall effect carrier mobility, the measured responsivity peaks at  $-1.2\%$  strain (Extended Data Fig. 9a). Compressive strain also improves the detectivity and the gain of the photodetector (Extended Data Fig. 9b, c). Devices with a diode structure can reduce the dark current, but have a much lower responsivity: on average 500 times lower than that of the photoconductor-type device (Supplementary Fig. 16).

The strained device also shows an enhanced external quantum efficiency over the visible range (Fig. 5c), owing to the enhanced carrier mobility as well as more efficient carrier transport across the gold-perovskite interface. Additionally, after normalizing the spectra, a distinct response in the short-wave infrared region ( $>810 \text{ nm}$ ) can be identified for the strained device (Extended Data Fig. 9d), consistent with the photoluminescence measurements showing bandgap reduction under compressive strain. The rise and fall times of the strained device are around 30% shorter than those of the strain-free device, indicating a faster carrier dynamics (Fig. 5d).

## Online content

Any methods, additional references, Nature Research reporting summaries, source data, extended data, supplementary information, acknowledgements, peer review information; details of author contributions and competing interests; and statements of data and code availability are available at <https://doi.org/10.1038/s41586-019-1868-x>.

- Smith, C. S. Piezoresistance effect in germanium and silicon. *Phys. Rev.* **94**, 42–49 (1954).
- Llordés, A. et al. Nanoscale strain-induced pair suppression as a vortex-pinning mechanism in high-temperature superconductors. *Nat. Mater.* **11**, 329–336 (2012).
- Yang, W. S. et al. Iodide management in formamidinium-lead-halide-based perovskite layers for efficient solar cells. *Science* **356**, 1376–1379 (2017).
- Lin, K. et al. Perovskite light-emitting diodes with external quantum efficiency exceeding 20 per cent. *Nature* **562**, 245–248 (2018).
- Feng, J. et al. Single-crystalline layered metal-halide perovskite nanowires for ultrasensitive photodetectors. *Nat. Electron.* **1**, 404–410 (2018).
- Lü, X. et al. Enhanced structural stability and photo responsiveness of  $\text{CH}_3\text{NH}_3\text{SnI}_3$  perovskite via pressure-induced amorphization and recrystallization. *Adv. Mater.* **28**, 8663–8668 (2016).
- Liu, G. et al. Pressure-induced bandgap optimization in lead-based perovskites with prolonged carrier lifetime and ambient retainability. *Adv. Funct. Mater.* **27**, 1604208 (2017).
- Wang, Y. et al. Pressure-induced phase transformation, reversible amorphization, and anomalous visible light response in organolead bromide perovskite. *J. Am. Chem. Soc.* **137**, 11144–11149 (2015).
- Chen, B. et al. Large electrostrictive response in lead halide perovskites. *Nat. Mater.* **17**, 1164 (2018).
- Zhao, J. et al. Strained hybrid perovskite thin films and their impact on the intrinsic stability of perovskite solar cells. *Sci. Adv.* **3**, eaao5616 (2017).

11. Zhu, C. et al. Strain engineering in perovskite solar cells and its impacts on carrier dynamics. *Nat. Commun.* **10**, 815 (2019).
12. Steele, J. A. et al. Thermal unequilibrium of strained black CsPbI<sub>3</sub> thin films. *Science* **365**, 679–684 (2019).
13. Wang, Y. et al. Nontrivial strength of van der Waals epitaxial interaction in soft perovskites. *Phys. Rev. Mater.* **2**, 076002 (2018).
14. Li, X., et al. Residual nanoscale strain in cesium lead bromide perovskite reduces stability and shifts local luminescence. *Chem. Mater.* **31**, 2778–2785 (2019).
15. Wang, Y. et al. Defect-engineered epitaxial VO<sub>2.5</sub> in strain engineering of heterogeneous soft crystals. *Sci. Adv.* **4**, eaar3679 (2018).
16. Han, Q. et al. Single crystal formamidinium lead iodide (FAPbI<sub>3</sub>): insight into the structural, optical, and electrical properties. *Adv. Mater.* **28**, 2253–2258 (2016).
17. Fang, Y., Dong, Q., Shao, Y., Yuan, Y. & Huang, J. Highly narrowband perovskite single-crystal photodetectors enabled by surface-charge recombination. *Nat. Photon.* **9**, 679–686 (2015).
18. Pohl, U. W. *Epitaxy of Semiconductors: Introduction to Physical Principles* (Springer, 2013).
19. Chen, T. et al. Entropy-driven structural transition and kinetic trapping in formamidinium lead iodide perovskite. *Sci. Adv.* **2**, e1601650 (2016).
20. Maculan, G. et al. CH<sub>3</sub>NH<sub>3</sub>PbCl<sub>3</sub> single crystals: inverse temperature crystallization and visible-blind UV-photodetector. *J. Phys. Chem. Lett.* **6**, 3781–3786 (2015).
21. Rakita, Y., Cohen, S. R., Kedem, N. K., Hodes, G. & Cahen, D. Mechanical properties of APbX<sub>3</sub> (A= Cs or CH<sub>3</sub>NH<sub>3</sub>; X= I or Br) perovskite single crystals. *MRS Commun.* **5**, 623–629 (2015).
22. Steele, J. A. et al. Direct laser writing of δ- to α-phase transformation in formamidinium lead iodide. *ACS Nano* **11**, 8072–8083 (2017).
23. Li, D. et al. Size-dependent phase transition in methylammonium lead iodide perovskite microplate crystals. *Nat. Commun.* **7**, 11330 (2016).
24. Sarmah, S. P. et al. Double charged surface layers in lead halide perovskite crystals. *Nano Lett.* **17**, 2021–2027 (2017).
25. Kanemitsu, Y. Luminescence spectroscopy of lead-halide perovskites: materials properties and application as photovoltaic devices. *J. Mater. Chem. C* **5**, 3427–3437 (2017).
26. Xie, L.-Q. et al. Understanding the cubic phase stabilization and crystallization kinetics in mixed cations and halides perovskite single crystals. *J. Am. Chem. Soc.* **139**, 3320–3323 (2017).
27. Katan, C., Mohite, A. D. & Even, J. Entropy in halide perovskites. *Nat. Mater.* **17**, 377–379 (2018).
28. Ge, C. et al. Ultralow thermal conductivity and ultrahigh thermal expansion of single-crystal organic–inorganic hybrid perovskite CH<sub>3</sub>NH<sub>3</sub>PbX<sub>3</sub> (X = Cl, Br, I). *J. Phys. Chem. C* **122**, 15973–15978 (2018).
29. Yin, W.-J., Yang, J.-H., Kang, J., Yan, Y. & Wei, S.-H. Halide perovskite materials for solar cells: a theoretical review. *J. Mater. Chem. A* **3**, 8926–8942 (2015).
30. Giorgi, G., Fujisawa, J.-I., Segawa, H. & Yamashita, K. Small photocarrier effective masses featuring ambipolar transport in methylammonium lead iodide perovskite: a density functional analysis. *J. Phys. Chem. Lett.* **4**, 4213–4216 (2013).
31. Herz, L. M. Charge-carrier mobilities in metal halide perovskites: fundamental mechanisms and limits. *ACS Energy Lett.* **2**, 1539–1548 (2017).
32. Dong, Q. et al. Electron-hole diffusion lengths > 175 μm in solution-grown CH<sub>3</sub>NH<sub>3</sub>PbI<sub>3</sub> single crystals. *Science* **347**, 967–970 (2015).
33. Zheng, X. et al. Improved phase stability of formamidinium lead triiodide perovskite by strain relaxation. *ACS Energy Lett.* **1**, 1014–1020 (2016).
34. Fu, Y. et al. Stabilization of the metastable lead iodide perovskite phase via surface functionalization. *Nano Lett.* **17**, 4405–4414 (2017).
35. Saidaminov, M. I. et al. Suppression of atomic vacancies via incorporation of isovalent small ions to increase the stability of halide perovskite solar cells in ambient air. *Nat. Energy* **3**, 648–654 (2018).
36. Liu, Y. et al. A 1300 mm<sup>2</sup> ultrahigh-performance digital imaging assembly using high-quality perovskite single crystals. *Adv. Mater.* **30**, 1707314 (2018).

**Publisher's note** Springer Nature remains neutral with regard to jurisdictional claims in published maps and institutional affiliations.

© The Author(s), under exclusive licence to Springer Nature Limited 2020

# Article

## Methods

### Precursor synthesis

Methylammonium bromide (MABr) was synthesized as the precursor for the substrate growth. First, 20 ml methylamine (40% in methanol, Tokyo Chemical Industry) and 21.2 ml hydrobromic acid (48 wt% in water, Sigma Aldrich) were mixed in an ice bath and the temperature was maintained for the reaction to continue for 2 h. The mixture was heated to 80 °C to evaporate the solvent. The precipitate was dissolved in anhydrous ethanol (Sigma Aldrich) at 80 °C and cooled down for recrystallization. The crystals were then centrifuged with diethyl ether and dried at 80 °C overnight.

### Crystal growth

Methylammonium lead chloride (MAPbCl<sub>3</sub>) solution was prepared by mixing 0.6752 g of methylammonium chloride (MACl, 98%, Tokyo Chemical Industry) and 2.781 g lead chloride (PbCl<sub>2</sub>, 99%, Alfa Aesar) in a mixed solution of 5 ml anhydrous dimethylformamide (99.8%, Aldrich) and 5 ml anhydrous dimethyl sulfoxide (DMSO, 99.8%, Aldrich). Methylammonium lead bromide (MAPbBr<sub>3</sub>) solution was prepared by mixing 1.120 g MABr and 3.670 g lead bromide (PbBr<sub>2</sub>, 98%, Acros) in 10 ml dimethylformamide. The MAPbCl<sub>3</sub> and MAPbBr<sub>3</sub> solutions were mixed with different ratios. The mixed solutions were kept at room temperature to slowly evaporate the solvent, and single crystals were collected to use as substrates. FAPbI<sub>3</sub> solutions were prepared by mixing formamidinium iodide (FAI, 99.9%, Greatcell Solar) and lead iodide (PbI<sub>2</sub>, 99.99%, Tokyo Chemical Industry) at a molar ratio of 1:1 in anhydrous gamma-butyrolactone (Sigma Aldrich) with different concentrations. Strain-free  $\alpha$ -FAPbI<sub>3</sub> single crystals were obtained by heating the FAPbI<sub>3</sub> solutions to 120 °C.

### Epitaxial growth

The substrates were heated to different temperatures, and the preheated FAPbI<sub>3</sub> solutions (at 100 °C) were then deposited onto the substrates for epitaxial growth.

### Structural and optical characterizations

SEM images were taken with a Zeiss Sigma 500 SEM operated at 3 kV. The  $2\theta/\omega$  XRD patterns, the rocking curve ( $\omega$  scan), and the asymmetrical reciprocal space mapping around the (104) reflection of the substrate were measured by a Rigaku Smartlab diffractometer equipped with a copper K $\alpha_1$  radiation source ( $\lambda = 0.15406$  nm) and a germanium (220  $\times$  2) monochromator. The unit cell parameters ( $a$ ,  $c$ ) for (104) reflection reciprocal space mapping were converted from ( $Q_x$ ,  $Q_z$ ) by  $a = 1/Q_x$ ,  $c = 4/Q_z$ . Raman and photoluminescence spectra were measured by a Raman spectrometer (Renishaw inVia). Raman peak fitting was done by the Renishaw inVia software. Atomic force microscopy was carried out by a scanning probe microscope (Veeco) in a tapping mode. XPS and UPS were carried out by a Kratos AXIS Supra with an aluminium K $\alpha$  anode source and a He I (21.22 eV) source, respectively. Measurements were operated under a chamber pressure of  $10^{-8}$  torr. XPS data were calibrated with the C 1s peak (284.8 eV). If not otherwise specified, bulk  $\alpha$ -FAPbI<sub>3</sub> single crystals were used as the strain-free samples for structural and optical characterizations.

### Device fabrication

Devices with a vertical structure were fabricated based on a lithography-based method<sup>37</sup>. Parylene-C (50 nm) and gold (50 nm) were sequentially deposited on the substrates, followed by a photolithography process with photoresist AZ-1512. The pattern was composed of an array of 2- $\mu$ m-diameter circles (exposed) with 1  $\mu$ m interdistance (covered by photoresist). The gold was chemically etched with wet etchants and the Parylene-C was precisely etched by reactive ion etching. The etched substrates underwent secondary growth in their corresponding growth solutions so that the substrate surface reached the same height as the electrode. Epitaxial growth on the patterned substrate enabled the  $\alpha$ -FAPbI<sub>3</sub> crystals to initiate from the exposed patterns and gradually merge into a thin film with a controllable

thickness. We note that the MAPbCl<sub>x</sub>Br<sub>3-x</sub> substrates were used for the strained devices (heteroepitaxy) and  $\alpha$ -FAPbI<sub>3</sub> substrates were used for the strain-free devices (homoepitaxy). The top electrodes were then deposited by sputtering (for indium tin oxide, 200 nm). For vertical devices, the area of the top electrode was controlled to be  $1 \times 1$  mm<sup>2</sup> using a shadow mask. For planar devices, Parylene-C (50 nm) and the electrode (gold, 50 nm) were deposited using a shadow mask with designed electrode layouts.

### Electrical characterizations

Space-charge-limited-current measurements were carried out by a source meter (Keithley 2400) and a customized probe station in a dark environment. Devices with an Au/Perovskite/Au structure were used.  $C-\omega$  measurements were carried out by a parameter analyser (B1500, Agilent) in a dark environment. Devices with an Au/perovskite/indium tin oxide structure were used. The thickness of  $\alpha$ -FAPbI<sub>3</sub> of all devices for space-charge-limited current and  $C-\omega$  measurements was controlled to be 500 nm. Hall effect measurements were carried out with a Lake Shore Hall measurement system (HM 3000) using the van der Pauw method. We note that the Parylene-C layer prevented direct contact between the substrate and electrodes, eliminating possible carriers extracted from the substrate. The thickness of the  $\alpha$ -FAPbI<sub>3</sub> for all devices for Hall effect measurement was controlled to be 500 nm. For the time-of-flight measurement, a 685-nm-pulse laser (10 mW cm<sup>-2</sup>) with  $<10^{-10}$ -s pulse width was used as the light source. Photoresponse was measured with an oscilloscope (MSO6104A Channel Mixed Signal, Agilent). An external bias of 1 V was applied to drive the carriers in the device while a 1-M $\Omega$  resistor was connected in series to simulate the open-circuit condition so that the carriers were effectively blocked in the devices<sup>32</sup>. The measurement was carried out in the dark while the bias and the laser power were kept constant. The experiment setup followed the reported time-of-flight measurement of halide perovskite single crystals<sup>32,38-40</sup>. The  $\alpha$ -FAPbI<sub>3</sub> thickness of all devices for time-of-flight measurements was also controlled to be 500 nm.

### Photodetector characterizations

Devices with the structure shown in Supplementary Figs. 15 and 16 were used. A 685-nm laser was used as the light source. The  $I-V$  characteristics were collected on a probe station with an Agilent B2912A source meter.

### First-principles calculations

First-principles density functional theory calculations were performed using the Vienna ab initio Simulation Package (VASP)<sup>41</sup>. Electron-ion interactions were described using the Projector Augmented Wave pseudopotential<sup>42</sup>. The electron-electron exchange-correlation functional was treated using the Generalized Gradient Approximation parametrized by Perdew, Burke and Ernzerhof<sup>43</sup>. For bandgap calculations, spin-orbit coupling was incorporated owing to the heavy element Pb, and the hybrid functionals within Heyd-Scuseria-Ernzerhof formalism with 25% Hartree-Fock exchange were employed. A cutoff energy of 400 eV for the plane-wave basis set was used. All structures were fully optimized until all components of the residual forces were smaller than  $0.01$  eV  $\text{\AA}^{-1}$ . The convergence threshold for self-consistent-field iteration was set at  $10^{-5}$  eV. For optimization of the cubic lattice parameter, a  $\Gamma$ -centred  $3 \times 3 \times 3$   $k$ -point mesh was used. A denser  $k$ -point mesh of  $4 \times 4 \times 4$  was used to obtain accurate energies and electronic structures for strained cells. For optimization and static calculations of the heterostructural models,  $\Gamma$ -centred  $4 \times 4 \times 1$  and  $5 \times 5 \times 1$   $k$ -point meshes were used, respectively. Raman intensities were calculated by the CASTEP module in Materials Studios<sup>44</sup> with a  $3 \times 3 \times 3$   $k$ -point mesh and a 400 eV cutoff energy.

### Finite element analysis simulations

Simulation of the current density was done by the multiphysics analysis in COMSOL (version 5.4; www.comsol.com). Simulation of the elastic strain relaxation was done by the ABAQUS<sup>45</sup>.

## Data availability

The data that support the findings of this study are available from the corresponding authors on reasonable request.

37. Lei, Y. et al. Controlled homoepitaxial growth of hybrid perovskites. *Adv. Mater.* **30**, 1705992 (2018).
38. Shi, D. et al. Low trap-state density and long carrier diffusion in organolead trihalide perovskite single crystals. *Science* **347**, 519–522 (2015).
39. Pospisil, J. et al. Density of bulk trap states of hybrid lead halide perovskite single crystals: temperature modulated space-charge-limited-currents. *Sci. Rep.* **9**, 3332 (2019).
40. Saidaminov, M. I. et al. High-quality bulk hybrid perovskite single crystals within minutes by inverse temperature crystallization. *Nat. Commun.* **6**, 7586 (2015).
41. Kresse, G. & Furthmüller, J. Efficient iterative schemes for ab initio total-energy calculations using a plane-wave basis set. *Phys. Rev. B* **54**, 11169–11186 (1996).
42. Blöchl, P. E. Projector augmented-wave method. *Phys. Rev. B* **50**, 17953–17979 (1994).
43. Perdew, J. P., Burke, K. & Ernzerhof, M. Generalized gradient approximation made simple. *Phys. Rev. Lett.* **77**, 3865–3868 (1996).
44. Clark, S. et al. First principles methods using CASTEP. *Z. Kristallogr.* **220**, 567–570 (2005).
45. Smith, M. *ABAQUS/Standard User's Manual Version 6.9* (Dassault Systèmes Simulia Corp, 2009).

**Acknowledgements** We thank T. N. Ng and Z. Wu for guidance on the transient photocurrent measurement; P. Liu and S. Yu for sharing the Rikagu Smartlab diffractometer; D. P. Fenning and X. Li for discussions; Q. Lin for guidance on the reciprocal space mapping measurements; S. Wang for analysis and discussions of the UPS; Y. Zeng for training on the Renishaw inVia

Raman spectrometer; Y. Li, Y. Yin and M. Chen for guidance on the finite element analysis simulations; and S. Xiang for constructive feedback on manuscript preparation. This work was supported by the startup fund by the University of California San Diego. The microfabrication involved in this work was performed at the San Diego Nanotechnology Infrastructure (SDNI) of UCSD, a member of the National Nanotechnology Coordinated Infrastructure, which was supported by the the National Science Foundation (grant number ECCS-1542148). K.Y. acknowledges the National Science Foundation under award number ACI-1550404 and computational resources from Extreme Science and Engineering Discovery Environment (XSEDE), which is supported by National Science Foundation grant number ACI-1548562.

**Author contributions** S.X. and Y.C. conceived the idea. Y.C. and Y. Lei prepared the samples. Y.C. and Y. Lei took the optical and SEM images. Y.C., J.S. and M.-H.C. carried out the XRD, Raman and photoluminescence spectroscopy characterizations. R.R. and A.E.I. contributed to the temperature-dependent photoluminescence characterizations. Y. Li and J.S. carried out the density functional theory calculations. Y.C. and W.C. carried out the finite element analysis simulations. Y.C., Y. Lei, Y.G., C.W. and J.C. contributed to the device fabrication. Y.C., Y.Y. and W.C. carried out the mobility measurements. Y.C. carried out the trap density measurements. Y.C. and Y.Y. carried out the photodetectors characterizations. All authors contributed to analysing the data and commenting on the manuscript.

**Competing interests** The authors declare no competing interests.

### Additional information

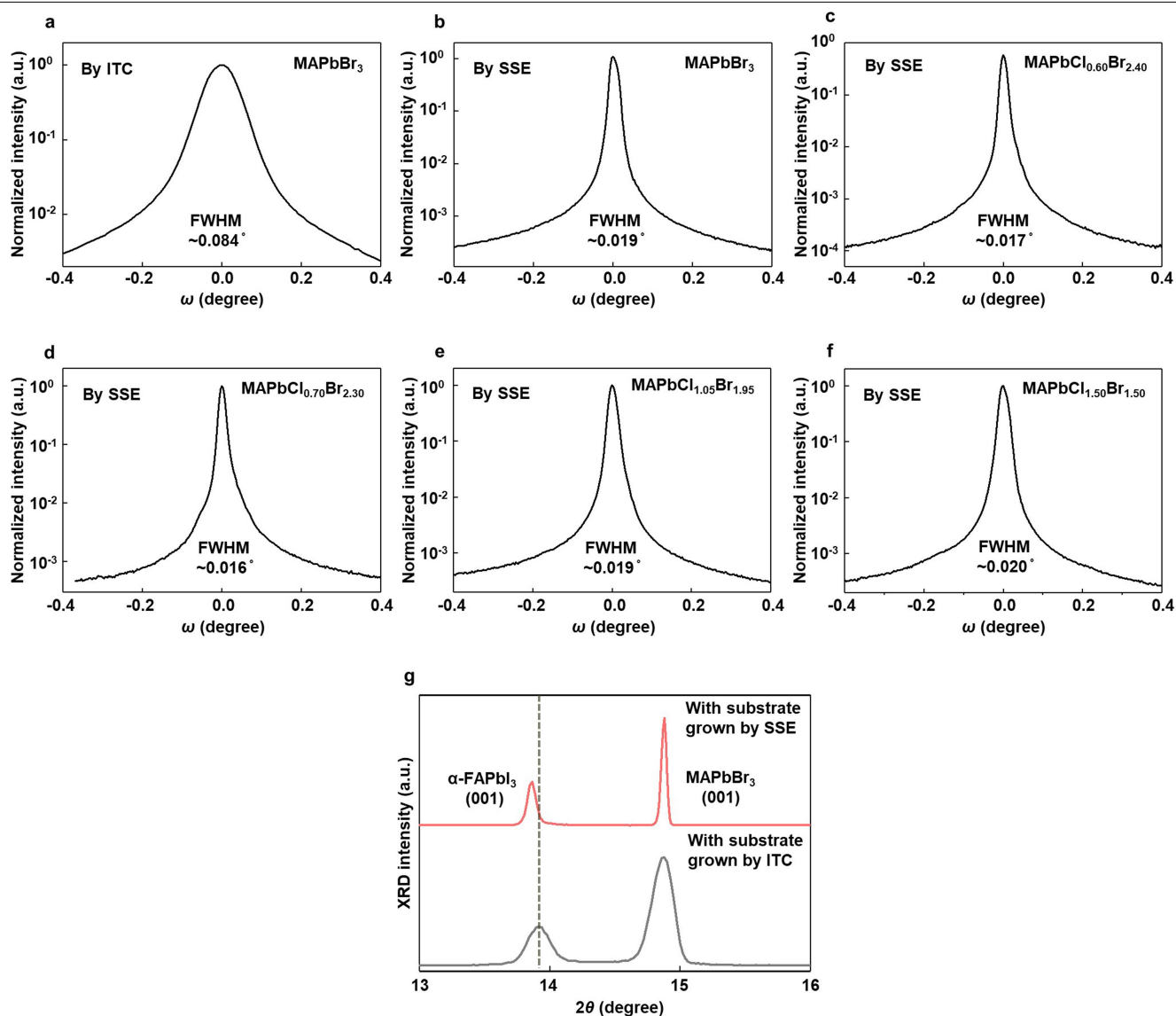
**Supplementary information** is available for this paper at <https://doi.org/10.1038/s41586-019-1868-x>.

**Correspondence and requests for materials** should be addressed to S.X.

**Peer review information** *Nature* thanks Jian Shi, Lijun Zhang and the other, anonymous, reviewer(s) for their contribution to the peer review of this work.

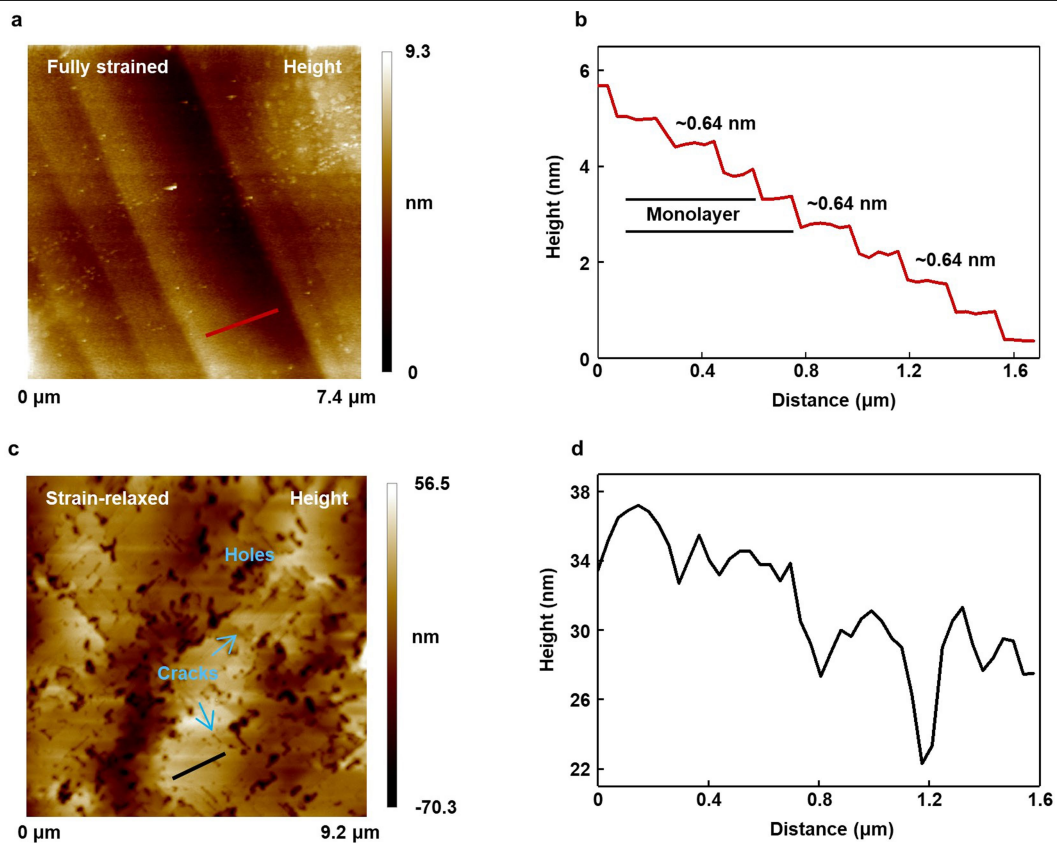
**Reprints and permissions information** is available at <http://www.nature.com/reprints>.





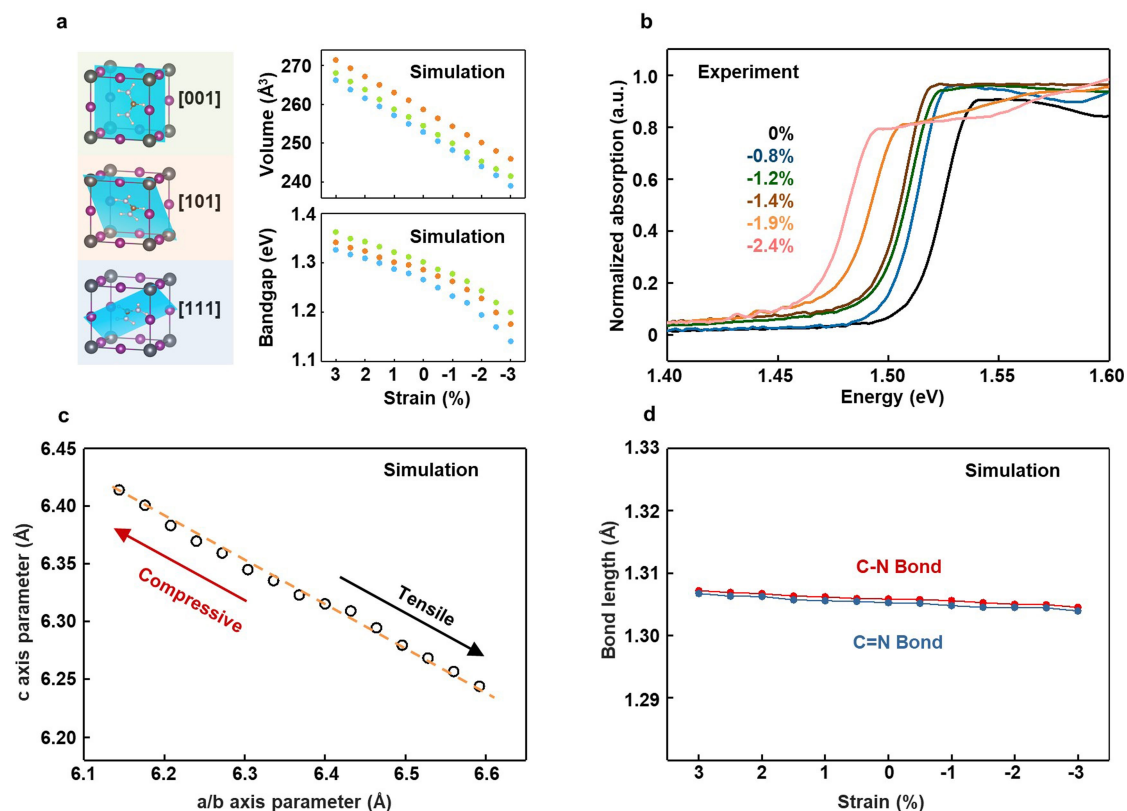
**Extended Data Fig. 1 | Characterization of substrate quality with different growth methods and its impact on the epitaxial strain. a–f,** Rocking curve measurements of substrates grown by the inverse temperature crystallization (ITC) and slow solvent evaporation (SSE) methods. Lower full-width at half-maximum (FWHM) values by the SSE indicate better crystal quality. **g,** XRD patterns of strained  $\alpha$ -FAPbI<sub>3</sub> on a substrate with higher crystal quality (red

curve) and relaxed  $\alpha$ -FAPbI<sub>3</sub> on a substrate with lower crystal quality (grey curve). Dislocations in the substrates can propagate into and relax the strain in the epitaxial  $\alpha$ -FAPbI<sub>3</sub>. The vertical dash line labels the (001) peak position of strain-free  $\alpha$ -FAPbI<sub>3</sub>. The peak position from the strain-relaxed FAPbI<sub>3</sub> (grey curve) shifts back to that of strain-free  $\alpha$ -FAPbI<sub>3</sub>.



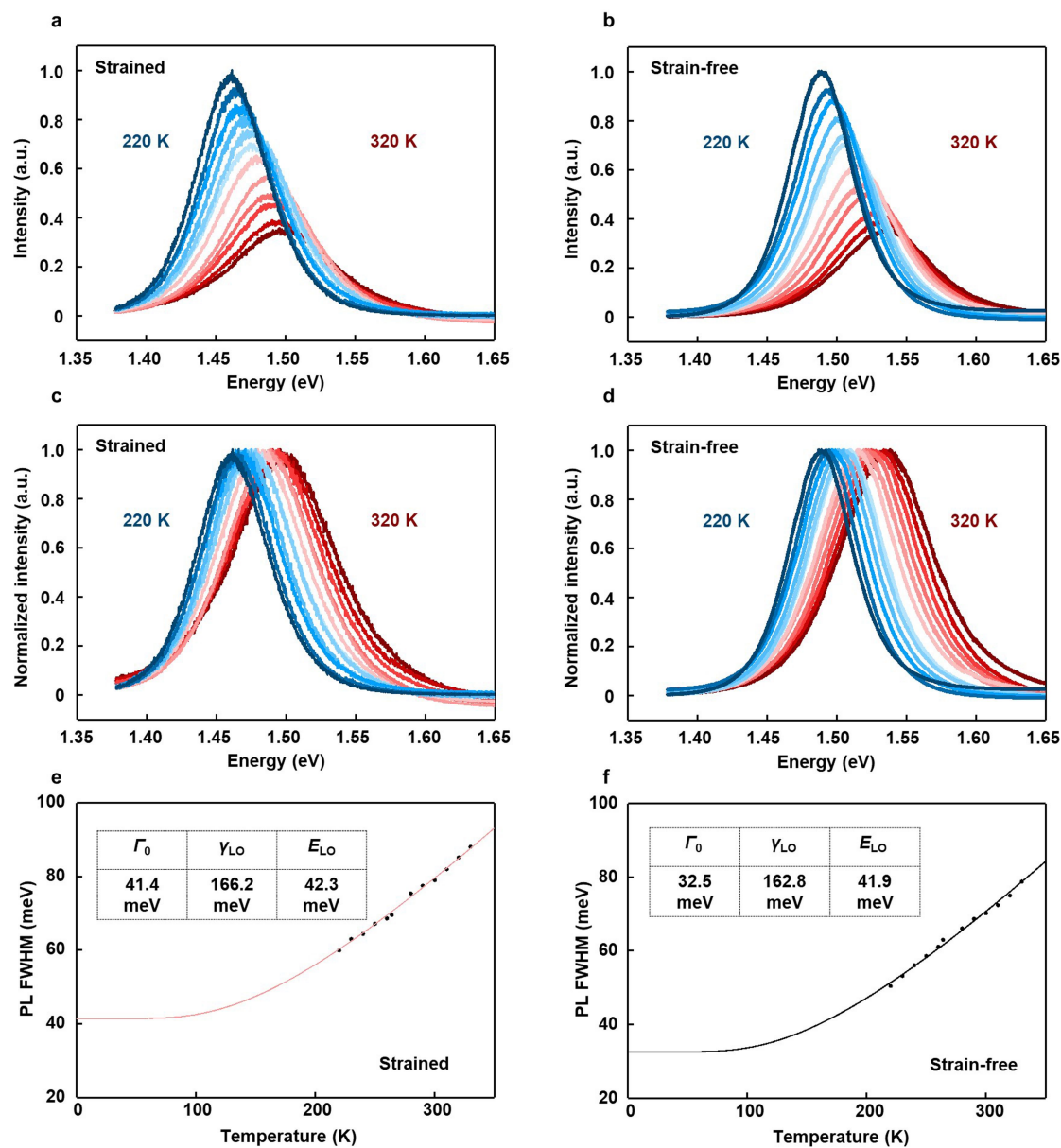
**Extended Data Fig. 2 | Atomic force microscopy morphology characterization of strained and strain-relaxed epitaxial  $\alpha$ -FAPbI<sub>3</sub> films.** **a, b,** A topography image (a) and the corresponding height scanning curve (b) of the red line in a of a strained epitaxial  $\alpha$ -FAPbI<sub>3</sub> thin film. **c, d,** A topography image (c) and the corresponding height scanning curve (d) of the black line in c of a strain-relaxed epitaxial  $\alpha$ -FAPbI<sub>3</sub> thick film. Results show that the strained

thin film adopts a layer-by-layer growth model. No cracks or holes can be detected. As the film thickness increases, the total strain energy builds up and generates dislocations that propagate throughout the film and relax the strain, leading to the formation of cracks and holes. These cracks and holes are typically regarded as a signature of strain relaxation.



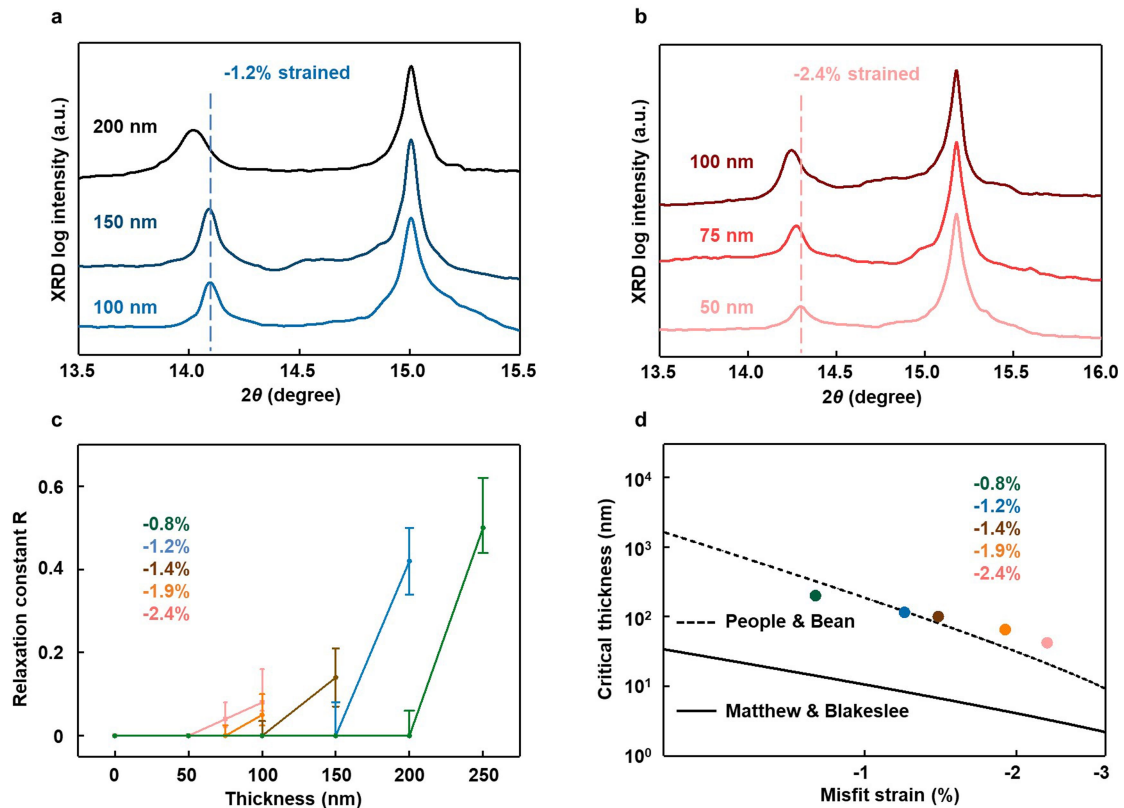
**Extended Data Fig. 3 | First-principles calculations of the strained  $\alpha$ -FAPbI<sub>3</sub> unit cell and experimental absorption spectra of the strained  $\alpha$ -FAPbI<sub>3</sub> under different strains. a**, Evolution of lattice volume and bandgap as a function of strain for three  $\alpha$ -FAPbI<sub>3</sub> lattices with different FA<sup>+</sup> organic cation orientations. For the bandgap calculations, spin-orbit coupling is incorporated owing to the heavy element Pb, and the hybrid functionals within Heyd-Scuseria-Ernzerhof formalism with 25% Hartree-Fock exchange are

employed. **b**, The absorption spectra of the strained  $\alpha$ -FAPbI<sub>3</sub> thin films. The absorption onset redshifts will the increasing strain, which agrees with the photoluminescence spectra and prove that the strain can alter the bandgap of the  $\alpha$ -FAPbI<sub>3</sub>. **c**, The c axis length of the unit cell when biaxially straining the *a/b* axes. The slope of the fitted line shows a Poisson's ratio of about 0.3. **d**, C-N and C=N bond lengths at different strain levels. Simulation results show that the deformation of the FA<sup>+</sup> skeleton is very small under the applied biaxial strain.



**Extended Data Fig. 4 | Temperature-dependent photoluminescence measurement.** **a, b**, Temperature-dependent photoluminescence of strained (**a**) and strain-free (**b**)  $\alpha$ -FAPbI<sub>3</sub> before normalization. **c, d**, Temperature-dependent photoluminescence of strained (**c**) and strain-free (**d**)  $\alpha$ -FAPbI<sub>3</sub> after normalization. Both samples exhibited uniform bandgap narrowing and FWHM narrowing with decreasing the temperature. **e, f**, Temperature-dependent photoluminescence (PL) FWHM of strained (**e**)  $\alpha$ -FAPbI<sub>3</sub> and strain-

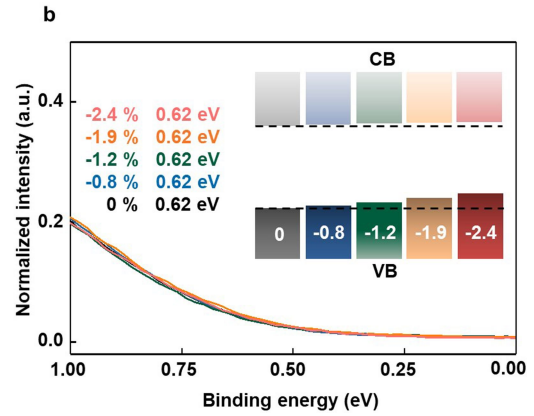
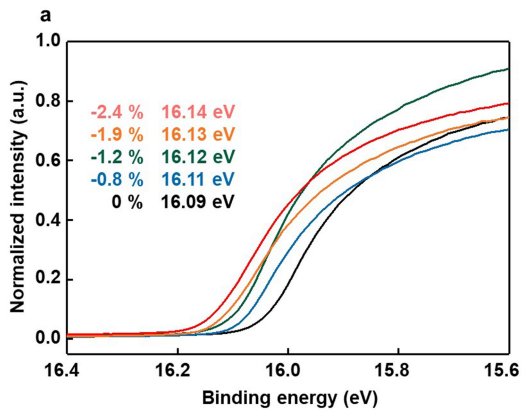
free (**f**)  $\alpha$ -FAPbI<sub>3</sub> with fitting. Results show that the strained  $\alpha$ -FAPbI<sub>3</sub> has a higher  $\Gamma_0$ ,  $\gamma_{LO}$  and  $E_{LO}$  than that of strain-free  $\alpha$ -FAPbI<sub>3</sub> owing to the strain-induced crystalline quality reduction and the strain-enhanced carrier-phonon scattering.  $\Gamma_0$ , temperature-independent emission linewidth term associated with the structural disorder scattering,  $\gamma_{LO}$ , charged-carrier-optical-phonon coupling constant,  $E_{LO}$ , optical phonon energy.



**Extended Data Fig. 5 | Plastic strain relaxation study of the epitaxial  $\alpha$ -FAPbI<sub>3</sub> thin films.** **a, b**, Thickness-dependent in-plane XRD of -1.2% strained (**a**) and -2.4% strained (**b**)  $\alpha$ -FAPbI<sub>3</sub> thin films. Vertical lines label the peak position of the fully strained films. Plastic strain relaxation at relatively high thickness can be evident by the peak shifting to lower angle and peak broadening. **c**, Thickness-dependent relaxation constant  $R$  of the epitaxial  $\alpha$ -FAPbI<sub>3</sub> thin films with different strains. Results show that the critical

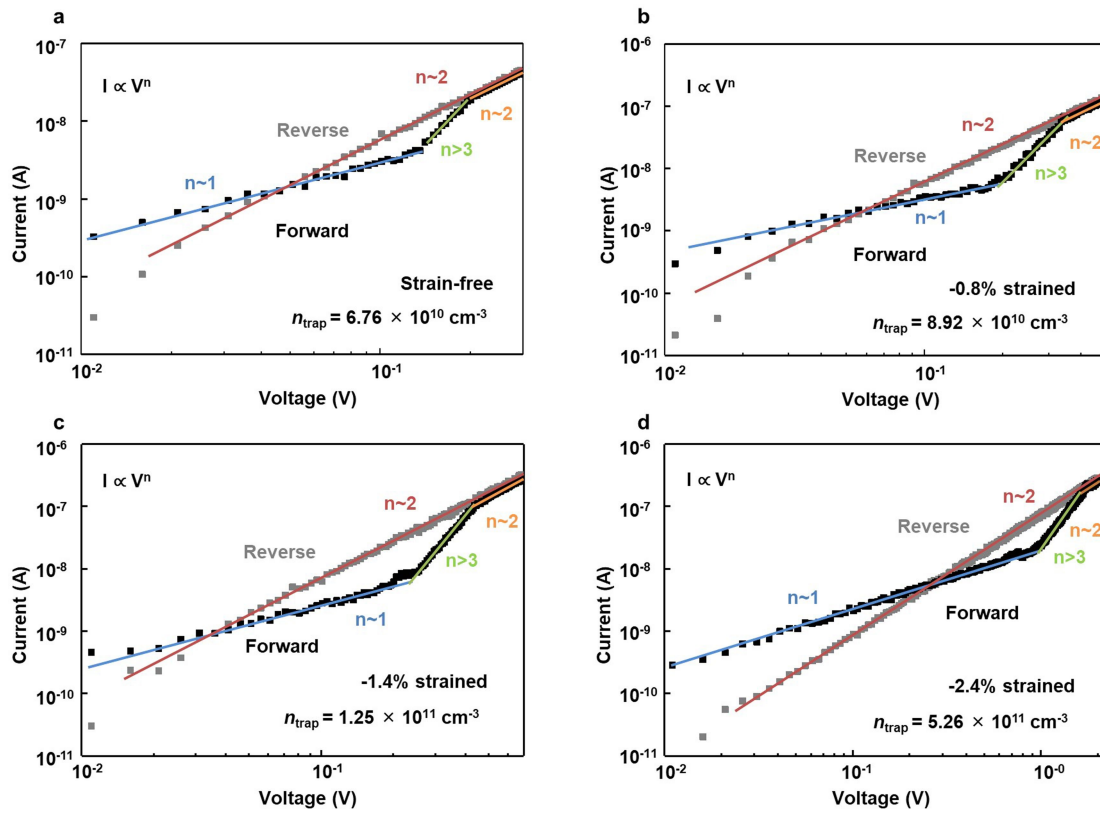
thickness decreases with increasing strain. **d**, Fitting of the experimental critical thicknesses with the People and Bean and the Matthew and Blakeslee models (see Supplementary Information refs 69 and 70). Experimental results agree well with the People and Bean model, indicating that the plastic strain relaxation due to the dislocations generated during the epitaxial growth is the dominating relaxation mechanism.





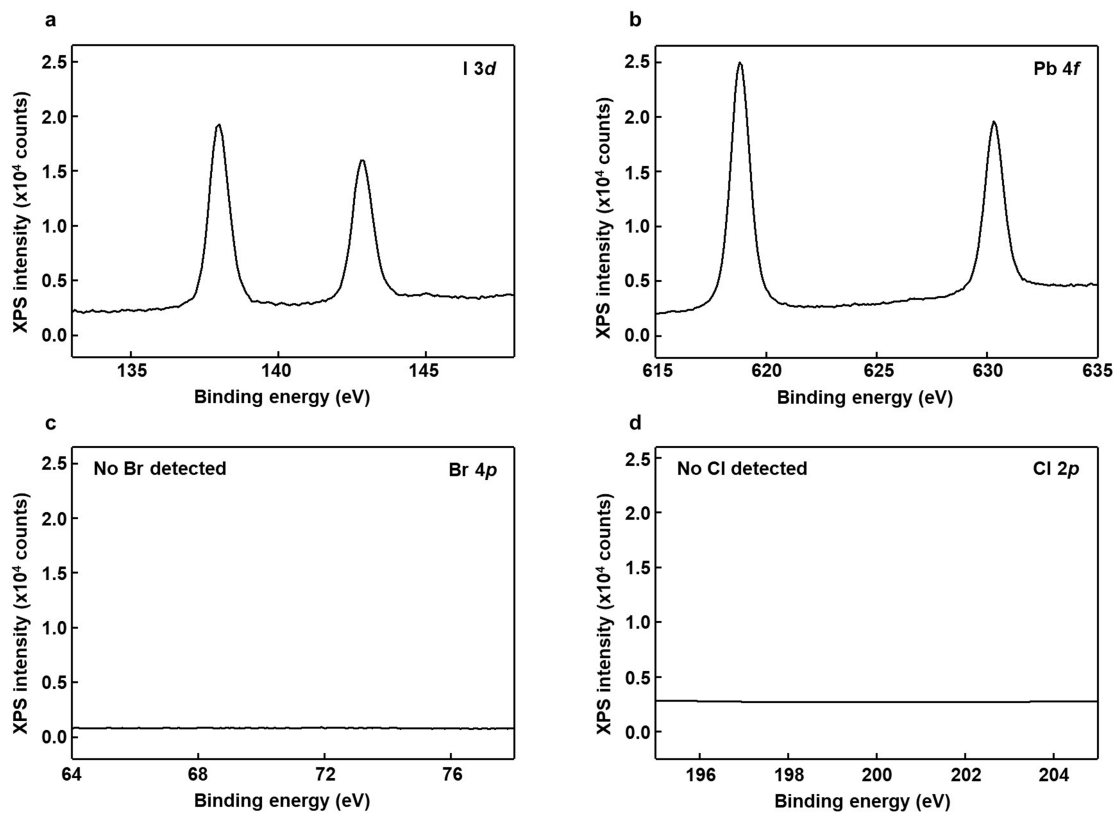
**Extended Data Fig. 6 | UPS spectra of  $\alpha$ -FAPbI<sub>3</sub> under different strains.** **a.** The intersects of the curves with the baseline in the high-binding-energy region give the Fermi level position of corresponding strained  $\alpha$ -FAPbI<sub>3</sub> films. There is a clear shift of the intersects to higher-binding-energy levels when the compressive strain becomes larger. **b.** The intersects of the curves with the

baseline in the low-binding-energy region give the energy difference between the Fermi level and the VBM. All  $\alpha$ -FAPbI<sub>3</sub> films have p-type character according to the calculated Fermi level position in the bandgap. Meanwhile, the VBM is pushed up more than the CBM with increasing strain. Inset, a schematic band diagram of the  $\alpha$ -FAPbI<sub>3</sub> under different strains.

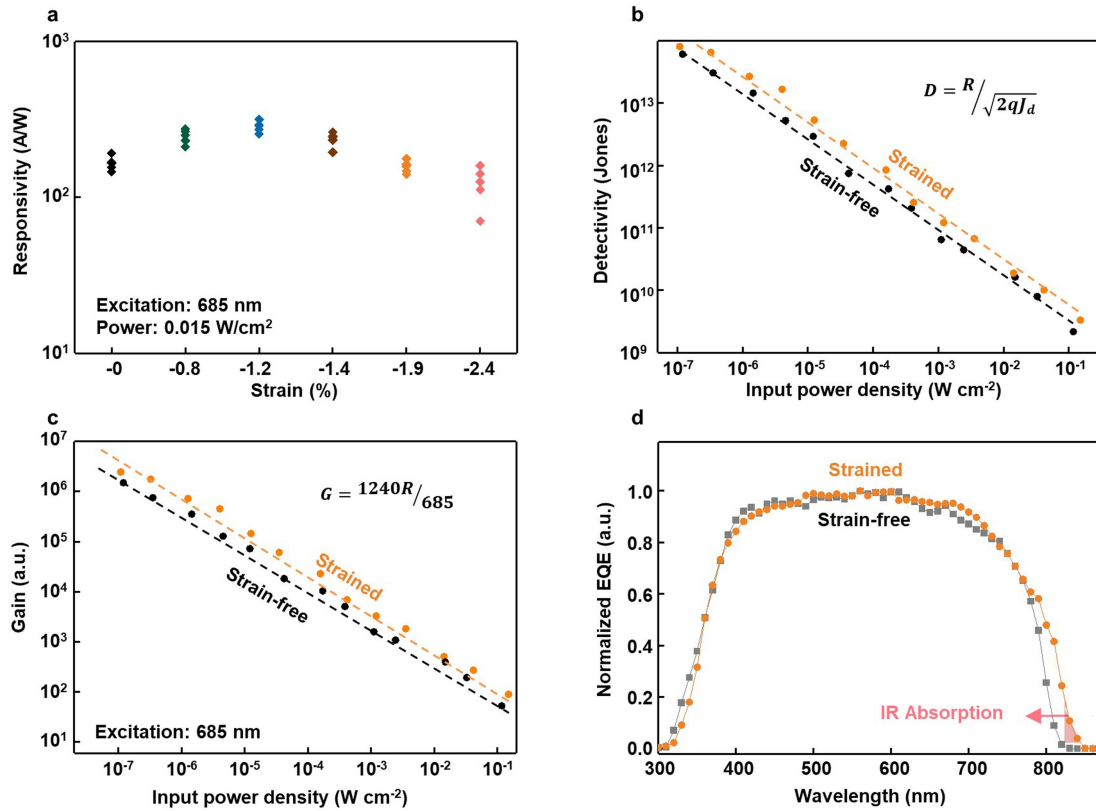


**Extended Data Fig. 7 | Space-charge-limited-current measurement of the epitaxial  $\alpha$ -FAPbI<sub>3</sub> with different strains.** a–d,  $I$ - $V$  characteristic curves for the space-charge-limited-current measurement of the epitaxial  $\alpha$ -FAPbI<sub>3</sub> film with different strains. While the forward scans indicate a typical trap-filling

process with increasing the applied voltage, the reverse scan doesn't show a detrapping process. Number of experiments,  $n = 5$  for each strain value.  $n_{\text{trap}}$ , calculated trap density.



**Extended Data Fig. 8 | XPS spectra of strained  $\alpha$ -FAPbI<sub>3</sub>.** XPS spectra of: **a**, I 3d; **b**, Pb 4f; **c**, Br 4p; and **d**, Cl 2p photoelectrons from a strained  $\alpha$ -FAPbI<sub>3</sub> film. Results show that Br and Cl are absent in the strained  $\alpha$ -FAPbI<sub>3</sub>.



**Extended Data Fig. 9 | Photoconductor-type photodetector characterizations with a 685-nm laser.** **a**, Responsivity as a function of strain level in  $\alpha$ -FAPbI<sub>3</sub>. Devices under  $-0.8\%$ ,  $-1.2\%$  and  $-1.4\%$  compressive strain give better responsivity compared to the strain-free devices. Further increasing the compressive strain can lead to a higher density of dislocations, which reduces the responsivity. Number of experiments,  $n = 5$  for each strain value.

**b, c**, Detectivity (**b**) and gain  $G$  (**c**) of the photodetector based on  $\alpha$ -FAPbI<sub>3</sub> under  $-1.2\%$  strain, indicating enhanced performance.  $q$ , element charge.  $J_d$ , dark current density. **d**, Normalized external quantum efficiency (EQE) of the photodetector based on  $\alpha$ -FAPbI<sub>3</sub> under  $-1.2\%$  strain, showing an extended infrared absorption range.

---

**Supplementary information**

---

**Strain engineering and epitaxial stabilization of halide perovskites**

---

In the format provided by the authors and unedited

Yimu Chen, Yusheng Lei, Yuheng Li, Yugang Yu, Jinze Cai, Ming-Hui Chiu, Rahul Rao, Yue Gu, Chunfeng Wang, Woojin Choi, Hongjie Hu, Chonghe Wang, Yang Li, Jiawei Song, Jingxin Zhang, Baiyan Qi, Muyang Lin, Zhuorui Zhang, Ahmad E. Islam, Benji Maruyama, Shadi Dayeh, Lain-Jong Li, Kesong Yang, Yu-Hwa Lo & Sheng Xu



1 **Supplementary Information for:**

2 **Strain engineering and epitaxial stabilization of halide perovskites**

3 Yimu Chen<sup>1,8</sup>, Yusheng Lei<sup>1,8</sup>, Yuheng Li<sup>1</sup>, Yugang Yu<sup>2</sup>, Jinze Cai<sup>2</sup>, Ming-Hui Chiu<sup>3</sup>, Rahul Rao<sup>4</sup>, Yue Gu<sup>2</sup>,  
4 Chunfeng Wang<sup>1</sup>, Woojin Choi<sup>5</sup>, Hongjie Hu<sup>2</sup>, Chonghe Wang<sup>1</sup>, Yang Li<sup>1</sup>, Jiawei Song<sup>2</sup>, Jingxin Zhang<sup>2</sup>,  
5 Baiyan Qi<sup>2</sup>, Muyang Lin<sup>1</sup>, Zhuorui Zhang<sup>1</sup>, Ahmad E. Islam<sup>4</sup>, Benji Maruyama<sup>4</sup>, Shadi Dayeh<sup>1,2,5</sup>, Lain-Jong  
6 Li<sup>3,6</sup>, Kesong Yang<sup>1</sup>, Yu-Hwa Lo<sup>2,5</sup>, Sheng Xu<sup>1,2,5,7\*</sup>

7  
8 <sup>1</sup>Department of Nanoengineering, University of California San Diego, La Jolla, CA 92093, USA.

9 <sup>2</sup>Materials Science and Engineering Program, University of California San Diego, La Jolla, CA 92093, USA.

10 <sup>3</sup>Physical Science and Engineering Division, King Abdullah University of Science and Technology, Thuwal,  
11 23955, Kingdom of Saudi Arabia.

12 <sup>4</sup>Materials and Manufacturing Directorate, Air Force Research Laboratory, Wright Patterson Air Force  
13 Base, Dayton, Ohio 45433, USA.

14 <sup>5</sup>Department of Electrical and Computer Engineering, University of California San Diego, La Jolla, CA 92093,  
15 USA.

16 <sup>6</sup>School of Materials Science and Engineering, University of New South Wales, Sydney 2052, Australia.

17 <sup>7</sup>Department of Bioengineering, University of California San Diego, La Jolla, CA 92093, USA.

18 <sup>8</sup>These authors contributed equally: Yimu Chen, Yusheng Lei.

19 \*e-mail: [shengxu@ucsd.edu](mailto:shengxu@ucsd.edu)

## 20 **Supplementary Discussion 1: Current Methods to Strain Halide Perovskites**

21 Strain engineering of halide perovskites is now receiving increasing attention in the  
22 field to improve the device performance by understanding device physics and improving  
23 materials quality. Different from the conventional semiconductors and perovskite oxides, the  
24 controllable strain engineering by heteroepitaxial growth of halide perovskites has not been  
25 achieved yet, to the authors' best knowledge, which is due to inappropriate growth methods  
26 and the absence of suitable lattice-mismatched substrates, therefore the lack of strong  
27 chemical bonds formed with the substrates.

28 Epitaxial growth of halide perovskites has been reported by many groups, but most of  
29 the works have been van der Waals epitaxy that is absent from strong interfacial chemical  
30 bonds<sup>1-3</sup>. Despite the weak nature of van der Waals bonds, nontrivial effects from van der  
31 Waals interaction to the epitaxial halide perovskites have been demonstrated due to the soft  
32 nature of halide perovskites<sup>4</sup>. Besides van der Waals epitaxy, chemical epitaxy by forming  
33 interfacial ionic bonds has also been reported<sup>5,6</sup>. However, due to the extremely high growth  
34 temperature (~500 °C), the interface was destroyed by the high diffusion rate of ions at such a  
35 high temperature and therefore, no interfacial strain could be detected. Other than epitaxial  
36 strain, thermally strained halide perovskites have also been studied. The thermal expansion  
37 coefficient difference between a patterned substrate and the halide perovskite was utilized to  
38 induce thermal strain to a perovskite microcrystal<sup>7</sup>. A thermally strained halide perovskite by  
39 introducing a phase transition of the substrate via increasing the temperature has also been  
40 demonstrated<sup>8</sup>. In this case, the thermal strain is highly dependent on the temperature and the  
41 magnitude of the strain cannot be well controlled.

42 Besides manipulating single crystalline halide perovskites, researchers are also creating  
43 strain in polycrystalline thin films by a variety of methods. One of the most popular methods  
44 is the ion substitution of a larger/smaller ion that can induce local tensile/compressive strain  
45 in the perovskite lattice<sup>9,10</sup>. Local compressive strain by small ion substitution was found to  
46 improve the stability of halide perovskites<sup>10</sup>. It was demonstrated that the local compressive  
47 strain by ion substitution could suppress the vacancy formation in halide perovskites<sup>9</sup>.  
48 Additionally, the crystalline quality of halide perovskites could be controlled by local strain  
49 via ion substitution<sup>11</sup>. Besides ion substitution, it was also reported the control of the local  
50 strain by light-induced lattice expansion<sup>12</sup>. The local strain was found to affect the  
51 optoelectronic properties of halide perovskites by creating defect distribution heterogeneity<sup>13</sup>.  
52 Recently, residual strain in polycrystalline halide perovskite films induced by the thermal  
53 annealing process has been reported. The residual strain in the polycrystalline  
54 methylammonium lead iodide film was found to have an impact on the perovskite stability<sup>14</sup>.  
55 Also, residual strain in the polycrystalline mixed halide perovskite film was reported to affect  
56 the carrier dynamics<sup>15</sup> and phase transition<sup>16</sup>. Hydrostatic pressurization was another  
57 commonly used method to apply strain to the halide perovskites. The crystal structure<sup>17</sup> and  
58 electronic band structure including bandgap<sup>18</sup> and carrier dynamics<sup>19,20</sup> were found to be  
59 highly subjective to the applied pressure. Metallic properties of halide perovskites were also  
60 reported under applied pressure<sup>21</sup>.

61 While all of these efforts demonstrated interesting strain engineering of halide  
62 perovskites, a controllable and scalable method for strain engineering single crystal halide  
63 perovskites is still critically needed. The epitaxially strained halide perovskite demonstrated

64 in this study meets this need by realizing the precise control of the strain in terms of  
65 magnitude and uniformity. The chemical bonds formed at the interface, rather than the weak  
66 van der Waals interactions, not only provide strong epitaxial strain to effectively alter the  
67 material structure and properties but also endow stability against environmental fluctuations  
68 so that the strain can maintain under different temperatures and pressures, which are  
69 qualitatively different from the thermally strained and the pressurized perovskites. The  
70 magnitude of the strain can be precisely controlled by designing different lattice mismatch  
71 rather than the residual strain that shows uncertainty and uncontrollability. Enhanced optical  
72 and electrical properties have been shown in the strained halide perovskites. Therefore, this  
73 method represents a significant scientific advance compared with other reported studies to  
74 strain halide perovskites.

75

76

## 77 **Supplementary Discussion 2: Characterizing MAPbCl<sub>x</sub>Br<sub>3-x</sub> Substrates and Strain-free** 78 **α-Formamidinium Lead Iodide (α-FAPbI<sub>3</sub>)**

79 Supplementary Fig. 1a shows the X-ray Diffraction (XRD)  $\theta$ - $2\theta$  scan pattern of  
80 strain-free  $\alpha$ -FAPbI<sub>3</sub> powder<sup>22</sup>. For the cubic crystal structure, the lattice parameter can be  
81 calculated by:

$$\lambda = 2d_{hkl}\sin\theta$$

82 where  $\lambda$  is the incident beam wavelength,  $\theta$  is the angle of incidence, and  $d_{hkl}$  is the  
83 lattice d-spacing. For strain-free  $\alpha$ -FAPbI<sub>3</sub>, the (001) peak position is at 13.92° and the  
84 corresponding lattice parameter is calculated to be 6.35 Å. All other peaks in the XRD pattern

85 are labeled and the corresponding lattice parameters can be calculated similarly.

86 Supplementary Fig. 1b shows a collection of the (001) peak locations from mixed  
87 methylammonium lead chloride/bromide ( $\text{MAPbCl}_x\text{Br}_{3-x}$ ) single crystal substrates, which,  
88 regardless of the Cl/Br ratio, are reported to have a cubic structure<sup>23</sup>. The peak position shifts  
89 to a higher  $2\theta$  angle with increasing Cl ratio, indicating a decrease in the lattice parameter.

90 The  $\text{MAPbCl}_x\text{Br}_{3-x}$  substrates are grown by solvent evaporation of different molar ratios  
91 of  $\text{MAPbCl}_3$  and  $\text{MAPbBr}_3$  solutions. With the lattice parameters derived from XRD  
92 measurements, the actual compositions of the substrates can be calculated by Vegard's  
93 Law<sup>24</sup>:

$$a_{\text{MAPbCl}_{1-x}\text{Br}_x} = (1 - x)a_{\text{MAPbCl}_3} + xa_{\text{MAPbBr}_3}$$

94 where  $a_{\text{MAPbCl}_{1-x}\text{Br}_x}$  is the lattice parameter of the mixed crystal, and  $a_{\text{MAPbCl}_3}$  and  
95  $a_{\text{MAPbBr}_3}$  are the lattice parameters of  $\text{MAPbCl}_{3.00}\text{Br}_{0.00}$  and  $\text{MAPbCl}_{0.00}\text{Br}_{3.00}$  single crystals,  
96 respectively. The Cl/Br molar ratios of the precursors, the composition of the  $\text{MAPbCl}_x\text{Br}_{3-x}$   
97 crystal, and the calculated lattice parameters are summarized in Supplementary Table 1.

98

99

### 100 **Supplementary Discussion 3: Strained Epitaxial Growth of $\alpha$ -FAPbI<sub>3</sub>**

101 Supplementary Table 2 summarizes the (001) XRD peak positions of the epitaxial  
102  $\alpha$ -FAPbI<sub>3</sub> on different substrates. All epitaxial samples have a shift of the (001) peak to a  
103 lower  $2\theta$  angle compared with the peak position of the strain-free crystal (13.92°), indicating  
104 an increase of the out-of-plane lattice parameter due to the in-plane compressive strain. The  
105 epitaxial  $\alpha$ -FAPbI<sub>3</sub> on  $\text{MAPbCl}_{0.00}\text{Br}_{3.00}$  substrate shows a minimum shift to 13.89°. When

106 more Cl is incorporated into the substrate, the lattice mismatch between  $\alpha$ -FAPbI<sub>3</sub> and the  
107 substrate increases. The (001) XRD peak of the epitaxial  $\alpha$ -FAPbI<sub>3</sub> will further shift to a  
108 lower  $2\theta$  angle, indicating a further increase of the out-of-plane lattice spacing and a stronger  
109 in-plane compressive strain. The strain values are calculated by comparing the in-plane lattice  
110 parameter of strain-free  $\alpha$ -FAPbI<sub>3</sub> and epitaxial  $\alpha$ -FAPbI<sub>3</sub>, showing a tunable strain as high  
111 as -2.4%.

112 The epitaxial growth conditions are systematically studied (Supplementary Fig. 1c, d).  
113 FAPbI<sub>3</sub> solutions with different concentrations are deposited on the substrates at different  
114 temperatures for epitaxial growth. Since FAPbI<sub>3</sub> has an inverse solubility in the  
115  $\gamma$ -Butyrolactone (GBL) solvent, high concentration and high temperature will accelerate the  
116 crystallization of  $\alpha$ -FAPbI<sub>3</sub>. In Supplementary Fig. 1c, the (001) peak position of the  
117 epitaxial  $\alpha$ -FAPbI<sub>3</sub> is studied as a function of the growth temperature. The vertical orange  
118 line labels the peak position (13.92°) of the strain-free  $\alpha$ -FAPbI<sub>3</sub>. The results show that  
119 growth temperatures below 180°C always generate diffraction peaks larger than 13.92°, while  
120 growth temperatures above 180°C can generate peaks smaller than 13.92°. The diffraction  
121 peak position reveals the out-of-plane lattice parameter of the epitaxial thin film. When the  
122 growth temperature is too high, crystallization of  $\alpha$ -FAPbI<sub>3</sub> is fast and many defects are  
123 incorporated, which would relax the strain in the  $\alpha$ -FAPbI<sub>3</sub>. When the growth temperature is  
124 too low, the crystallization is too slow and Cl<sup>-</sup>/Br<sup>-</sup> ions may dissolve from the substrate and  
125 re-crystallize into the epitaxial  $\alpha$ -FAPbI<sub>3</sub>, forming mixed alloys at the interface, although  
126 MAPbCl<sub>x</sub>Br<sub>3-x</sub> has an extremely low solubility in GBL. Diffraction peaks larger than 13.92°  
127 provide evidence for uniform lattice contraction caused by the incorporation of smaller Br<sup>-</sup>

128 and Cl<sup>-</sup> ions.

129 The epitaxial growths with different FAPbI<sub>3</sub> precursor concentrations are also  
130 investigated (Supplementary Fig. 1d). Similar to the effect of temperature, FAPbI<sub>3</sub> precursor  
131 concentrations that are too high will result in fast crystallization and a high defect  
132 concentration. Precursor concentrations that are too low will lead to slow α-FAPbI<sub>3</sub>  
133 crystallization, and thus the incorporation of Cl<sup>-</sup>/Br<sup>-</sup> ions that form alloys at the interface.

134

135

#### 136 **Supplementary Discussion 4: Quality of the Epitaxial Films**

137 The crystalline quality of the substrate is found to have a significant impact on the  
138 quality of the epitaxial thin film since defects in the substrates will propagate through the  
139 epitaxial layer and relax the strain. The substrate crystal quality prepared using the Inverse  
140 Temperature Crystallization (ITC)<sup>25</sup> (Extended Data Fig. 1a) and the Slow Solvent  
141 Evaporation (SSE) methods (Extended Data Fig. 1b to 1f) are systematically characterized.  
142 The Full Width at Half Maximum (FWHM) value in rocking curve measurements  
143 characterizes crystal mosaicity. Substrates grown by the SSE method show a much smaller  
144 FWHM value (~0.020°) compared with those by the ITC method (~0.084°) due to the  
145 extremely slow crystallization speed of SSE, indicating a higher crystal quality of substrates  
146 prepared by the SSE than those by the ITC.

147 Extended Data Fig. 1g shows (001) XRD patterns of epitaxial α-FAPbI<sub>3</sub> grown on  
148 substrates with high quality (red curve) and low quality (black curve). For α-FAPbI<sub>3</sub> grown  
149 on the high-quality substrate, the FWHM of the XRD peak is also smaller than α-FAPbI<sub>3</sub>



150 grown on the low-quality substrate. Additionally, the epitaxial  $\alpha$ -FAPbI<sub>3</sub> grown on the  
151 high-quality substrate maintains the strained status with a shifted diffraction peak while the  
152 epitaxial  $\alpha$ -FAPbI<sub>3</sub> grown on the low-quality substrate has a (001) peak close to that of the  
153 strain-free sample at 13.92° (position of the dashed line).

154 Evidence for the strain relaxation and the growth model can also be found by studying  
155 the surface topography of the epitaxial crystal. Atomic force microscopy is used to  
156 characterize topographic features of a fully strained film and a fully relaxed film under the  
157 tapping mode. The topography of the fully strained film (Extended Data Fig. 2a) shows a  
158 smooth surface with small terrains. The stepwise height profile (Extended Data Fig. 2b)  
159 corresponds to the red line in Extended Data Fig. 2a. Each step has a height of ~0.64 nm, the  
160 same as the height of a strained  $\alpha$ -FAPbI<sub>3</sub> unit cell. This reveals that the epitaxial growth of  
161  $\alpha$ -FAPbI<sub>3</sub> follows a layer-by-layer model<sup>26</sup>. Besides, no obvious cracks or pits can be  
162 observed, indicating a coherent growth of the epitaxial layer on the mismatched substrate.

163 The areal elastic strain energy will increase with the epitaxial layer thickness, which  
164 leads to the formation of defects (e.g., dislocations) that relax the strain energy. Also, the  
165 dislocations will glide and propagate to form cracks and pits at the surface of the epitaxial  
166 layer. The rough surface of the fully relaxed film shows the existence of such dislocations  
167 (Extended Data Fig. 2c). The corresponding height profile shows a very rough surface  
168 morphology, which indicates strain relaxation (Extended Data Fig. 2d).

169  $\alpha$ -FAPbI<sub>3</sub> fails to epitaxially grow on substrates with a Cl ratio higher than 50% (i.e.,  
170 higher Cl content than that in MAPbCl<sub>1.50</sub>Br<sub>1.50</sub>), because higher levels of lattice mismatch  
171 will dramatically increase the strain energy and make the epitaxial growth less

172 thermodynamically favorable. Supplementary Fig. 2b shows the optical image of growth  
173 results on a  $\text{MAPbCl}_{2.00}\text{Br}_{1.00}$  substrate prepared using the same method as the other  
174 substrates. In this case, the  $\alpha$ -FAPbI<sub>3</sub> randomly crystallizes on the substrate, without forming  
175 a uniform epilayer; most of the black  $\alpha$ -FAPbI<sub>3</sub> crystals undergo a phase transition to yellow  
176  $\delta$ -FAPbI<sub>3</sub> due to the phase instability of  $\alpha$ -FAPbI<sub>3</sub> at room temperature.

177

178

### 179 **Supplementary Discussion 5: Mechanisms of XRD Diffraction Peak Broadening**

180 For XRD diffraction peak broadening, common reasons include<sup>27</sup>: 1) lattice strain, 2)  
181 crystalline dimension, 3) misorientation induced by defects, 4) thermal movement of the  
182 atoms around the equilibrium states, and 5) instrumental effects like focusing imperfection.  
183 The fourth and fifth reasons are irrelevant to this study.

184 We attribute the main contributions of the diffraction peak broadening in Fig. 1c to the  
185 increased lattice strain and the reduced crystalline dimension rather than the misorientation.  
186 Based on the Williamson-Hall equation<sup>28</sup>, the diffraction peak FWHM is linearly related to  
187 the lattice strain and reversely related to the crystalline dimension<sup>27</sup>. In fact, such diffraction  
188 peak broadening is commonly reported in thin film heteroepitaxial growth where the thin  
189 epitaxial films usually exhibit broader diffraction peaks due to the lattice strain and low  
190 thickness<sup>29</sup>.

191 In general, dislocation-induced lattice distortion and misorientation can also lead to  
192 broadening of the XRD diffraction peaks. For the strain relaxation of the epitaxial film,  
193 however, the diffraction peak broadening due to the dislocations usually leads to a huge

194 broadening that is several times broader than that of the free-standing materials and the  
195 fully-strained materials<sup>30</sup>. We investigate the FWHM of the diffraction peaks in the epitaxial  
196  $\alpha$ -FAPbI<sub>3</sub> thin film under different strains. Results show that the diffraction peak FWHM of  
197 the free-standing single crystals is  $\sim 0.05^\circ$  while the diffraction peak FWHM of the epitaxial  
198  $\alpha$ -FAPbI<sub>3</sub> thin film is  $\sim 0.07^\circ$ , suggesting a small broadening rather than the large broadening  
199 by the strain relaxation (Supplementary Fig. 3a).

200 We study the diffraction peak FWHM of the strained and the strain-relaxed  $\alpha$ -FAPbI<sub>3</sub>  
201 thin films in Extended Data Fig. 1g. Note that in this case, we exclude the influence of the  
202 thickness-induced diffraction broadening by using films with the same thickness. Strain is  
203 relaxed by adopting a substrate with a high density of dislocations for the epitaxial growth.  
204 The XRD diffraction patterns shown in Extended Data Fig. 1g indicates that the strained  
205 epitaxial  $\alpha$ -FAPbI<sub>3</sub> thin film shows a shift to the lower diffraction angle due to the in-plane  
206 compressive strain compared with that of the strain-relaxed epitaxial  $\alpha$ -FAPbI<sub>3</sub> thin film. A  
207 broadening effect due to the high dislocation density of the strain-relaxed epitaxial  $\alpha$ -FAPbI<sub>3</sub>  
208 thin film is also shown. Statistical study of the diffraction peak FWHM (Supplementary Fig.  
209 3b) shows that the diffraction peak of the strain-relaxed  $\alpha$ -FAPbI<sub>3</sub> is much broader  
210 (FWHM $\sim 0.25^\circ$ ) than that of the strained  $\alpha$ -FAPbI<sub>3</sub> (FWHM $\sim 0.07^\circ$ ). Therefore, we can  
211 conclude that the broadening in the XRD diffraction peak in Fig. 1c is not due to strain  
212 relaxation.

213

214

215 **Supplementary Discussion 6: Raman Spectroscopy and Simulation**

## 216 **1. Discussion of the Raman spectroscopy measurement**

217 Full Raman spectra of the strain-free (Supplementary Fig. 4a) and the -2.4% strained  
218 (Supplementary Fig. 4b)  $\alpha$ -FAPbI<sub>3</sub> show that there is only one peak in the region between 0  
219  $\text{cm}^{-1}$  and 1200  $\text{cm}^{-1}$ , which can be attributed to the vibration of Pb-I bonds<sup>22,31</sup>. Note that the  
220 broad shoulder peak at  $\sim 250 \text{ cm}^{-1}$  in the strain-free sample is attributed to the Pb-O bond  
221 from the oxidation of Pb-I bond induced by the incident laser<sup>31</sup>. During the fitting process,  
222 the spectra were fitted with both Pb-I and Pb-O peaks, while only the Pb-I peaks were shown  
223 in Fig. 1f.

224 Raman spectroscopy is also used to study the substrates (Supplementary Fig. 4e) using a  
225 488-nm laser as the excitation source. No Raman signals can be detected from these  
226 substrates in the wavenumber range of interest. Therefore, all Raman signals in this study are  
227 originated from the epitaxial thin film.

228 Thickness-dependent Raman study is based on epitaxial  $\alpha$ -FAPbI<sub>3</sub> thin films on  
229 substrates with the same composition. The results show that increasing the epitaxial thin film  
230 thickness will cause strain relaxation (Supplementary Fig. 4f). The trend is similar to the  
231 strain-dependent Raman spectra in Fig. 1e.

232

## 233 **2. Raman spectra simulation and peak broadening**

234 The peaks are fitted, and the peak broadening can be attributed to the emergence of a  
235 shoulder peak due to the strain-induced out-of-plane bond elongation. This phenomenon is  
236 also reported in other strain-dependent Raman studies<sup>32-34</sup>.

237 To further confirm that the peak broadening in the Raman spectra originates from the  
238 strain-induced lattice deformation, we simulate the Raman spectra with first-principles  
239 calculations by the CASTEP in Materials Studios. The Raman spectra are simulated from 100  
240  $\text{cm}^{-1}$  to 400  $\text{cm}^{-1}$  to compare with the experimental data.

241 Supplementary Fig. 4c shows the comparison between the experimental and simulated  
242 Raman spectra of the strain-free  $\alpha$ -FAPbI<sub>3</sub> lattice. Simulated results show a Raman peak at  
243 124  $\text{cm}^{-1}$ , which can be assigned to the stretching of the Pb-I bond. This is correlated with the  
244 Raman peak at  $\sim 136 \text{ cm}^{-1}$  in the experimental result. Underestimations of the simulated  
245 Raman peak wavenumbers are commonly reported<sup>35-37</sup>. Possible explanations may be that the  
246 anharmonicity of the bonds and the van der Waals interactions (between the inorganic cages  
247 and organic cations) can affect the simulated results<sup>36</sup>. Besides, the assignment of the Pb-I  
248 stretching peak also agrees with the reported studies<sup>38,39</sup>. Meanwhile, we also identify a weak  
249 peak at 377  $\text{cm}^{-1}$  from the simulated Raman spectrum, which can be assigned to the bending  
250 of the FA<sup>+</sup> cation. However, this peak vanishes in the experimental spectrum, probably  
251 because the organic cations in halide perovskites are highly dynamic in the inorganic  
252 framework<sup>40-42</sup>. The reorientation of the cation will lead to the weakening of the peak under  
253 room temperature<sup>43</sup>. This is also the reason why low-temperature Raman, which can freeze  
254 the orientation of the organic cation, can resolve the signal from the organic cations in halide  
255 perovskites<sup>36,43</sup>. Note that the weak Raman band at  $\sim 250 \text{ cm}^{-1}$  from the experimental Raman  
256 spectrum is assigned to the Pb-O bond induced by the laser oxidation<sup>38</sup>.

257 We then apply -2.4% strain to the  $\alpha$ -FAPbI<sub>3</sub> lattice and comparison between the  
258 experimental and simulated Raman spectra of the strained  $\alpha$ -FAPbI<sub>3</sub> lattice is shown in

259 Supplementary Fig. 4d. An obvious peak splitting due to the in-plane Pb-I bond compression  
260 and the out-of-plane Pb-I bond stretching can be observed from the simulated Raman  
261 spectrum. This agrees with the experimental Raman peak, which shows obvious broadening  
262 due to the peak splitting. In fact, the strain-induced Raman peak splitting is also reported in  
263 other materials<sup>32-34</sup>. We also notice the increase of the peak intensity, which is due to the  
264 breakage of the Raman-inactive cubic symmetry<sup>44</sup>.

265 Therefore, we demonstrate that the Raman peak broadening originates from the  
266 strain-induced peak splitting. Strain leads to the in-plane compression and out-of-plane  
267 stretching of the Pb-I bonds in the  $\alpha$ -FAPbI<sub>3</sub> lattice, splitting the Pb-I stretching peak, and  
268 broadening the peak FWHM.

269

270

### 271 **Supplementary Discussion 7: First-Principles Calculations of the Strained $\alpha$ -FAPbI<sub>3</sub>**

272 First-principles calculations allow a better understanding of the structural deformation  
273 and prediction of any emerging new properties. Cubic  $\alpha$ -FAPbI<sub>3</sub> unit cells are calculated with  
274 the N-N axis of the FA<sup>+</sup> cation along (001), (101), and (111), respectively (left panel of  
275 Extended Data Fig. 3a). These three low Miller index directions represent FA's typical  
276 orientations, and their calculated total energies could reveal potential orientation preferences.  
277 As the first step, we optimized the cubic lattice parameter  $a$  for each orientation to obtain the  
278 lowest total energy. Our calculations show  $a = 6.35$  Å for the FA along (001),  $a = 6.40$  Å for  
279 the FA along (101), and  $a = 6.37$  Å for the FA along (111). The optimized structure with the  
280 FA along (101) has the lowest total energy of -52.73 eV, and the optimized structure with the

281 FA along (001) shows the highest total energy of -52.68 eV. The total energy difference  
282 between these two structures is within 50 meV, and thus the structural model with FA along  
283 (101) direction was used in our calculations.

284 Then we applied bi-axial strains in the *ab*-plane of the optimized structure for each  
285 orientation. The range is from 3% tensile strain to -3% compressive strain. The strained cells  
286 keep their original FA orientation after optimization along the z-direction. For bandgap  
287 calculations, spin-orbit coupling (SOC) was incorporated due to the heavy element Pb, and  
288 hybrid functionals within Heyd–Scuseria–Ernzerhof (HSE) formalism with 25% Hartree–  
289 Fock (HF) exchange were employed. The calculated bandgap energy (lower right of  
290 Extended Data Fig. 3a) and cell volume (upper right of Extended Data Fig. 3a) are displayed  
291 as a function of the bi-axial strain. The cell volume decreases as the strain changes from  
292 tensile to compressive for each FA orientation. This is a result of the decreased *a* and *b* and  
293 slightly increased *c*. The bandgap decreases as well when the strain changes from tensile to  
294 compressive for each FA orientation.

295 Extended Data Fig. 3c shows the out-of-plane lattice deformation with different in-plane  
296 strain levels. A Poisson's ratio of around 0.3 can be calculated, consistent with the  
297 experimental value by reciprocal space mapping. Meanwhile, C-N and C=N bond lengths in  
298 FA<sup>+</sup> cation with different strain levels (Extended Data Fig. 3d) show no obvious changes with  
299 the strain, indicating a weak interaction between the FA<sup>+</sup> cation and the inorganic Pb-I  
300 framework.

301

302



### 303 **Supplementary Discussion 8: Bandgap Reduction of the Strained $\alpha$ -FAPbI<sub>3</sub>**

304 Fig. 2a shows photoluminescence (PL) spectra of the epitaxial  $\alpha$ -FAPbI<sub>3</sub> thin films at  
305 different strain levels. With increasing the in-plane compressive strain, a clear redshift can be  
306 seen from  $\sim 1.523$  eV to  $\sim 1.488$  eV. To confirm whether the redshift of PL peaks is caused by  
307 the in-plane compressive strain, several possible mechanisms are discussed.

308 It has been reported that as the perovskite thickness decreases, surface charges will  
309 induce depletion micro-electric field near the perovskite surface and increase the bandgap,  
310 which causes the PL to blueshift<sup>45,46</sup>, opposite to this case here. Thus, this surface field effect  
311 can be ruled out. We also rule out the possibility of reabsorption of short-wavelength photons  
312 by the material itself, which may cause PL redshift. This effect is only observed in bulk  
313 crystals and thick films ( $>1$   $\mu\text{m}$  in thickness) and can be neglected for  $<100$  nm films in Fig.  
314 2a<sup>47</sup>. Additionally, the possible incorporation of Br or Cl element is excluded since those  
315 foreign atoms will lead to PL blueshift<sup>48</sup>. Hence, we can conclude that the PL redshift is due  
316 to the compressive strain generated by the lattice mismatch.

317 The absorption spectrum is also studied to validate the bandgap measured by PL. Note  
318 that improper measurement methods can lead to inaccurate results in both absorption and PL.  
319 For example, the absorption spectrum of thick materials obtained by the transmission mode  
320 cannot distinguish the light being absorbed or being scattered due to the large thickness of the  
321 sample<sup>49</sup>. Meanwhile, PL emission peaks show dependence on the illumination intensity<sup>50</sup> as  
322 well as material dimensions<sup>45</sup>. Therefore, absorption and PL measurements can be used to  
323 validate each other.

324 Due to the large thickness (1 to 2 mm) and the high absorption coefficients ( $\sim 10^5 \text{ cm}^{-1}$ )  
325 of the substrates, light transmittance cannot be detected<sup>51</sup>. Therefore, we adopt the reflection  
326 mode of UV-VIS to detect the absorption onset of the samples. The collected absorption  
327 results (Extended Data Fig. 3b) also demonstrate a red-shift when the strain goes up, which is  
328 consistent with the PL measurements.

329 Meanwhile, we notice that there is a quantitative discrepancy between the calculated  
330 bandgap reduction ( $\sim 120 \text{ meV}$ ) and the experimental bandgap reduction ( $\sim 35 \text{ meV}$ ) under  
331  $-2.4\%$  compressive strain. Note that the first-principle calculations of the strain-dependent  
332 bandgap serve as a general prediction. The main purpose is to predict the trend of the change  
333 instead of showing quantitative agreement with experimental results. Due to the  
334 approximation in the exchange-correlation functionals, deviation in the order of  $10^2 \text{ meV}$  in  
335 calculated bandgap energy from experiments is within a reasonable and tolerable range.  
336 Additionally, the geometry approximation of the strained lattice model doesn't reveal the  
337 actual deformation of the strained lattice. For example, the lattice parameters  $a$  and  $b$  are set  
338 to be different values to mimic different in-plane biaxial strain levels in the simulation, which  
339 changes the bond length between atoms. In real lattice deformation, however, the bond angle  
340 will also change to accommodate the in-plane biaxial strain (e.g., by octahedral rotation).  
341 Therefore, the calculated values can be different from the experimental values.

342

343

#### 344 **Supplementary Discussion 9: Emission Peaks Broadening of the Strained $\alpha$ -FAPbI<sub>3</sub>**

345 PL FWHM of the epitaxially strained  $\alpha$ -FAPbI<sub>3</sub> thin film is shown to increase with the

346 strain (Supplementary Fig. 5). There are multiple possibilities origins of the PL broadening.  
347 We can first rule out the influence of the domain size because the sample is a single domain  
348 thin film<sup>52</sup>. For semiconductors, emission linewidth broadening is governed by charged  
349 carrier-phonon coupling, including crystalline quality, acoustic phonon scattering, optical  
350 phonon scattering, and impurity<sup>53</sup>. In semiconductors with heterojunctions, charged carrier  
351 transfer can also take place with specific band structure at the interfaces. Such charged carrier  
352 transfer usually leads to carrier quenching without direct recombination<sup>54-56</sup>, and emission  
353 peak shifting due to the energy change<sup>57</sup>, while very few reported PL broadening due to the  
354 carrier relaxation<sup>58</sup>. Here, we discuss the possible emission peak broadening mechanism in  
355 the epitaxially strained  $\alpha$ -FAPbI<sub>3</sub> thin films.

356

### 357 **1. Charge transfer**

358 The  $\alpha$ -FAPbI<sub>3</sub> grown on MAPbBr<sub>3</sub> is analyzed as an example.  $\alpha$ -FAPbI<sub>3</sub> has a very  
359 different band structure compared with MAPbBr<sub>3</sub> in terms of bandgap, valance band  
360 maximum (VBM), and conduction band minimum (CBM) as shown in Supplementary Fig. 6.  
361 The heterojunction shows a straddling band alignment where the charged carrier transfer is  
362 only allowed from the larger bandgap side to the smaller bandgap side when the larger  
363 bandgap side is excited. During the PL measurement in this study, a 633-nm laser  
364 (corresponding to 1.95 eV) was used for exciting the epitaxial layer (bandgap 1.50 eV)  
365 without exciting the substrates (bandgap 2.30 eV). Upon absorption, electrons in the  
366  $\alpha$ -FAPbI<sub>3</sub> will be excited to the conduction band while the MAPbBr<sub>3</sub> remains unexcited.

367 Here, the large barrier between  $\alpha$ -FAPbI<sub>3</sub> and MAPbBr<sub>3</sub> blocks the carrier transfer from the  
368  $\alpha$ -FAPbI<sub>3</sub> to the MAPbBr<sub>3</sub> across the interface (Supplementary Fig. 6).

369 This analysis also applies to other substrates MAPbCl<sub>x</sub>Br<sub>3-x</sub> in this study with different  
370 compositions from MAPbBr<sub>3</sub>. When incorporating more Cl into the MAPbBr<sub>3</sub> substrate, the  
371 bandgap will further increase by lifting up the CBM and pushing down the VBM, and the  
372 energy barrier between the  $\alpha$ -FAPbI<sub>3</sub> and the substrates will be even larger<sup>59</sup>. Thus,  
373 interfacial charge transport will be even less favorable.

374 Additionally, we also consider the carrier transfer from the MAPbBr<sub>3</sub> to the  $\alpha$ -FAPbI<sub>3</sub>.  
375 Since the MAPbBr<sub>3</sub> remains unexcited due to the large bandgap, the intrinsic electrons are  
376 extremely minor compared with the excited carrier in  $\alpha$ -FAPbI<sub>3</sub>. Therefore, we exclude the  
377 possibility of carrier transfer from the MAPbBr<sub>3</sub> to the  $\alpha$ -FAPbI<sub>3</sub>.

378 Considering that the laser for the PL measurement doesn't excite the carriers in the  
379 substrate, as well as the large energy barrier that blocks the interfacial carrier transfer  
380 between the epitaxial layer and the substrate, we draw the conclusion that the charged carrier  
381 transfer between the epitaxial layer and the substrates will not take place in the PL  
382 measurements and, therefore, will not contribute to the PL broadening.

383

## 384 **2. Emission broadening by charged carrier-phonon coupling**

385 For inorganic semiconductors, emission linewidth is associated with different  
386 mechanisms of scattering between charged carriers and phonons or impurities, which can be  
387 expressed as<sup>60</sup>:

$$\Gamma(T) = \Gamma_{\text{imp}} + \Gamma_{\text{ac}} + \Gamma_{\text{LO}} + \Gamma_0$$

388 where  $\Gamma(T)$  is the temperature-dependent emission linewidth,  $\Gamma_{\text{imp}}$  is the broadening terms  
389 of scattering with impurities,  $\Gamma_{\text{ac}}$  and  $\Gamma_{\text{LO}}$  are the broadening terms of the scattering from  
390 the acoustic phonons and the optical phonons, and  $\Gamma_0$  is a temperature-independent  
391 broadening term associating with the scattering due to the structural disorder, respectively.

392

## 393 **2.1 Impurity**

394 Experimentally speaking, as mentioned above, impurity during epitaxial growth can be  
395 controlled by adopting the same growth solutions and epitaxial growth protocol. Therefore,  
396 the impurity in the epitaxial films will have a similar concentration. The influence on the PL  
397 FWHM from impurity variation will be very minimal.

398 Additionally, theoretical studies have identified that impurity scattering should be an  
399 inhomogeneous broadening term for PL FWHM in halide perovskites<sup>53,61</sup> and other  
400 semiconductors<sup>62</sup>, which should show a weak temperature dependence. This is because  
401 impurities can lead to local electric field heterogeneity, and the existence and scattering of  
402 impurities are independent on the temperature. The PL FWHM will not change much with  
403 the temperature. However, experiments have shown a homogeneous broadening behavior of  
404 the PL FWHM of halide perovskites, with a strong temperature dependency<sup>53,61</sup>. Therefore,  
405 the contribution of impurity-induced emission broadening of the PL FWHM is considered to  
406 be minor in halide perovskites.

407

## 408 **2.2 Acoustic phonon scattering**

409 As we mentioned above, the temperature-dependent PL FWHM of halide perovskites  
410 shows a homogeneous behavior, which can be attributed to optical phonon and acoustic  
411 phonon scattering<sup>53,61</sup>. This is due to the fact that acoustic and optical phonons are strongly  
412 temperature-dependent. However, the contribution of the acoustic scattering  $\Gamma_{ac}$  in the  
413 emission broadening is also demonstrated to be minor in halide perovskites<sup>61</sup>. According to  
414 the expression equation of the acoustic scattering,  $\Gamma_{ac}$  is linearly proportional to the  
415 temperature<sup>61</sup>. However, the experimental temperature-dependent PL FWHM of halide  
416 perovskites, especially FAPbI<sub>3</sub>, behave nonlinearly with temperature<sup>61</sup>. This is due to the fact  
417 that the polar Pb-I bond mainly generates optical phonons. Therefore, the contribution of the  
418 acoustic phonon scattering to the emission linewidth broadening is considered to be minor,  
419 and the optical phonon scattering is the dominating factor.

420

### 421 2.3 Temperature-dependent PL FWHM study

422 As demonstrated by extensive prior works<sup>53,61,63,64</sup>, the above equation can be expressed  
423 in the following form, with the consideration that the acoustic phonon scattering and the  
424 impurity scattering contribute little to the emission linewidth in halide perovskites:

$$\Gamma(T) = \Gamma_{LO} + \Gamma_0 = \frac{\gamma_{LO}}{e^{\left(\frac{E_{LO}}{k_b T}\right)} - 1} + \Gamma_0$$

425 where  $\gamma_{LO}$  is the charged carrier-optical phonon coupling constant,  $E_{LO}$  is the energy of the  
426 optical phonon, and  $k_b$  is the Boltzmann constant. Based on this equation, we studied the  
427 relationship between PL FWHM and the temperature for the strained and the strain-free  
428  $\alpha$ -FAPbI<sub>3</sub> (Extended Data Fig. 4a, b). A clear redshift can be observed while the intensity of

429 the emission peak increases with reducing the temperature due to the reduced scattering  
430 between the phonon and carriers at low temperatures. To better reveal the change in bandgap  
431 and FWHM as a function of the temperature, we normalize each of the PL peak intensity  
432 (Extended Data Fig. 4c, d). With decreasing the temperature, both strained and strain-free  
433  $\alpha$ -FAPbI<sub>3</sub> showed a bandgap narrowing, which is attributed to the contraction of the lattice.  
434 Meanwhile, the PL FWHM exhibits a uniform narrowing with decreasing the temperature.  
435 Extended Data Fig. 4e, f show the PL FWHM as a function of the temperature for a -2.4%  
436 strained and a strain-free sample, respectively.

437 Data were fitted with the equation introduced above. Fitted results indicate the main  
438 increment of  $\Gamma_0$  in the strained sample can be attributed to the increased scattering by the  
439 crystalline quality reduction. Meanwhile, the increment of both  $\gamma_{LO}$  and  $E_{LO}$  suggests an  
440 enhanced charged carrier-optical phonon coupling and higher phonon energy in the strained  
441 lattice, which can be attributed to the strain-induced lattice deformation<sup>65</sup>. Therefore, we can  
442 conclude that the PL FWHM difference of the strained and the strain-free sample mainly  
443 comes from the increased scattering by the strain-induced crystalline quality reduction.

444 To sum up, we discussed several possible mechanisms that might have led to the PL  
445 peak broadening and focused on the crystalline quality and charged carrier-optical phonon  
446 coupling. By analyzing the temperature-dependent PL FWHM of both strained and strain-free  
447  $\alpha$ -FAPbI<sub>3</sub>, the calculation results demonstrate that the PL broadening with strain is caused by  
448 the strain-induced crystalline quality reduction (major) and enhanced optical phonon  
449 scattering (minor).

450



451

## 452 **Supplementary Discussion 10: Strain Relaxation of the Epitaxial $\alpha$ -FAPbI<sub>3</sub>**

453 Confocal PL spectroscopy is used to study the PL emission with different focal points  
454 inside a 3  $\mu\text{m}$  thick -2.4% strained epitaxial  $\alpha$ -FAPbI<sub>3</sub> (Fig. 2b). Results show a PL redshift  
455 from  $\sim 1.523$  eV to  $\sim 1.479$  eV with the focal point moving from the film surface to the  
456 film/substrate interface. The large discrepancy indicates the strain is relaxed in the thick  
457  $\alpha$ -FAPbI<sub>3</sub> film. Here, we study the possible elastic strain relaxation due to the soft nature of  
458 halide perovskite and the plastic strain relaxation from the strain-induced dislocation.

459

### 460 **1. Elastic strain relaxation**

461 We study the elastic relaxation of the epitaxial  $\alpha$ -FAPbI<sub>3</sub> thin film using finite element  
462 analysis (FEA) simulations. The simulation results are shown in Supplementary Fig. 8 where  
463 an  $\alpha$ -FAPbI<sub>3</sub> thin film with a  $30 \mu\text{m} \times 30 \mu\text{m} \times 3 \mu\text{m}$  dimension in  $l \times w \times t$ . Elastic constants  
464  $C_{11}$ ,  $C_{12}$ , and  $C_{44}$  of  $\alpha$ -FAPbI<sub>3</sub> come from the reported literature<sup>66</sup>. Different biaxial  
465 compressive strains (-1.2% and -2.4%) are applied at the bottom of the  $\alpha$ -FAPbI<sub>3</sub> to simulate  
466 the interfacial strain. Plastic relaxation from the dislocations is ignored in the simulation to  
467 focus on the influence of the elastic relaxation only. Supplementary Fig. 8a, b show the  
468 planar stress distribution from the bottom view of the -1.2% and -2.4% strained  $\alpha$ -FAPbI<sub>3</sub>,  
469 respectively. Supplementary Fig. 8c, d show the vertical stress distribution from the  
470 cross-sectional view of the -1.2% and -2.4% strained  $\alpha$ -FAPbI<sub>3</sub>, respectively.

471 Simulated results indicate a uniform strain distribution throughout the entire epitaxial  
472  $\alpha$ -FAPbI<sub>3</sub> thin film. We further study the thickness-dependent stress distribution along the

473 vertical direction (Supplementary Fig. 8e, f), as labeled by the blue line and the red line in the  
474 Supplementary Fig. 8c, d, respectively. From the results, the strain maintains almost the same  
475 along with the thickness. For a sample thickness of 3  $\mu\text{m}$ , the elastic relaxation is calculated  
476 to be 0.096% and 0.093% for -1.2% and -2.4% strained  $\alpha\text{-FAPbI}_3$ , respectively. The small  
477 discrepancy between the elastic relaxation under the two strain magnitudes is due to the  
478 numerical dispersive error because the FEA simulation uses a dispersive model for  
479 approximation<sup>67</sup>. Therefore, the elastic relaxation in the epitaxially strained  $\alpha\text{-FAPbI}_3$  is not  
480 as prominent as we expected, due to the small thickness (in the range of hundreds of  
481 nanometers to a few micrometers) used in this study. Halide perovskites are in fact still brittle  
482 solids even though they are softer in nature than other conventional semiconductors<sup>68</sup>.

483

## 484 2. Plastic strain relaxation

485 In heteroepitaxial growth, strain usually relaxes plastically rather than elastically. The  
486 calculations of the critical thickness where the dislocations form and relax the strain have  
487 been determined theoretically and experimentally. There are two models that have been  
488 widely used for the critical thickness calculations: the Matthews and Blakeslee (MB) model<sup>69</sup>  
489 and the People and Bean (PB) model<sup>70</sup>.

490 The MB model is a mechanical equilibrium model that stems from the force balance of  
491 dislocations. In this model, the critical thickness is defined as the thickness when the strain  
492 force is equal to the dislocation tension force and can be expressed as:

$$h_c = \frac{b(1 - \nu \cos^2 \alpha)}{8\pi f(1 + \nu) \cos \lambda} \left[ 1 + \ln\left(\frac{h_c}{b}\right) \right]$$

493 where  $h_c$  is the critical thickness,  $b$  is the length of the Burger's vector,  $\nu$  is the Poisson's

494 ratio,  $\alpha$  is the angle between the Burger's vector and the line vector for the dislocation,  $f$  is  
495 the misfit strain, and  $\lambda$  is the angle between the Burger's vector and the line in the interface  
496 plane that is perpendicular to the intersection of the glide plane with the interface.

497 The PB model is an alternative prediction method based on the energy equilibrium that  
498 is widely studied and experimentally proved. In this model, the critical thickness is defined as  
499 the thickness where the strain energy is equal to the dislocation formation energy and can be  
500 expressed as:

$$h_c = \frac{(1 - \nu)b^2}{(1 + \nu)(16\sqrt{2}\pi\alpha f^2)} \ln\left(\frac{h_c}{b}\right)$$

501 where  $a$  is the lattice constant of the material.

502 Many studies show large discrepancy with the MB model. Even the epilayer is thicker  
503 than the MB limit, the dislocations are still absent<sup>71</sup>. Therefore, the MB model underestimates  
504 the critical thickness. The MB model may not give a quantitatively matched result. Besides,  
505  $\alpha$  and  $\lambda$  in PB need to be determined for different dislocations. However, the PB model  
506 gives a closer estimation of the critical thickness<sup>71</sup>, and will therefore be used in this study.

507 We first study the thickness-dependent strain relaxation of the epitaxial  $\alpha$ -FAPbI<sub>3</sub> thin  
508 films with different strains by in-plane XRD. In-plane XRD measures the in-plane lattice  
509 constant of the crystalline materials, which can be directly used to calculate the strain and  
510 contains information about the plastic strain relaxation in heteroepitaxy. Extended Data Fig.  
511 5a, b show the thickness-dependent in-plane XRD patterns of two representative epitaxially  
512 strained  $\alpha$ -FAPbI<sub>3</sub> thin films with -1.2% and -2.4% strain, respectively. The -1.2% strained  
513 epitaxial  $\alpha$ -FAPbI<sub>3</sub> thin film with a thickness of 200 nm shows obvious plastic strain  
514 relaxation (Extended Data Fig. 5a), as evidenced by the peak shifting (to a lower angle, the

515 vertical line labels the fully strained peak position) and broadening. For the -2.4% strained  
516 epitaxial  $\alpha$ -FAPbI<sub>3</sub> thin films, plastic relaxation can be measured in films above 50 nm with  
517 obvious peak shifting and broadening (Extended Data Fig. 5b). The vertical line labels the  
518 fully strained peak position. Besides, we can also obtain the thickness-dependent in-plane  
519 lattice constants, based on which we can calculate the in-plane strain by comparing with the  
520 in-plane lattice constant. The degree of plastic strain relaxation can be quantified by  
521 comparing the local in-plane strain with the highest measured in-plane strain.

522 Quantification of the degree of plastic strain relaxation is done by calculating the  
523 relaxation constant  $R$ :

$$R = \frac{a_{measured} - a_{strained}}{a_{\alpha-FAPbI_3} - a_{strained}}$$

524 where  $a_{measured}$  is the measured in-plane lattice constant at different thicknesses,  $a_{strained}$   
525 is the in-plane lattice constant with maximum strain, and  $a_{\alpha-FAPbI_3}$  is the lattice constant of  
526 the strain-free  $\alpha$ -FAPbI<sub>3</sub>. For the epitaxial film with the same substrate but different  
527 thicknesses,  $R$  ( $0 \leq R \leq 1$ ) reveals the relationship between the film thickness and the  
528 degree of plastic strain relaxation. For  $R$  equals to one, the epitaxial film is considered as  
529 fully-relaxed. Otherwise, the film is considered as partially-relaxed. At relatively low  
530 thickness,  $R$  remains at zero without any relaxation. With increasing thickness,  $R$  will  
531 gradually increase due to the formation of dislocations, which plastically relax their  
532 surrounding strain.

533 The thickness-dependent relaxation constants of each epitaxial  $\alpha$ -FAPbI<sub>3</sub> with different  
534 substrates (i.e., different strains) are calculated and shown in Extended Data Fig. 5c. The  
535 error bars label the range of calculated  $R$  of the films with the same substrate and thickness.

536 Results show that the film with a -2.4% strain quickly relaxes at the thickness of  $\sim 50$  nm  
537 while the film with -0.8% start to relax at  $\sim 200$  nm. Note that the thinnest film we can obtain  
538 is  $\sim 50$  nm and we assume that the thin layer  $\alpha$ -FAPbI<sub>3</sub> will be fully strained without  
539 relaxation. Critical thicknesses are extracted from Extended Data Fig. 5c where  $R$  is larger  
540 than 0 and fitted with both the MB and PB models (Extended Data Fig. 5d). Results show  
541 that the critical thickness decreases with increasing the strain. Our experimental results agree  
542 more with the predicted PB model, indicating that the plastic strain relaxation due to the  
543 dislocations generated during the epitaxial growth is the dominating relaxation mechanism.

544 Confocal PL spectroscopy is used to study the PL emission with different focal points  
545 inside a 3  $\mu$ m thick -2.4% strained epitaxial  $\alpha$ -FAPbI<sub>3</sub> (Fig. 2b). Results show a PL redshift  
546 from  $\sim 1.523$  eV to  $\sim 1.479$  eV with the focal point moving from the film surface to the  
547 film/substrate interface. Besides, we also measured a strain-free bulk  $\alpha$ -FAPbI<sub>3</sub> crystal  
548 sample and a 3  $\mu$ m thick mixed sample (Supplementary Fig. 7). Note that the mixed sample  
549 came from the mixed epitaxial growth with low temperature and low concentration in  
550 Supplementary Fig. 1. By using a low growth temperature and low concentration solution, the  
551 crystallization speed of the epitaxial film will be significantly retarded. The long-time contact  
552 of the substrate and solution will lead to a slow ion exchange between them and, therefore,  
553 form an epitaxial film containing mixed Cl and Br. In the case of Fig. 2a, we adopt an  
554 optimal growth condition with high temperature (180 °C) and high concentration (1.2 mol L<sup>-1</sup>)  
555 to achieve a fast crystallization speed, so that the  $\alpha$ -FAPbI<sub>3</sub> crystals will nucleate on the  
556 substrate, even before the Cl and Br ions dissolve and get mixed in the solution. The obtained  
557 interface will be clear and the epitaxial  $\alpha$ -FAPbI<sub>3</sub> sample will be highly strained. The

558 strain-free sample shows a much less obvious PL peak redshift from  $\sim 1.523$  eV to  $\sim 1.516$  eV  
559 (Supplementary Fig. 7a), which can be attributed to reabsorption as discussed above. For the  
560 mixed sample grown under low temperature and low concentration (Supplementary Fig. 7b),  
561 the PL peak at the sample surface is at  $\sim 1.542$  eV, indicating incorporation of Cl and Br  
562 elements from the substrate. With increasing focal depth to the film/substrate interface, the  
563 PL peak blueshifts to below 1.550 eV, which indicates a higher degree of mixing.

564 Film thickness-dependent PL measurements are based on samples at -2.4% strain with  
565 different epitaxial film thicknesses (Supplementary Fig. 9). A 633-nm laser with the standard  
566 mode is used as the excitation source to study the overall emission behavior of the film at all  
567 depths. The PL peak position shows a strong film thickness dependency. When the  $\alpha$ -FAPbI<sub>3</sub>  
568 film thickness increases, the PL emission peak shifted from  $\sim 1.479$  eV back to 1.523 eV, the  
569 same as that of the strain-free  $\alpha$ -FAPbI<sub>3</sub>, which indicates the strain has been fully relaxed.

570

571

## 572 **Supplementary Discussion 11: Temperature-Dependent Bandgap of the Strained** 573 **$\alpha$ -FAPbI<sub>3</sub>**

574 Due to the soft nature, external stimuli (i.e., temperature, pressure) can effectively alter  
575 the lattice structure of halide perovskites, and, therefore, change the electronic band  
576 structures<sup>18,20,72</sup>. Under such considerations, temperature-dependent PL was studied on both  
577 epitaxial  $\alpha$ -FAPbI<sub>3</sub> and free-standing  $\alpha$ -FAPbI<sub>3</sub>. Epitaxially grown thin films are subjected to  
578 the lattice deformation of the substrates due to the strong chemical bonds at the interface and  
579 the much bulkier size of the substrate. In this case, the epitaxial film will adopt a similar

580 thermal expansion coefficient  $\alpha_t$  to that of the substrate<sup>73</sup>. A reported study has shown that  
581 the  $\alpha_t$  of halide perovskites are subjected to the molecular radius of halides. Therefore, the  
582 I-based perovskite epitaxial layer will have a larger  $\alpha_t$  due to the large radius of I<sup>-</sup> than the Br<sup>-</sup>  
583 and Cl<sup>-</sup> based halide perovskite substrate<sup>74</sup>. The epitaxial  $\alpha$ -FAPbI<sub>3</sub> on a Br<sup>-</sup> and Cl<sup>-</sup> based  
584 substrate exhibited a reduced temperature dependency compared with the freestanding  
585  $\alpha$ -FAPbI<sub>3</sub>. Additionally, if the substrate has a larger  $\alpha_t$  than that of the strained layer, we  
586 should expect to see the strained sample has a stronger temperature dependence than that of  
587 the free-standing sample.

588

589

### 590 **Supplementary Discussion 12: Band Structure of the Strained $\alpha$ -FAPbI<sub>3</sub>**

591 UPS measurements are carried out on epitaxial  $\alpha$ -FAPbI<sub>3</sub> films with different strain  
592 levels. Extended Data Fig. 6a shows the cutoff energy region and Extended Data Fig. 6b  
593 shows the valence band region of the  $\alpha$ -FAPbI<sub>3</sub>. Take the UPS spectrum of the strain-free  
594  $\alpha$ -FAPbI<sub>3</sub> as an example, the position of the electron affinity (Fermi level) *versus* vacuum is  
595 the difference between the high binding energy cutoff and the radiation energy of He I (21.22  
596 eV):

$$597 \quad 16.09 \text{ eV} - 21.22 \text{ eV} = -5.13 \text{ eV}$$

598 The low binding energy cutoff (0.62 eV) determines the position of Valence Band  
599 Maximum (VBM). Therefore, the position of the VBM relative to the vacuum level is:

$$600 \quad -5.13 \text{ eV} - 0.62 \text{ eV} = -5.75 \text{ eV}$$

601 Considering the measured optical bandgap of  $\sim 1.51$  eV (Fig. 2a), the Conduction Band

602 Minimum (CBM) is determined to be -4.24 eV. This also suggests that the Fermi level is  
603 closer to the VBM than to the CBM, and therefore the strain-free  $\alpha$ -FAPbI<sub>3</sub> is p-type.  
604 Similarly, all other strained epitaxial thin films show a p-type character.

605 Additionally, the results show that the valence band is pushed up by 50 meV while the  
606 CBM is only pushed up by 15 meV when strain increases from 0% to -2.4%. The reason why  
607 VBM is pushed up more than the CBM by the biaxial in-plane compressive strain is because  
608 the compressed PbI<sub>6</sub> octahedron contributes more to the VBM than the CBM. The VBM is  
609 composed of the coupled Pb 6s and I 5p orbitals that form the PbI<sub>6</sub> octahedral, while the  
610 CBM is mostly nonbonding localized states of Pb p orbitals<sup>75</sup>.

611

612

### 613 **Supplementary Discussion 13: Effective Mass Calculations and Carrier Mobility** 614 **Characterizations of the Strained $\alpha$ -FAPbI<sub>3</sub>**

#### 615 **1. Effective mass calculations**

616 To investigate the effect of strain on carrier dynamics in  $\alpha$ -FAPbI<sub>3</sub>, we analyzed the  
617 variation of charged carrier mobility via predicting effective masses of charged carriers from  
618 first-principles calculations. In the calculations, the mean free time of carriers was assumed to  
619 be a constant, and the reversely proportional relationship between the effective mass and  
620 charged carrier mobility was used. Carrier effective masses are determined by the curvature  
621 of the highest energy at the VBM for holes and lowest energy at the CBM for electrons in the  
622  $k$  space. Figure 3a shows the calculated electron and hole effective masses of  $\alpha$ -FAPbI<sub>3</sub> under  
623 different strain levels. Electronic band structures of  $\alpha$ -FAPbI<sub>3</sub> under 3%, 0%, and -3% are



624 also shown in the lower panels of Fig. 3a. Results indicate that the hole effective mass  $m_h^*$   
625 decreases when strain goes from tensile to compressive, while the electron effective mass  $m_e^*$   
626 barely changes with the strain. The trend of  $m_h^*$  can be revealed from the curvature of the  
627 highest energy point of the VBM, which gets less dispersive with increasing compressive  
628 strain. This is due to the fact that the VBM that determines  $m_h^*$  mainly consists of Pb 6s and I  
629 5p orbitals. Under tensile strain, the distance between Pb and I atoms increase and therefore  
630 the Pb-I bond interaction is weakened, thus leading to the increase of effective mass. In  
631 contrast, the hole mobility will increase under compressive strain due to the enhanced Pb-I  
632 bond interaction and the decreased effective mass. However, the CBM that determines the  
633 electron effective mass mainly consist of Pb p orbitals is less sensitive to the deformation of  
634 Pb-I bonds, which is why  $m_e^*$  barely changes with applied strain<sup>15</sup>.

635

## 636 **2. Interfacial carrier transfer and Hall effect measurements**

637 Hall effect is used to measure the strain-dependent carrier mobility of the epitaxial  
638  $\alpha$ -FAPbI<sub>3</sub> thin films. Before the measurement, we study the possible carrier collection from  
639 the substrates since the substrates are halide perovskites with high carrier mobility as well.  
640 We first analyze the device structure with the FEA simulation. The schematic device  
641 structure is shown in Supplementary Fig. 10a where four Au electrodes are deposited with a  
642 layer of Parylene-C beneath. The Parylene-C serves as the insulating layer to prevent the  
643 carrier collection from the substrate to the electrodes. To better understand the carrier transfer  
644 between the epitaxial layer and the substrate, we also study the band alignment between them  
645 (Supplementary Fig. 10b). Herein,  $\alpha$ -FAPbI<sub>3</sub> and MAPbBr<sub>3</sub> are analyzed as an example.

646  $\alpha$ -FAPbI<sub>3</sub> has a very different band structure compared with MAPbBr<sub>3</sub> in terms of bandgap,  
647 valance band maximum (VBM) as well as conduction band minimum (CBM). For  $\alpha$ -FAPbI<sub>3</sub>,  
648 VBM and CBM are determined to be -5.75 eV and -4.25 eV by the ultraviolet photoelectron  
649 spectroscopy, respectively. For MAPbBr<sub>3</sub>, VBM and CBM are determined to be -6.20 eV and  
650 -3.90 eV from the literature<sup>76</sup>. For the Hall measurement, the injected carriers are subject to  
651 the Lorentz force applied by the vertical magnetic field and are accumulated at the diagonal  
652 electrodes to build up the Hall voltage. However, the large energy barrier at the  
653 heterojunction interface blocks the carrier injection from the  $\alpha$ -FAPbI<sub>3</sub> to the MAPbBr<sub>3</sub>.  
654 Therefore, there is a very low concentration of free carriers in the substrate that can hardly  
655 generate a significant Hall voltage during the measurement. This analysis also applies to  
656 other substrates MAPbCl<sub>x</sub>Br<sub>3-x</sub> in this study with different compositions from MAPbBr<sub>3</sub>.  
657 When incorporating more Cl into the MAPbBr<sub>3</sub> substrate, the bandgap will further increase  
658 by lifting up the CBM and pushing down the VBM, and the energy barrier between the  
659  $\alpha$ -FAPbI<sub>3</sub> and the substrates will be even larger<sup>59</sup>. Thus, interfacial charge transport will be  
660 even less favorable. Additionally, we also exclude the free carrier transfer from the MAPbBr<sub>3</sub>  
661 to the  $\alpha$ -FAPbI<sub>3</sub>.

662 We then simulate the current distribution within the device by FEA. We also intend to  
663 quantify the current density in both the epitaxial layer and the substrate to study the  
664 contribution of the substrate to the Hall measurement. With the combined energy diagram  
665 and the electric field distribution, we simulate the current distribution in the device  
666 (Supplementary Fig. 10c upper panel). The simulation results show that the current  
667 distribution is completely different from the electric field distribution. Current density in the

668 epitaxial layer ( $9.8 \text{ A m}^{-2}$ ) is much higher than that of the substrate ( $0.4 \text{ A m}^{-2}$ ), which means  
669 that the large energy barrier between the epitaxial layer and the substrate, as well as the  
670 minimal vertical electric field distribution and the insulation of the Parylene-C, minimizes the  
671 carrier injection to the substrate. A closer look at the area that is close to the electrode  
672 suggests that the carrier injection to the substrate is indeed prohibited (Supplementary Fig.  
673 10c lower panel, red arrows indicate the direction of the current flow). To quantify the ratio  
674 of the current in the substrate to that in the epitaxial layer, we study the current density along  
675 the vertical orange line where the current flows horizontally (at a steady state).  
676 Supplementary Fig. 10d shows the vertical current density distribution along the vertical  
677 orange line where the heterostructural interface locates at 500 nm from the bottom (0 nm).  
678 The ratio of current density across the interface is shown to  $\sim 24.5:1$  where the epitaxial layer  
679 is  $9.8 \text{ A m}^{-2}$  and the substrate is  $0.4 \text{ A m}^{-2}$ . By integrating the area below the current  
680 distribution curve, we obtain the ratio of the current density in the substrate to the total  
681 current density along the vertical line to be 0.8%. Therefore, we conclude that the carrier in  
682 the substrate is negligible compared with that in the epitaxial layer, and we attribute this  
683 result to the large energy barrier between the epitaxial layer and the substrate, as well as the  
684 minimal vertical electrical field distribution and the insulation of the Parylene-C layer.

685 Without the concern of possible carrier collection from the substrates, we perform Hall  
686 effect measurement to the epitaxial  $\alpha\text{-FAPbI}_3$  thin films under different strains. Measurement  
687 results also show p-type character, which is consistent with the UPS results. The hole  
688 mobility as a function of strain is plotted in Fig. 3b, which doesn't show a linear tendency  
689 with increasing strain. Devices with -0.8%, -1.2%, and -1.4% strain show enhanced hole

690 mobility compared with that of the strain-free  $\alpha$ -FAPbI<sub>3</sub> bulk crystal. A -1.2% strained device  
691 gives the highest mobility of  $\sim 72 \text{ cm}^2 \text{ V}^{-1} \text{ s}^{-1}$ . Further increasing the strain results in a drastic  
692 drop in the hole mobility, because higher strain levels will relax at a lower thickness and  
693 induce high concentrations of dislocations that deteriorate the device performance.

694

### 695 **3. Time-of-flight (ToF) measurements**

696 To validate the results from the Hall effect measurement, we study the carrier mobility  
697 of the epitaxial  $\alpha$ -FAPbI<sub>3</sub> thin films under different strains by ToF measurements. The  
698 schematic device structure is shown in the inset of Fig. 3d. A layer of Parylene-C was  
699 deposited between the Au electrode and the substrate to block the carrier extracted from the  
700 substrate as demonstrated above. Besides, we adopted a 685-nm laser as the excitation source  
701 so that the photon can only be absorbed by the epitaxial layer rather than the substrate that  
702 has a larger bandgap than the excitation laser energy. In this case, we guaranteed the  
703 measured photovoltages coming from the epitaxial layer absorption were the same. Similarly,  
704 the excited electrons that occupy the CBM of the  $\alpha$ -FAPbI<sub>3</sub> are less likely to be extracted to  
705 the CBM of the substrate due to the large energy barrier, as shown in Supplementary Fig. 10.

706 ToF measurements were carried out with the designed structure where the distance  
707 between the two electrodes is controlled to be 100  $\mu\text{m}$  in lateral directions. Meanwhile, the  
708 thickness of the epitaxial layer is controlled to be the same and all the devices are biased with  
709 1 V. The measured transient photocurrents are shown in Fig. 3c where the carrier transit time  
710 can be extracted as the inflection point of the photocurrent curve. The carrier mobility can be  
711 calculated by:

$$\mu = \frac{d^2}{Vt}$$

712 where  $\mu$  is the calculated carrier mobility,  $d$  is the thickness of the target region,  $V$  is the  
713 applied voltage, and  $t$  is the measured carrier transit time. The measured carrier mobilities  
714 are plotted in Fig. 3d. Our measured ToF mobility of the epitaxial  $\alpha$ -FAPbI<sub>3</sub> with different  
715 strains showed a similar trend compared with the measured Hall mobility. -1.2% strained  
716  $\alpha$ -FAPbI<sub>3</sub> exhibits the highest carrier mobility while further increasing the strain can lead to  
717 faster relaxation, and the accumulation of dislocations will reduce the carrier mobility.

718 Besides, bias and laser power dependence of the ToF measurement are also discussed.  
719 ToF mobility is calculated by  $\mu = \frac{d^2}{vt}$ . The applied bias will only change the carrier transient  
720 time rather than the carrier mobility. This is because the carrier mobility is an intrinsic  
721 property of the semiconductor materials and is independent of the magnitude of the applied  
722 bias. This rule has been demonstrated by many ToF measurements of halide perovskites, in  
723 which the carrier mobility is independent of the applied bias but the measured carrier  
724 transient time is inversely proportional to the applied bias<sup>77,78</sup>. In the measurements, as  
725 described in the manuscript, all experiments are tested under 1 V DC bias with other  
726 experimental parameters well-controlled. Therefore, the transient photocurrents of the  
727 epitaxial films under different strain magnitudes appropriately reveal the carrier mobility of  
728 the epitaxial thin films. For the ToF measurement, it has been reported that the  
729 photogenerated carrier density shows laser power dependency and a high carrier density can  
730 generate the space charge effect which affects carrier extraction<sup>79,80</sup>. However, the space  
731 charge effect will be significant only in systems where the ratio between the electron mobility  
732 and the hole mobility exceeds two orders of magnitude<sup>81</sup>. According to the reported carrier

733 mobility of halide perovskites, the electron and hole mobilities are usually on the same order  
734 of magnitude when they are from the same literature<sup>82</sup>. Therefore, the space charge effect can  
735 be safely ignored and the laser power dependence of ToF measurements is less significant in  
736 this study. In the measurements, the laser intensity is kept at constant ( $10 \text{ mW cm}^{-2}$ )  
737 throughout the entire measurement so that the only variation is the strain magnitude of the  
738 epitaxial thin film.

739         The possible influence of the current–voltage ( $I$ – $V$ ) hysteresis on the ToF measurement  
740 is also discussed here. During the ToF measurement, the devices are biased under a constant  
741 voltage, e.g., 1 V, to collect photogenerated carriers in the epitaxial thin films. In this case,  
742 the baseline current due to ion migration and mobile electron and hole carriers under a fixed  
743 electric field is considered to be in a steady state. Adding on top of the baseline current, a  
744 pulsed laser is used as the excitation source to generate carriers in the epitaxial thin film. The  
745 corresponding photocurrent-time characteristics are recorded by an oscilloscope. The  
746 timescale of the excited transient current, i.e., ToF, is measured to be  $\sim 10^{-6}$  s (as seen in Fig.  
747 3 in the main text).  $I$ – $V$  hysteresis is reported to originate from ion migration, device  
748 capacitive charging, and perovskite ferroelectric polarization<sup>83,84</sup>. For the ion migration, the  
749 timescale is reported to be in the range of seconds to minutes in halide perovskites<sup>85</sup>, which is  
750 much longer than that of the ToF. For the device capacitive charging, whose timescale is  
751 reported to be in the range of milliseconds to seconds<sup>83</sup>, which is also much longer than that  
752 of the ToF. Also, the timescale of ferroelectric dipole switching is reported to be faster than  
753  $10^{-8}$  s<sup>86</sup>, which is much shorter than that of the ToF. Besides, since the devices are biased  
754 under 1 V DC voltage during the measurement, the capacitive charge and the ferroelectric

755 dipoles are almost kept constant in the devices. Therefore, it is safe to exclude the possible  
756 influence of the  $I$ - $V$  hysteresis on the ToF measurement.

757

#### 758 **4. Analysis of the influence of ion migrations to the carrier mobility measurements**

759 Ion migrations of halide perovskites have been studied in the literature and are believed  
760 to be the origin of the reported current-voltage hysteresis in halide perovskites. Reported  
761 studies showed that the mobility of the vacancies and the ions in polycrystalline perovskites  
762 were determined to be  $\sim 1.6 \times 10^{-6} \text{ cm}^2 \text{ V}^{-1} \text{ s}^{-1}$  and  $\sim 5 \times 10^{-8} \text{ cm}^2 \text{ V}^{-1} \text{ s}^{-1}$ , respectively<sup>87,88</sup>.  
763 However, these values are much smaller than that of the measured hole mobilities ( $\sim 50 \text{ cm}^2$   
764  $\text{V}^{-1} \text{ s}^{-1}$ ) in this study. Additionally, the carrier transit time in the ToF measurement of this  
765 study was in the range of  $\mu\text{s}$ , which was too short for the ions to move a substantial distance.  
766 Therefore, it is safe to exclude the contribution of ions and structural vacancies from the  
767 measured hole mobility in this study.

768 Besides, grain boundaries of the polycrystalline halide perovskites were reported to be a  
769 major pathway for ion migrations<sup>89-91</sup>. In this study, the epitaxial growth of single-crystalline  
770 perovskites minimizes the formation of grain boundaries and, therefore, minimizes the  
771 influence of the ion migrations. In a reported study, the ion migration mobility in both  
772 polycrystalline and single crystalline methylammonium lead iodide ( $\text{MAPbI}_3$ ) were  
773 measured<sup>92</sup>. Compared with the ion migration in polycrystalline  $\text{MAPbI}_3$  whose ion migration  
774 mobility was  $\sim 1 \times 10^{-9} \text{ cm}^2 \text{ V}^{-1} \text{ s}^{-1}$ , the ion migration in single crystalline  $\text{MAPbI}_3$  can hardly be  
775 detected<sup>92</sup>. Therefore, we can conclude that the influence of ionic movements in the halide  
776 perovskites can be excluded from this study.

777

## 778 **5. Crystalline quality characterization**

779 The space-charge limit current (SCLC) method is used to quantitatively evaluate the  
780 crystalline quality of the epitaxial thin film (Extended Data Fig. 7 and Supplementary Fig.  
781 11). Devices adopt the same structure as the one used in ToF measurement. Devices with  
782 different strain levels (strain-free, -0.8%, -1.4%, and -2.4%) are fabricated and tested. Note  
783 that bulk  $\alpha$ -FAPbI<sub>3</sub> single crystals were used as the substrates to fabricate strain-free devices.

784 We first study the  $I$ - $V$  characteristic curves of the devices with forward and reverse  
785 scans from 0.01 V to 2 V (Extended Data Fig. 7a to 7d). Note that the devices adopt a planar  
786 structure to correlate with the devices used in the Hall effect measurements. A layer of  
787 Parylene-C (50 nm) and a layer of Au (50 nm) are sequentially deposited on the substrates  
788 while the lateral distance between two Parylene-C/Au electrodes is 100  $\mu$ m. Epitaxially  
789 strained  $\alpha$ -FAPbI<sub>3</sub> thin films are then grown from the gaps between the electrodes and cover  
790 part of the electrodes for electrical contact.

791 In the forward scan, the log-log  $I$ - $V$  characteristic curves show different regions of  
792 behavior. At low voltages, the  $I$ - $V$  curves exhibit a typical ohmic conduction behavior, where  
793 the current is linearly related to the applied voltage ( $n \sim 1$ , blue line). In this region, the  
794 quantity of the thermally generated free carriers exceeds that of the externally injected  
795 carriers<sup>93</sup>. With increasing the applied voltage, the externally injected carriers gradually  
796 increase and start to fill the traps. Therefore, a trap-filling process is identified by the end of  
797 the linear ohmic region ( $n > 3$ , green). By further increasing the voltage, traps in the bandgap  
798 are completely filled by the externally injected carriers and the carriers move freely<sup>94</sup>. In this



799 region, the current is squarely related to the applied voltage ( $n \sim 2$ , orange).  $V_{TFL}$  is extracted  
800 by finding the voltage where the ohmic region ends. The extracted  $V_{TFL}$  in samples with  
801 different strains is used to evaluate the trap density, which agrees with the results in the  
802 manuscript.

803 The forward scan is followed by a reverse scan where the  $I$ - $V$  characteristic curves of  
804 the reverse scan show only a linear region. By fitting the  $I$ - $V$  curves of the reverse scan, we  
805 find out that the current is squarely related to the applied voltage ( $n \sim 2$ , red). During the  
806 reverse scan, the filled traps will not undergo a de-trapping process because of the existence  
807 of the applied electric field as well as the continuously injected carriers. Therefore, the  
808 reverse scan cannot be used to study the trap-filling process, and the evaluation of the  $V_{TFL}$   
809 can only be studied with the forward scan. Trap density of the epitaxial film  $n_t$  can be  
810 calculated by:

$$V_{TFL} = \frac{en_t d^2}{2\epsilon\epsilon_0}$$

811 where  $d$  is the layer thickness,  $\epsilon$  ( $\approx 47$ ) is the relative dielectric constant of  $\alpha$ -FAPbI<sub>3</sub>, and  
812  $\epsilon_0$  is the vacuum permittivity.

813 We also statistically study the trap density in the epitaxial  $\alpha$ -FAPbI<sub>3</sub> film with different  
814 strain magnitudes to evaluate the robustness of the measured trap density values. Here, five  
815 different devices of each strain value are tested. The trap density of the epitaxial  $\alpha$ -FAPbI<sub>3</sub>  
816 film from different samples are calculated and displayed in Supplementary Fig. 11a. The  
817 average trap densities and the standard deviation are shown in Supplementary Fig. 11b. With  
818 increasing the strain, the average trap densities show an increasing trend, indicating that a  
819 higher strain level induces a higher defect density in the epitaxial  $\alpha$ -FAPbI<sub>3</sub> film. This trend

820 correlates well with the data we showed in the manuscript. Meanwhile, the standard deviation  
821 of the trap density also increases with the strain, which reveals an increased disorder in the  
822 epitaxial  $\alpha$ -FAPbI<sub>3</sub> film at higher strain values.

823 Besides, we also investigate  $I$ - $V$  characteristic curves from the same device under  
824 different measurement conditions, e.g., different scan rates and scan directions.  $I$ - $V$  curves of  
825 the halide perovskites are reported to be scan rate-dependent due to the fact that the scan rate  
826 can alter the charged carrier collection efficiency of the devices, which results in artificial  $I$ - $V$   
827 curves<sup>84,85,95</sup>. However, this discrepancy can be effectively minimized by adopting a  
828 relatively slow scan rate<sup>83</sup> since a fast scan rate has been reported to go beyond the response  
829 speed of free carriers to the electric field<sup>96</sup>. To prove that the 50 mV s<sup>-1</sup> scan rate we use in  
830 this work does not produce artificial  $I$ - $V$  curves, we study  $I$ - $V$  curves under four representative  
831 scan rates (Supplementary Fig. 11c).  $I$ - $V$  curves with 10 mV s<sup>-1</sup>, 50 mV s<sup>-1</sup>, and 200 mV s<sup>-1</sup>  
832 scan rates show distinct trap filling behavior as we discussed above. The  $V_{TFL}$  extracted from  
833 the  $I$ - $V$  curves with 10 mV s<sup>-1</sup> and 50 mV s<sup>-1</sup> scan rates are similar, indicating that 10 mV s<sup>-1</sup>  
834 and 50 mV s<sup>-1</sup> are sufficiently slow to avoid artificial  $I$ - $V$  curves and  $V_{TFL}$  values. Meanwhile,  
835 increasing the scan rate to 200 mV s<sup>-1</sup> leads to a smaller  $V_{TFL}$  because of the limited response  
836 of free carriers to the rapid electric field change. No trap filling process can even be measured  
837 when further increasing the scan rate to 1000 mV s<sup>-1</sup>, showing that the  $I$ - $V$  curve under a very  
838 fast scan rate can skew the results. Therefore, we can conclude that the 50 mV s<sup>-1</sup> scan rate  
839 we use in the SCLC measurements helps produce reliable  $I$ - $V$  curves and  $V_{TFL}$ . Besides, we  
840 study how the scan direction may possibly affect the SCLC measurement. Supplementary Fig.  
841 11d shows  $I$ - $V$  curves of the same device with different scan directions. The  $I$ - $V$  curves from

842 positive and negative scan directions, with  $\sim 10$  min in between the scans, are similar to each  
843 other, which is because the device adopts a symmetric Au/perovskite/Au structure. The initial  
844 direction of the forward scan along either direction should give the same result. Therefore, we  
845 can conclude that the SCLC measurements under different scan conditions, with a slow scan  
846 rate ( $50 \text{ mV s}^{-1}$ ), and a symmetric device structure can produce reliable results.

847 In this study, the goal is not to distinguish the origins or the densities of various traps  
848 but is to study the trap density increment in the epitaxial  $\alpha$ -FAPbI<sub>3</sub> thin films when the strain  
849 magnitude is increased. For lattice-mismatched heteroepitaxial growth, the density of misfit  
850 dislocations will be increased with increasing the interfacial misfit magnitude and the  
851 epitaxial layer thickness, to partially release the strain<sup>97</sup>. These misfit dislocations tend to  
852 degrade the properties of the epitaxial layers and, therefore, the performance of the devices  
853 by introducing below-gap trap states. For the impurity, the growth precursor was controlled  
854 to be the same, which will keep a similar impurity source for all  $\alpha$ -FAPbI<sub>3</sub> films in this study.  
855 Without additional impurity source being introduced during epitaxial growth, the epitaxial  
856 film with different strain levels should share a similar impurity density. Therefore, we  
857 exclude the contribution of impurities to the measured trap density increment. For the other  
858 crystallographic defects (e.g., vacancies, interstitials, antisites, etc.), their contributions to the  
859 trap density increment are considered to be minor, because it is a convention that the  
860 generation of dislocations is the main reason for strain relaxation in heteroepitaxy<sup>97,98</sup>. For the  
861 interfacial defects formed at the perovskite/electrode interface, all devices fabrication adopted  
862 the same protocol. Therefore, the interfacial traps caused by the interfacial defects are similar  
863 for different strain values and can be excluded from the possible reason for the trap density

864 increment in the epitaxial samples. In this case, the impurities and the interfacial defects will  
865 not lead to the significant trap density increment, up to ~1000% as observed in the studies  
866 with increasing the strain magnitude from 0% to -2.4%.

867       Based on the above discussions, we demonstrate that the trap density increments with  
868 increasing the interfacial misfit magnitude and film thickness can be attributed to the  
869 strain-induced dislocations. Even though there is currently a lack of an experimental  
870 characterization technique that would allow accurately quantifying the separate contribution  
871 of each defect due to the complexity of these defects<sup>99</sup>, contributions from all other types of  
872 traps are minor and can be safely excluded in this study by adopting the unique variable  
873 principle throughout the experiment. Actually, the unique variable principal is commonly  
874 used to exclude irrelevant factors in trap density measurements, as evidenced by many  
875 examples in the literature. Vapor deposition of relatively thick perovskite film is reported to  
876 show reduced trap density due to the reduced crystallographic defects. The trap density  
877 increment in the relatively thinner sample excludes the contribution of impurities and the  
878 interfacial defects because they are considered to be similar to those of the thicker sample and  
879 will not lead to trap density reduction<sup>100</sup>. Also, it is recently reported that the addition of  
880 CuBr into inorganic perovskite will reduce the trap density. The influence of the interfacial  
881 defects and the impurities are considered of minor influence to the trap density reduction in  
882 the control sample due to the same fabrication protocol<sup>101</sup>. Similarly, the addition of  
883  $\text{Eu}^{3+}$ - $\text{Eu}^{2+}$  ionic pair can reduce the crystallographic defects generated by the  $\text{Pb}^0$  and  $\text{I}^0$ . The  
884 trap density increment in the control sample rules out the contribution of interfacial defects  
885 and impurities because the samples share similar fabrication processes<sup>102</sup>. Additionally,

886 perovskite seeding growth is reported to improve the crystallinity and reduce the trap density.  
887 The interfacial defects and the impurities in the control sample are considered to be similar in  
888 the seeded grown sample and control sample<sup>103</sup>. What's more, modifying the interface  
889 between the perovskite and the electron transporting layer is shown to reduce interfacial  
890 defects and trap density. The influence of the impurities and crystallographic defects can be  
891 excluded because they are considered to be similar in different devices<sup>104</sup>. Finally,  
892 incorporating bilateral alkylamine additives is shown to reduce interfacial defects and trap  
893 density in the perovskite film. Contributions from impurities and crystallographic defects are  
894 ruled out due to the fact these two factors are similar in different devices<sup>105</sup>.

895 We also investigate the literature to study the minimum trap density difference that can  
896 be measured by the SCLC method. Researchers demonstrated the reduced trap density by 15%  
897 due to the incorporation of Cl in the perovskite film<sup>100</sup>. In two-dimensional perovskite  
898 nanowires with different layer numbers, a one-fold increment of trap density was also  
899 reported<sup>106</sup>. Meanwhile, researchers demonstrated the decrease of trap density by ~20% with  
900 a modified tin doped indium oxide (ITO) surface<sup>107</sup>. Similarly, a decrease of trap density by  
901 ~50% with a modified interface was also reported<sup>108</sup>. Compared with the reported works, the  
902 results in this study demonstrate a difference from ~30% to up to ~1000%, which is  
903 sufficiently large to conclude that a higher strain can induce more defects.

904 Characterizing the trap density in halide perovskite thin films has been widely studied.  
905 Quantitative characterization of the trap density in halide perovskites are mostly done by the  
906 SCLC method (the dark  $I-V$  characteristic curve). It is believed to be the most facile, accurate,  
907 and direct technique for trap density characterization and has been extensively used<sup>77,78,109</sup>.

908 Besides the SCLC method, tuning the excitation density of input photons in the transient  
909 photocurrent measurement is also reported to roughly estimate the trap density by generating  
910 different densities of free carriers and monitoring the decay rate<sup>110,111</sup>. The measurement  
911 accuracy is relatively low. Additionally, capacitance-frequency ( $C-\omega$ ) spectroscopy has been  
912 reported to study the trap density in organic materials<sup>112,113</sup> and halide perovskites<sup>114-117</sup>. The  
913 low-frequency capacitance originates from the carrier trapping/detrapping of electronic traps  
914 while the high-frequency capacitance is attributed to the geometrical capacitance and the  
915 depletion capacitance<sup>114,116</sup>.

916 In this study, we use the  $C-\omega$  spectroscopy as an alternative probe for trap density of  
917 epitaxial  $\alpha$ -FAPbI<sub>3</sub> thin films with different strain magnitudes. Devices for  $C-\omega$   
918 measurements have a lateral configuration with a 3 mm width. Au and ITO are used as the  
919 two electrodes with a  $2 \times 2$  mm<sup>2</sup> area. During the measurement, a 0.5 V AC voltage is applied.  
920 The resulting electric field is  $1.67 \times 10^{-4}$  V  $\mu\text{m}^{-1}$ , which is insufficient for generating ion  
921 migration<sup>117</sup>. In this case, we exclude the contribution of charged ions to the measured  
922 capacitance. The capacitance of  $\alpha$ -FAPbI<sub>3</sub> thin films with different strain magnitudes are  
923 measured in the frequency range of  $1 \sim 10^5$  Hz in dark. To eliminate the influence of the  
924 parasitic capacitance from the substrate and air, we first measure the  $C-\omega$  spectra of the bare  
925 substrate without the epitaxial layer. After measuring the  $C-\omega$  spectra of the devices with the  
926 epitaxial layer, we subtract the spectra of the substrates from that of the devices to obtain the  
927  $C-\omega$  spectra of the epitaxial layer, which therefore exclude the capacitance contributions from  
928 the substrates and air. The results after subtraction are shown in Supplementary Fig. 12a. The  
929 measured capacitance gradually increases with increasing the strain magnitudes, indicating

930 the accumulation of electronic traps. We then calculate the trap density with the  $C-\omega$   
 931 measurement results. The trap density can be calculated by

$$N_t(E_\omega) = -\frac{V_b}{qkAtT} \frac{dC(\omega)}{d \ln(\omega)}$$

932 where  $N_t$  is the trap density at a certain trap energy  $E_\omega$ ,  $V_b$  is the build-in potential and is  
 933 estimated to be  $\sim 0.5$  V from the work function difference between Au and ITO,  $q$  is the  
 934 element charge,  $k$  is the Boltzmann constant,  $A$  is the device area,  $t$  is the thickness, and  
 935  $T$  is the temperature. Trap energy  $E_\omega$  is calculated by

$$E_\omega = kT \ln\left(\frac{\omega_0}{\omega}\right)$$

936 where  $\omega_0$  is the attempt-to-escape frequency, which is reported to be  $\sim 2 \times 10^{11} \text{ s}^{-1}$  for halide  
 937 perovskites<sup>118</sup>. The calculated trap density of the epitaxial  $\alpha$ -FAPbI<sub>3</sub> thin films with different  
 938 strain magnitudes are shown in Supplementary Fig. 12b and an obvious trap density  
 939 increment can be seen with increasing strain magnitudes.

940 To quantitatively evaluate the trap density in the epitaxial thin films, we fit the calculated  
 941 trap density distribution with the following Gaussian distribution equation:

$$N_t(E_\omega) = \frac{n_t}{\sigma\sqrt{2\pi}} \exp\left[-\frac{(E_0 - E_\omega)^2}{2\sigma^2}\right]$$

942 where  $n_t$  is the trap density,  $\sigma$  is the disorder parameter, and  $E_0$  is the mean energy of the  
 943 traps. The fitted trap density ( $n_t$ ) for 0%, -0.8%, -1.4%, and -2.4% strained epitaxial thin  
 944 films are  $2.6 \times 10^{11} \text{ cm}^{-3}$ ,  $3.2 \times 10^{11} \text{ cm}^{-3}$ ,  $7.2 \times 10^{11} \text{ cm}^{-3}$ , and  $2.4 \times 10^{12} \text{ cm}^{-3}$ , respectively. The  
 945 trap density increment with increasing the strain magnitude indicates an accumulation of  
 946 dislocations under a higher strain magnitude<sup>97</sup>. The trend also agrees with that measured by  
 947 the SCLC method (Extended Data Fig. 7 and Supplementary Fig. 11). Note that the  $C-\omega$   
 948 method measures the sum of electron and hole traps<sup>112</sup> while the SCLC methods can

949 distinguish electron and hole traps with selected electrodes<sup>78</sup>. In the SCLC measurements, we  
950 adopt an Au/perovskite/Au structure that only reveals the hole traps due to the energy  
951 alignment of the Au electrode for hole injection<sup>78</sup>. This may be the main reason that leads to  
952 the small discrepancy in the results measured by the  $C-\omega$  and the SCLC methods.

953

954

## 955 **Supplementary Discussion 14: Different Methods for Stabilizing $\alpha$ -FAPbI<sub>3</sub>**

### 956 **1. Current methods**

957 The high-temperature  $\alpha$ -FAPbI<sub>3</sub> phase suffers from a spontaneous and quick phase  
958 transition to the low-temperature, photoinactive  $\delta$ -FAPbI<sub>3</sub> phase at room temperature. The  
959 most popular stabilization method for  $\alpha$ -FAPbI<sub>3</sub> is accomplished by mixing/doping small  
960 ions<sup>119-121</sup>. Several reported works discussed the possible stabilization mechanisms behind.  
961 Researchers explained the stabilization effect of mixing small ions by studying the entropy  
962 where the formation energy of the mixed  $\delta$  phase was too large for the phase transition to  
963 take place<sup>119</sup>. Meanwhile, the internal strain of  $\alpha$ -FAPbI<sub>3</sub> lattice was reported as the driving  
964 force of the phase transition and compensation of the strain by incorporating small ions could  
965 prevent the phase transition<sup>10</sup>. Despite the success and reliability of this method, it should be  
966 pointed out that the incorporation of the small ions usually leads to an enlarged bandgap<sup>119</sup>.  
967 As a result, light absorption at the long-wavelength region will be inhibited and the  
968 short-circuit current of the fabricated solar cells will decrease<sup>122</sup>. Recently, researchers  
969 reported several mixing strategies that stabilized the phase without the bandgap  
970 increment<sup>122,123</sup>. However, such incorporation showed short-term stability of no more than



971 several weeks. Meanwhile, the incorporation of external ions that were not well-miscible with  
972 the  $\alpha$ -FAPbI<sub>3</sub> matrix would eventually lead to disorders and heterogeneity in the lattice, and  
973 these heterogeneities would serve as non-radiative recombination centers that deteriorated the  
974 device performance<sup>51</sup>.

975 Other stabilization methods of  $\alpha$ -FAPbI<sub>3</sub> were also reported. Surface functionalization  
976 and dimension reduction are popular due to the recent emergence of low-dimensional halide  
977 perovskites. The reduction of surface energy was accomplished by large-sized/nonconductive  
978 organic molecules<sup>124</sup>. However, such functionalization with organic molecules would prohibit  
979 the transport of charged carriers and, therefore, led to relatively low performance. Recently, a  
980 new confinement strategy of  $\alpha$ -FAPbI<sub>3</sub> stabilization was reported.  $\alpha$ -FAPbI<sub>3</sub> was found to  
981 obtain phase stability within patterned nanochannels<sup>125</sup>. Long-term stability was achieved by  
982 limiting the expansion of  $\alpha$ -FAPbI<sub>3</sub> during phase transition to  $\delta$ -FAPbI<sub>3</sub> with the confinement  
983 of the surrounding nanochannels. However, this method lacked compatibility with  
984 conventional fabrication protocols and could hardly be applied to device integration.  
985 Additionally, encapsulating the  $\alpha$ -FAPbI<sub>3</sub> with mesoporous TiO<sub>2</sub> scaffolds was found to  
986 enhance the phase stability of  $\alpha$ -FAPbI<sub>3</sub><sup>126</sup>. However, the stability didn't last long.

987

## 988 **2. Differences between the epitaxial stabilization and the current methods.**

989 Besides the conventional stabilization by forming mixed perovskite alloys, the  
990 dimensional reduction, as well as the encapsulation effects, are also reported<sup>124,125,127,128</sup>.  
991 Herein, we discuss the differences between these methods with the epitaxial stabilization in

992 this study and demonstrate that the epitaxial stabilization is from neither the dimensional  
993 reduction nor the encapsulation effect.

994 The dimensional reduction of the  $\alpha$ -FAPbI<sub>3</sub> is usually accomplished by forming  
995 two-dimensional  $\alpha$ -FAPbI<sub>3</sub> with several atomic layers or zero-dimensional quantum dot with  
996 a limited number of lattices<sup>124</sup>. This low-dimensional  $\alpha$ -FAPbI<sub>3</sub> is usually capped with  
997 surfactants/capping agents to reduce the surface energy so that the metastable  $\alpha$  phase can be  
998 stabilized. In the case of the epitaxially stabilized  $\alpha$ -FAPbI<sub>3</sub>, however, the thin film is far  
999 beyond several atomic layers and, therefore, will not be considered as the effect of the  
1000 dimensional reduction.

1001 The encapsulation effect is also reported to stabilize the  $\alpha$ -FAPbI<sub>3</sub>. Embedding the  
1002  $\alpha$ -FAPbI<sub>3</sub> into the mesoporous TiO<sub>2</sub> scaffolds was reported to retard the phase transition due  
1003 to the partial encapsulation by the mesoporous TiO<sub>2</sub><sup>126</sup>. Meanwhile, the stabilization of  
1004  $\alpha$ -FAPbI<sub>3</sub> within nanochannel was also reported<sup>125,128</sup>. The encapsulation of the  $\alpha$ -FAPbI<sub>3</sub>  
1005 with the nanochannels prohibits the phase transition by constraining the volume expansion of  
1006  $\alpha$ -FAPbI<sub>3</sub> to  $\delta$ -FAPbI<sub>3</sub> in the nanochannels. However, in both cases, an epitaxial relationship  
1007 between the mesoporous TiO<sub>2</sub>/nanochannel and the constrained  $\alpha$ -FAPbI<sub>3</sub> is not necessary. In  
1008 the case of the epitaxial stabilization, the  $\alpha$ -FAPbI<sub>3</sub> is grown on the substrate with only the  
1009 bottom surface chemically bonded to the substrate. The  $\alpha$ -FAPbI<sub>3</sub> lattice is constrained to the  
1010 substrate, which is the essential difference from the encapsulation method.

1011 By comparing these two methods with the epitaxial growth, we can conclude that both  
1012 the dimensional reduction and the encapsulation effect require the entire  
1013 capping/encapsulation of the  $\alpha$ -FAPbI<sub>3</sub> by either the capping agents or space-confinement

1014 objects. In the epitaxial stabilization, the epitaxial  $\alpha$ -FAPbI<sub>3</sub> grows on the substrate and  
1015 leaves the top surface and the side surfaces uncapped. The stabilization effect comes from the  
1016 coherent growth of the  $\alpha$ -FAPbI<sub>3</sub> with the substrates. During nucleation, the crystallized  
1017 FAPbI<sub>3</sub> will adopt the most conformal atom sequence to accommodate the existing substrate  
1018 crystal structure. Once crystallized, the formed epitaxial lattice will be constrained to the  
1019 substrate due to the strong chemical bonds between them. Therefore, the epitaxial growth is  
1020 also used to stabilize the polymorphs that are unstable under ambient condition<sup>129-131</sup>. The  
1021 origin of the epitaxial stabilization actually comes from the coherent interface rather than the  
1022 reduced dimension or the encapsulation effect. The epitaxial  $\alpha$ -FAPbI<sub>3</sub> thin film strongly  
1023 bonds to the substrate, leaving other surfaces uncapped. Not to mention the passivation effect  
1024 of the surfactant. Therefore, we can exclude the possibility of dimensional reduction and  
1025 encapsulation effects regarding the phase stabilization of  $\alpha$ -FAPbI<sub>3</sub>.

1026 Besides, a recent study shows that the residual strain produced from the thermal  
1027 expansion coefficients difference during the thermal annealing can be used to temporarily  
1028 stabilize the polycrystalline  $\alpha$ -CsPbI<sub>3</sub> film<sup>16</sup>. However, the mechanism is different from the  
1029 internal lattice strain neutralization. The isotropic (to the randomly orientated polycrystalline  
1030 perovskite lattices) residual strain originates from the thermal expansion coefficients  
1031 difference between the glass slide and the polycrystalline perovskites. During cooling down,  
1032 the constraint from the glass will prevent the phase transition of the  $\alpha$ -CsPbI<sub>3</sub> film. The weak  
1033 constraint by van der Waals contact between the glass slides and the perovskite will be  
1034 unstable against the environmental fluctuations and can gradually lose the stabilization effect.  
1035 In the case of chemically epitaxially strained  $\alpha$ -FAPbI<sub>3</sub>, we suggest that strong constraint

1036 from the ionic bond at the epitaxial interface restrict the phase transition, and neutralization  
1037 of the lattice internal tensile strain can also be an important reason for stabilization. The strain  
1038 we applied by epitaxial growth is an anisotropic lattice strain (to the aligned single crystal  
1039 lattices), which is different from the isotropic residual strain from the reported work<sup>16</sup>.

1040

1041

### 1042 **Supplementary Discussion 15: Composition of the Strained $\alpha$ -FAPbI<sub>3</sub>**

1043 To study the composition of the stabilized epitaxial  $\alpha$ -FAPbI<sub>3</sub> thin film, X-ray  
1044 photoelectron spectroscopy (XPS) is used to examine the targeted key elements (I, Pb, Br,  
1045 and Cl), as shown in Extended Data Fig. 8a to 8d. The results indicate a pristine surface of  
1046 the epitaxy  $\alpha$ -FAPbI<sub>3</sub> thin film without any contamination from the Br and Cl elements,  
1047 which excludes the possibility of any stabilization effects by Br and Cl incorporation<sup>48</sup>.

1048

1049

### 1050 **Supplementary Discussion 16: First-Principles Calculations of Epitaxial Stabilization**

1051 First-principles calculations were performed to investigate epitaxial stabilization of  
1052  $\alpha$ -FAPbI<sub>3</sub> with respect to  $\delta$ -FAPbI<sub>3</sub> on MAPbBr<sub>3</sub> substrates. A typical model of epitaxial  
1053 stabilization calculations compares the total energy changes of nucleating the two phases on  
1054 the substrate<sup>132</sup>. Equation (1) shows an expression of this model for this specific system:

$$1055 \quad \Delta E^{\alpha-\delta} = (\Delta E_f^\alpha - \Delta E_f^\delta)d + (\Delta E_s^\alpha - \Delta E_s^\delta)d + (\sigma^{\alpha||S} - \sigma^{\delta||S}) \quad (1)$$

1056 where the terms on the right-hand side for phase  $i$  ( $i = \alpha, \delta$ ) are bulk formation energy ( $\Delta E_f^i$ ),  
1057 strain energy ( $\Delta E_s^i$ ), and interfacial energy ( $\sigma^{i||S}$ , S means substrate) terms. Here, we use

1058 area-specific bulk energy terms ( $\Delta E_f^i$  and  $\Delta E_s^i$ ) by setting the film thickness to  $d = 1$  nm. The  
 1059 sum of the three energy-difference terms is the total energy difference between strained  
 1060  $\alpha$ -FAPbI<sub>3</sub> and  $\delta$ -FAPbI<sub>3</sub> ( $\Delta E^{\alpha-\delta}$ ). A negative  $\Delta E^{\alpha-\delta}$  indicates that growth of  $\alpha$ -FAPbI<sub>3</sub> is  
 1061 energetically more favorable than  $\delta$ -FAPbI<sub>3</sub> on the MAPbBr<sub>3</sub> substrate, and thus the  
 1062 metastable  $\alpha$ -FAPbI<sub>3</sub> is epitaxially stabilized. Calculation details and results for each energy  
 1063 term are discussed below.

1064 The bulk formation energy ( $\Delta E_f^i$ ) is the energy difference between bulk  $i$ -FAPbI<sub>3</sub> and its  
 1065 elemental components, as shown in Equation (2):

$$1066 \quad \Delta E_f^i = E_i - E_{FA} - E_{Pb} - 3E_I \quad (2)$$

1067 Because we are dealing with polymorphs with the same composition, the elemental  
 1068 components for both  $\alpha$  and  $\delta$  phases are the same. The total energy of the FA<sup>+</sup> cation is  
 1069 calculated based on an isolated molecule. Total energies of Pb and I are calculated using their  
 1070 most stable crystal structures, with a space group of  $Fm3m$  and  $Cmce$ , respectively. By  
 1071 setting the film thickness to 1 nm, we get area-specific bulk formation energies  $\Delta E_f^\alpha =$   
 1072  $-2.279 \times 10^{-1} \frac{eV}{\text{\AA}^2}$  and  $\Delta E_f^\delta = -2.31 \times 10^{-1} \frac{eV}{\text{\AA}^2}$ . The results indicate that  $\delta$ -FAPbI<sub>3</sub> is more  
 1073 stable, which agrees with the experimental findings that  $\delta$ -FAPbI<sub>3</sub> is more stable than  
 1074  $\alpha$ -FAPbI<sub>3</sub> at room temperature<sup>40</sup>.

1075 The strain energy of  $i$ -FAPbI<sub>3</sub> ( $\Delta E_s^i$ ) is induced by constraints from the substrate due to  
 1076 epitaxial nucleation and lattice mismatch. It equals to the energy difference between the films  
 1077 with and without the strain (Equation (3)).

$$1078 \quad \Delta E_s^i = E_i^{strained} - E_i \quad (3)$$

1079 In the case of  $\alpha$ -FAPbI<sub>3</sub>, we have confirmed in the experiments that both MAPbBr<sub>3</sub> substrate

1080 and  $\alpha$ -FAPbI<sub>3</sub> film are (001) oriented. Our calculations also show that lattice constants of  
1081  $\alpha$ -FAPbI<sub>3</sub> and MAPbBr<sub>3</sub> have a relatively large mismatch of 6%. Therefore, we can explicitly  
1082 obtain  $E_{\alpha}^{strained}$  in Equation (3) by calculating  $\alpha$ -FAPbI<sub>3</sub> with 6% bi-axial compressive  
1083 strain along  $ab$ -axes. The area-specific  $\Delta E_s^{\alpha}$  is calculated to be  $1.2 \times 10^{-2} \frac{eV}{\text{\AA}^2}$ .

1084 In the case of  $\delta$ -FAPbI<sub>3</sub>, the possible growth model is not straightforward. Therefore, we  
1085 perform a search for the lattice plane of minimal lattice mismatch with MAPbBr<sub>3</sub> (001). The  
1086 hexagonal (001) close-packed plane of  $\delta$ -FAPbI<sub>3</sub> has dimensions of  $a = b = 8.62 \text{ \AA}$  and  $\gamma =$   
1087  $120^\circ$ . Based on this plane, the termination we found that is most compatible with MAPbBr<sub>3</sub>  
1088 (001) substrate has a large vector strain of 13.2% and  $3.43^\circ$ , and an area strain of 18.3%. This  
1089 obviously exceeds the strain threshold for a coherent interface, which is usually below 10%  
1090 <sup>132</sup>. We thus consider  $\delta$ -FAPbI<sub>3</sub> forms incoherent interface with MAPbBr<sub>3</sub> (001). A film with  
1091 the incoherent interface is not constrained by the substrate and the strain energy  $\Delta E_s^{\delta}$  is  
1092 therefore 0.

1093 To calculate the interfacial energy for  $\alpha$ -FAPbI<sub>3</sub> (001)/MAPbBr<sub>3</sub> (001) ( $\sigma^{\alpha||S}$ ), we build  
1094 heterostructural models consisting of  $m$  layers of substrate and  $n$  layers of film. The two  
1095 heterostructural models are shown in Supplementary Fig. 13a. They represent two different  
1096 terminations, namely FAI/PbBr<sub>2</sub> ( $m = 5, n = 9$ ) and PbI<sub>2</sub>/MABr ( $m = 5, n = 11$ ). Note that  
1097 only nine layers of film material are shown in each structure for clarity.

1098 The other two possible terminations for the  $\alpha$ -FAPbI<sub>3</sub> (001)/MAPbBr<sub>3</sub> (001) interfaces  
1099 are FAI/MABr and PbI<sub>2</sub>/PbBr<sub>2</sub> (not shown here). Through initial analysis of bonding  
1100 characteristics, we find that these terminations cannot form ionic bonds between the film and  
1101 the substrate like the Pb-I or Pb-Br bonds in FAI/MABr (PbI<sub>2</sub>/PbBr<sub>2</sub>). ‘Physical contacts’ like

1102 FAI/MABr and  $\text{PbI}_2/\text{PbBr}_2$ <sup>133</sup> at the interface are less stable than ‘chemical contacts’ like  
 1103 FAI/ $\text{PbBr}_2$  and  $\text{PbI}_2/\text{MABr}$ . Therefore, we only focus on FAI/ $\text{PbBr}_2$  and  $\text{PbI}_2/\text{MABr}$  in this  
 1104 investigation.

1105 After the heterostructural models are confirmed, the interfacial energy can be calculated  
 1106 by subtracting the bulk energy of all components in the heterostructural model. Specifically,  
 1107 interfacial energy equations for these two heterostructural models are shown as Equations (4)  
 1108 and (5).

$$1109 \quad \sigma_{TERM1}^{\alpha||S} = \frac{1}{2A} (E_{HS1} - 2 \times E_{MAPbBr_3} - 4 \times E_{FAPbI_3}^{strain} - \mu_{Pb}^{MAPbBr_3} - 2 \times \mu_{Br}^{MAPbBr_3} - \mu_{FA}^{FAPbI_3} -$$

$$1110 \quad \mu_I^{FAPbI_3}) \quad (4)$$

$$1111 \quad \sigma_{TERM2}^{\alpha||S} = \frac{1}{2A} (E_{HS2} - 2 \times E_{MAPbBr_3} - 5 \times E_{FAPbI_3}^{strain} - \mu_{MA}^{MAPbBr_3} - \mu_{Br}^{MAPbBr_3} - \mu_{Pb}^{FAPbI_3} -$$

$$1112 \quad 2 \times \mu_I^{FAPbI_3}) \quad (5)$$

1113 where  $E_{HS}$  is the total energy of the heterostructural model,  $E_{MAPbBr_3}$  is the total energy of  
 1114 the strain-free  $\text{MAPbBr}_3$  lattice,  $E_{FAPbI_3}^{strain}$  is the total energy of the strained  $\alpha\text{-FAPbI}_3$  lattice,  
 1115 and  $\mu$  represents the chemical potentials of the corresponding atoms/molecules. Each of the  
 1116 heterostructural models contains two identical interfaces, and A is the interfacial area.

1117 On the right-hand side, the trailing terms represent the bulk energy of each component in  
 1118 the heterostructure. For example, there are nine layers of  $\alpha\text{-FAPbI}_3$  in FAI/ $\text{PbBr}_2$ , which  
 1119 equals to four intact  $\alpha\text{-FAPbI}_3$  unit cells (each has two layers) plus one extra layer of FAI.  
 1120 The extra or un-stoichiometric components require the determination of their chemical  
 1121 potentials in the corresponding film or substrate material. Here we show in detail how we  
 1122 obtained chemical potentials of un-stoichiometric  $\alpha\text{-FAPbI}_3$  components.

$$1123 \quad \Delta\mu_{FA} + \Delta\mu_{Pb} + 3\Delta\mu_I = \Delta H(FAPbI_3) = -5.78 \text{ eV} \quad (6)$$

1124 
$$\Delta\mu_{Pb} + 2\Delta\mu_I < \Delta H(PbI_2) = -2.02 \text{ eV} \quad (7)$$

1125 
$$\Delta\mu_{FA} + \Delta\mu_I < \Delta H(FAI) = -3.74 \text{ eV} \quad (8)$$

1126 According to thermodynamic stability limits expressed in Equations (6) - (8), we plot the  
 1127 phase diagram for  $\alpha$ -FAPbI<sub>3</sub> against the chemical potential change  $\Delta\mu_I$  and  $\Delta\mu_{Pb}$ .  
 1128 Supplementary Fig. 13b shows the phase diagram, and the long, narrow green region  
 1129 indicates the thermodynamic stability region for the synthesis of  $\alpha$ -FAPbI<sub>3</sub>. We select three  
 1130 representative points throughout the whole region for the following calculations: A  
 1131 ( $\Delta\mu_I = -1.02 \text{ eV}$ ,  $\Delta\mu_{Pb} = 0 \text{ eV}$ ), B ( $\Delta\mu_I = -0.50 \text{ eV}$ ,  $\Delta\mu_{Pb} = -1.03 \text{ eV}$ ), and C  
 1132 ( $\Delta\mu_I = 0 \text{ eV}$ ,  $\Delta\mu_{Pb} = -2.04 \text{ eV}$ ).

1133 Similarly, we obtain the phase diagram for MAPbBr<sub>3</sub> substrate (not shown) and select  
 1134 one representative point P ( $\Delta\mu_{Br} = -0.70 \text{ eV}$ ,  $\Delta\mu_{Pb} = -1.47 \text{ eV}$ ) in the middle of the  
 1135 thermodynamically stable range. The values of point P are used as constants in Equations (4)  
 1136 and (5) for the un-stoichiometric MAPbBr<sub>3</sub> components.

1137 We also added the stability limit for FAI/MABr and PbI<sub>2</sub>/PbBr<sub>2</sub> in the phase diagram  
 1138 (Supplementary Fig. 13b). As the red dashed line shows, FAI/MABr is more stable in the  
 1139 region below this limit, and it covers the whole stability range of  $\alpha$ -FAPbI<sub>3</sub>. Therefore, we  
 1140 only need to calculate the interfacial energy for FAI/MABr, and the results are  $2.86 \times 10^{-4} \text{ eV}$   
 1141  $\text{\AA}^{-2}$ ,  $4.29 \times 10^{-4} \text{ eV \AA}^{-2}$ , and  $2.86 \times 10^{-4} \text{ eV \AA}^{-2}$  at A, B, and C points, respectively. Interestingly,  
 1142 the composition of interfacial terminations and their preferred chemical potential conditions  
 1143 agree with each other. For the  $\delta$ -FAPbI<sub>3</sub>/MAPbBr<sub>3</sub> (001) interface, the interfacial energy  
 1144  $\sigma^{\delta||S}$  is given as  $6.242 \times 10^{-2} \text{ eV \AA}^{-2}$  (i.e.,  $1 \text{ J m}^{-2}$ ), a typical value for incoherent interfaces<sup>132</sup>.

1145 Results for all energy terms in Equation (1) are summarized in Supplementary Table 3.



1146 The calculated total energy change of nucleating  $\alpha$ -FAPbI<sub>3</sub> is around  $-2.155 \times 10^{-1}$  eV  $\text{\AA}^{-2}$   
1147 (regardless of chemical potential conditions), while the value for  $\delta$ -FAPbI<sub>3</sub> is  $-1.6858 \times 10^{-1}$   
1148 eV  $\text{\AA}^{-2}$ . Apparently,  $\Delta E^{\alpha-\delta}$  has a negative value of around  $-4.7 \times 10^{-2}$  eV  $\text{\AA}^{-2}$  (i.e.,  $-0.75$  J  
1149  $\text{m}^{-2}$ ), which indicates epitaxial stabilization of  $\alpha$ -FAPbI<sub>3</sub> with respect to  $\delta$ -FAPbI<sub>3</sub> on  
1150 MAPbBr<sub>3</sub> substrates. This result is comparable to prior successful prediction of epitaxial  
1151 stabilization.

1152 From Supplementary Table 3, we can see that the bulk formation energy is the largest  
1153 term but yields a small difference ( $3.1 \times 10^{-3}$  eV  $\text{\AA}^{-2}$ ) between  $\alpha$ -FAPbI<sub>3</sub> and  $\delta$ -FAPbI<sub>3</sub>. The  
1154 strain energy term is in favor of  $\delta$ -FAPbI<sub>3</sub> by a large value of  $1.2 \times 10^{-2}$  eV  $\text{\AA}^{-2}$ . The main  
1155 contribution to  $\Delta E^{\alpha-\delta}$  is from interfacial energy, which is above  $6 \times 10^{-2}$  eV  $\text{\AA}^{-2}$  and decides  
1156 the overall energy preference. Notably, to accurately determine energetics using DFT  
1157 calculations, we apply a large interfacial mismatch (strain = -6%) to calculate the strain  
1158 energy term for  $\alpha$ -FAPbI<sub>3</sub>. However, the calculations represent an upper limit of strain's  
1159 influence and guarantee a negative  $\Delta E^{\alpha-\delta}$  in lower-strain circumstances. Strains below 6%  
1160 would definitely yield a  $\Delta E_s^\alpha$  less than  $1.2 \times 10^{-2}$  eV  $\text{\AA}^{-2}$  and a more negative  $\Delta E^{\alpha-\delta}$ , which  
1161 better ensures epitaxial stabilization of  $\alpha$ -FAPbI<sub>3</sub>. Another experimental variable is the  
1162 substrate composition. We use MAPbBr<sub>3</sub> as the substrate in the heterostructural model to  
1163 calculate the interfacial energies, but in experiments we also use mixed-halide substrates with  
1164 Cl composition up to MAPbCl<sub>1.50</sub>Br<sub>1.50</sub>. This will not change the conclusion of the  
1165 discussions here because the substrate energy is excluded in the calculation of the interfacial  
1166 energy, as shown in Equations (4) and (5).

1167 Besides, the consideration of the stabilization mechanism is based on the system with

1168 both the  $\alpha$ -FAPbI<sub>3</sub> and substrate lattices rather than just focusing on the  $\alpha$ -FAPbI<sub>3</sub> lattice  
1169 alone. Two different heterostructures (i.e., the  $\alpha$ -FAPbI<sub>3</sub>/substrate and the  $\delta$ -FAPbI<sub>3</sub>/substrate)  
1170 are used to study the interfacial energy of nucleus crystallization during the epitaxial growth.  
1171 The structure with lower interfacial energy will be more favorable during nucleus  
1172 crystallization and, thus, more favorable to form. Calculation results show that the interfacial  
1173 energy of the  $\alpha$ -FAPbI<sub>3</sub>/substrate ( $0.0286 \times 10^{-2}$  eV Å<sup>-2</sup>) is much lower than that of the  
1174  $\delta$ -FAPbI<sub>3</sub>/substrate ( $6.242 \times 10^{-2}$  eV Å<sup>-2</sup>). Therefore, the total energy of the  
1175  $\alpha$ -FAPbI<sub>3</sub>/substrate system is much smaller than that of the  $\delta$ -FAPbI<sub>3</sub>/substrate system  
1176 because of the interfacial energy benefit, which stabilizes the epitaxial  $\alpha$ -FAPbI<sub>3</sub> on the  
1177 substrate. Additionally, the phase transition depends on not only the energy landscapes of  
1178 both phases (phases before/after phase transition), but also the energy barrier between the two  
1179 phases. This is where the epitaxial constraint from the substrate comes into play. In order to  
1180 make the phase transition to happen, the  $\alpha$ -FAPbI<sub>3</sub> need to break the ionic bonds with the  
1181 substrate, which represents a very high energy barrier. Therefore, due to the synergistic  
1182 effects of strain and epitaxial constraint, the  $\alpha$ -FAPbI<sub>3</sub> is stable for long term as observed in  
1183 this study. In summary, our calculations show reliable and robust validation of the epitaxial  
1184 stabilization of  $\alpha$ -FAPbI<sub>3</sub>.

1185

1186

1187 **Supplementary Discussion 17: Stability Investigation of the  $\alpha$ -FAPbI<sub>3</sub> Removed from**  
1188 **the Substrate**

1189           Due to the constraint of the substrate lattice, the epitaxial  $\alpha$ -FAPbI<sub>3</sub> thin film shows  
1190 long-term stability without phase transition. To experimentally demonstrate the phase  
1191 stability originates from the substrate lattice constriction, we partially remove the epitaxial  
1192  $\alpha$ -FAPbI<sub>3</sub> thin film from the substrate and investigate the phase stability of the removed  
1193  $\alpha$ -FAPbI<sub>3</sub>. Due to the limited thickness of the epitaxial  $\alpha$ -FAPbI<sub>3</sub> thin film, it is difficult to  
1194 remove the epitaxial thin film by a sharp razor blade or needle. Therefore, we remove the  
1195 epitaxial  $\alpha$ -FAPbI<sub>3</sub> by polishing a substrate covered with the epitaxial  $\alpha$ -FAPbI<sub>3</sub> thin film  
1196 with a sandpaper. As shown in Supplementary Fig. 14a, removed  $\alpha$ -FAPbI<sub>3</sub> attached to the  
1197 upper half of the sandpaper while the removed substrate (MAPbBr<sub>3</sub> in this case) attached to  
1198 the lower half of the sandpaper due to over-polishing. Meanwhile, the right half of the  
1199 substrate, which remains unpolished, is covered with epitaxial  $\alpha$ -FAPbI<sub>3</sub> while the left half  
1200 exposes the substrate due to the removal of epitaxial  $\alpha$ -FAPbI<sub>3</sub>. The removed  $\alpha$ -FAPbI<sub>3</sub>,  
1201 which attaches to the sandpaper, remains in black  $\alpha$  phase right after removal. After 24 hours,  
1202 the removed  $\alpha$ -FAPbI<sub>3</sub> changes to yellow  $\delta$  phase while the epitaxial  $\alpha$ -FAPbI<sub>3</sub> on the right  
1203 half of the substrate remains black and stable (Supplementary Fig. 14b). This experiment  
1204 shows that the epitaxial stabilization of the  $\alpha$ -FAPbI<sub>3</sub> thin film originates from the constraint  
1205 by the substrate lattice and relies on the existence of the substrate. The MAPbCl<sub>x</sub>Br<sub>3-x</sub>  
1206 substrates are highly stable and therefore the epitaxial  $\alpha$ -FAPbI<sub>3</sub> is expected to be highly  
1207 stable as well.

1208

1209

1210 **Supplementary Discussion 18: Photodetectors Based on the Strained  $\alpha$ -FAPbI<sub>3</sub>**

1211 Based on the device structure and working principles, the halide perovskites  
1212 photodetectors are divided into two main categories: the photodiode-type and the  
1213 photoconductor-type. Here, we fabricate photodetectors with both structures and discuss them  
1214 below.

1215

### 1216 **1. Photodetector with a photoconductor structure**

1217 Photodetectors with a vertical photoconductor structure based on the strained  $\alpha$ -FAPbI<sub>3</sub>  
1218 thin films are fabricated with a structure shown in Supplementary Fig. 15. Compared with the  
1219 photodiode-type one, the photoconductor-type photodetectors will have a much higher  
1220 responsivity and the EQE will be larger than 100% due to the injected carriers<sup>134-136</sup>. All  
1221 devices we tested have a thickness of around 1  $\mu$ m. A transparent ITO electrode is deposited  
1222 as the top electrode with an area of 1 $\times$ 1 mm<sup>2</sup>.  $I$ - $V$  characteristics are measured under -1 V  
1223 bias with a 685-nm laser as the excitation source. The responsivity of the photodetectors is  
1224 calculated by:

$$1225 \quad R = (J_{light} - J_{dark})/P,$$

1226 where  $J_{light}$  and  $J_{dark}$  are the current densities under illumination and dark conditions,  
1227 respectively, and  $P$  is the input light power density. Extended Data Fig. 9a shows the  
1228 responsivity of photodetectors at different strain levels under 0.015 W cm<sup>-2</sup> illumination.  
1229 Compared with the strain-free device, devices at -0.8%, -1.2%, and -1.4% strain levels show  
1230 enhanced responsivity. Further increasing the compressive strain level will lead to a  
1231 deterioration of the responsivity due to the accumulation of defects. Supplementary Table 4  
1232 summarizes the highest responsivity measured on  $\alpha$ -FAPbI<sub>3</sub> in the literature. The

1233 responsivity of the device is comparable with the highest responsivity of a strain-free system  
1234 with a similar device structure but at a much weaker illumination and higher bias voltage.

1235 Besides, the detectivity, which characterizes how weak light can be detected, and the  
1236 gain, which describes the number of charges flowing through an external circuit per incident  
1237 photon, are calculated by:

$$1238 \quad D = R / \sqrt{2qJ_d} \text{ and } G = 1240R / 685$$

1239 where  $D$  is the detectivity,  $R$  is the responsivity,  $q$  is element charge,  $J_d$  is the dark  
1240 current density, and  $G$  is the gain. They are also plotted as a function of illumination power  
1241 level for both -1.2% strained and strain-free devices (Extended Data Fig. 9b, c). Results  
1242 demonstrate that the strained device has better performance than the strain-free device.

1243 Normalized external quantum efficiency (EQE) spectra are shown in Extended Data Fig.  
1244 9d to highlight the extended absorption range of the strained device compared with the  
1245 strain-free device.

1246

## 1247 **2. Photodetectors with a photodiode structure**

1248 With electrons/holes blocking layers, the photodiode-type photodetectors exhibit a  
1249 minimized dark current by blocking the external current injection. In this study, we aim at  
1250 fabricating a detector with high responsivity. Therefore, we fabricate and test the  
1251 photodetector with the photodiode structure for comparison. We fabricated a photodiode-type  
1252 photodetector by inserting poly(3,4-ethylenedioxythiophene) polystyrene sulfonate  
1253 (PEDOT:PSS) as the hole transporting layer and tin oxide ( $\text{SnO}_2$ ) as the electron transporting  
1254 layer. The structure of the photodiode type photodetector is

1255 Au/PEDOT:PSS/FAPbI<sub>3</sub>/SnO<sub>2</sub>/ITO, which is shown in Supplementary Fig. 16a. From the  
1256 band diagram, the carrier injection under reverse bias is blocked due to the large energy  
1257 barrier. The characterization of the photodetector was carried out with a 685-nm red laser,  
1258 which is selected based on the highest EQE wavelength, under different input power levels.  
1259 Supplementary Fig. 16b shows the  $I$ - $V$  curves of the photodetector under the dark condition  
1260 as well as under 1  $\mu$ W illumination. The  $I$ - $V$  curves show a typical diode-like behavior while  
1261 the dark current under -0.5 V is measured to be  $\sim 2 \times 10^{-8}$  A. This value is more than two orders  
1262 of magnitude lower than that of the photoconductor type detector. However, under the same  
1263 illumination power level, the photocurrent is much smaller than that of the photoconductor  
1264 type detector ( $\sim 600$  times lower at a  $10^{-6}$  W incident power), and therefore, leads to a lower  
1265 responsivity ( $\sim 500$  times lower at a  $10^{-6}$  W incident power). The responsivity and the  
1266 photocurrent under different illumination power levels are also shown in Supplementary Fig.  
1267 16c. Under different illumination power levels, the responsivity of the photodetector is  
1268 always lower than  $1 \text{ A W}^{-1}$  (in comparison with the responsivity of  $200 \text{ A W}^{-1}$  of the  
1269 photoconductor type detector), indicating the block of external current injection with the  
1270 presence of the different transporting layers.

1271

1272

### 1273 **Supplementary Discussion 19: Broader Impact of the Epitaxial System**

1274 The technique we developed enables the controllable strain engineering of halide  
1275 perovskites with epitaxial growth, which has a fundamental difference from the previous  
1276 works. The free-standing  $\alpha$ -FAPbI<sub>3</sub> suffers from severe phase transition under room

1277 temperature while the epitaxial strain can stabilize the  $\alpha$ -FAPbI<sub>3</sub> without changing the  
1278 perovskite composition. The pure phase  $\alpha$ -FAPbI<sub>3</sub> with long-term stability is a property that  
1279 is absent in the free-standing  $\alpha$ -FAPbI<sub>3</sub>.

1280 Secondly, the epitaxial system we developed is a generalized approach that can  
1281 presumably be applied to the entire halide perovskites family. We have already demonstrated  
1282 the growth of epitaxial  $\alpha$ -FAPbI<sub>3</sub> on various substrates, which means that we can grow  
1283 various epitaxial halide perovskites on one or multiple halide perovskite substrates.

1284 Additionally, the epitaxial strain can be applied to stabilize polymorphs of metastable  
1285 perovskites. Perovskites with new compositions are recently predicted through computational  
1286 designs<sup>137</sup>. However, those predicted new perovskites with novel optical and electronic  
1287 properties may have unstable crystal structures under room temperature or normal working  
1288 conditions. In this case, epitaxial stabilization can potentially be applied to stabilize these  
1289 unstable or metastable perovskites on suitable substrates. The reported approach can be  
1290 generalized to other halide perovskites with different compositions and structures.

1291 **Supplementary Table 1. Summary of the substrate growth precursor ratios, the**  
 1292 **resulting substrate compositional Br ratios, and lattice parameters.**

Cl/Br Solution Ratio	Compositional Br Ratio (%)	Formula	Lattice Parameter (Å)
Cl Only	0	MAPbCl <sub>3.00</sub> Br <sub>0.00</sub>	5.70
1/2	50.0	MAPbCl <sub>1.50</sub> Br <sub>1.50</sub>	5.83
1/2.5	58.0	MAPbCl <sub>1.25</sub> Br <sub>1.75</sub>	5.86
1/3	62.1	MAPbCl <sub>1.15</sub> Br <sub>1.85</sub>	5.87
1/4	64.3	MAPbCl <sub>1.05</sub> Br <sub>1.95</sub>	5.88
1/6	76.8	MAPbCl <sub>0.70</sub> Br <sub>2.30</sub>	5.89
1/8	80.6	MAPbCl <sub>0.60</sub> Br <sub>2.40</sub>	5.90
1/19	85.2	MAPbCl <sub>0.45</sub> Br <sub>2.55</sub>	5.92
Br Only	100	MAPbCl <sub>0.00</sub> Br <sub>3.00</sub>	5.95

1293  
 1294 **Supplementary Table 2. Summary of epitaxial growth substrates and the corresponding**  
 1295 **strain measured in  $\alpha$ -FAPbI<sub>3</sub>.**

Substrate Composition	$\alpha$ -FAPbI <sub>3</sub> (001) Peak (degree)	Strain (%)
MAPbCl <sub>1.50</sub> Br <sub>1.50</sub>	13.82	-2.4
MAPbCl <sub>1.05</sub> Br <sub>1.95</sub>	13.84	-1.9
MAPbCl <sub>0.70</sub> Br <sub>2.30</sub>	13.86	-1.4
MAPbCl <sub>0.60</sub> Br <sub>2.40</sub>	13.87	-1.2
MAPbCl <sub>0.00</sub> Br <sub>3.00</sub>	13.89	-0.8

1296  
 1297 **Supplementary Table 3. Thermodynamic terms relevant to epitaxial nucleation of**  
 1298  **$\alpha$ -FAPbI<sub>3</sub> and  $\delta$ -FAPbI<sub>3</sub> on cubic MAPbBr<sub>3</sub> substrates.**

	$\alpha$ -FAPbI <sub>3</sub>			$\delta$ -FAPbI <sub>3</sub>
	A	B	C	--
$\Delta E_f$	$-22.79 \times 10^{-2}$			$-23.10 \times 10^{-2}$
$\Delta E_s$	$1.20 \times 10^{-2}$			0
$\sigma$	$0.0286 \times 10^{-2}$	$0.0429 \times 10^{-2}$	$0.0286 \times 10^{-2}$	$6.242 \times 10^{-2*}$
$\Delta E$	$-21.5614 \times 10^{-2}$	$-21.5471 \times 10^{-2}$	$-21.5614 \times 10^{-2}$	$-16.858 \times 10^{-2}$
$\Delta E (\alpha-\delta)$	$-4.7034 \times 10^{-2}$	$-4.6891 \times 10^{-2}$	$-4.7034 \times 10^{-2}$	--



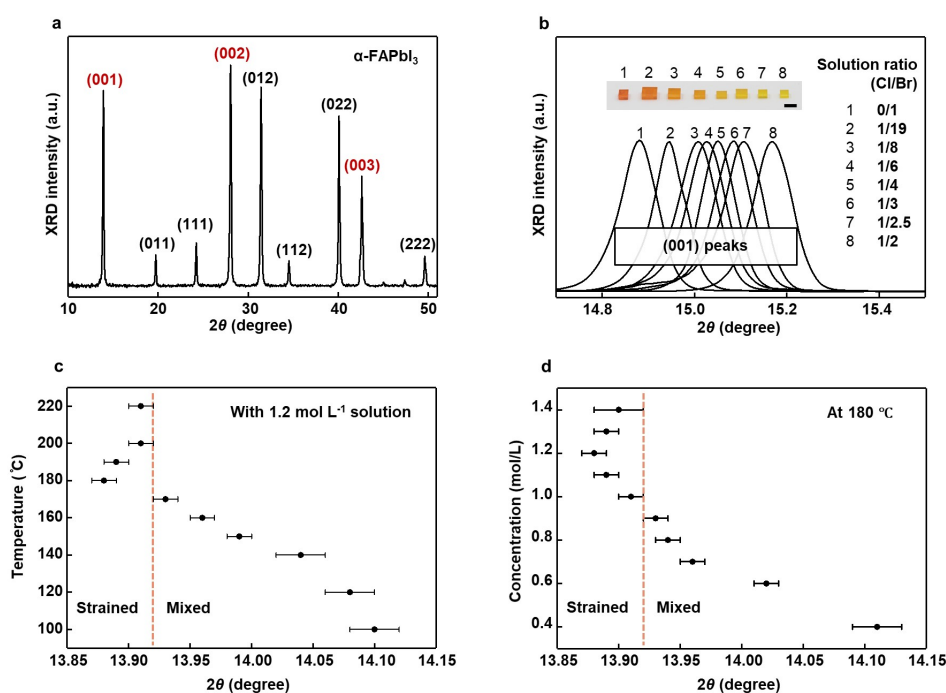
1299 The bulk formation energy ( $\Delta E_f$ ), strain energy ( $\Delta E_s$ ), interfacial energy ( $\sigma$ ), total energy  
 1300 change ( $\Delta E$ ), and the difference between of the two phases ( $\Delta E (\alpha-\delta)$ ) are in eV  $\text{\AA}^{-2}$ . The  
 1301 value marked with \* indicates that the interface between the substrate and the  $\delta$ -FAPbI<sub>3</sub> is  
 1302 considered incoherent, and the interfacial energy term is set at  $1 \text{ J m}^{-2} = 6.242 \times 10^{-2} \text{ eV \AA}^{-2}$ .

1303

1304 **Supplementary Table 4. Summary of representative halide perovskite photodetectors**  
 1305 **with high responsivities in the literature.**

Device structure	Structure	Highest R	Light power	Bias	References
Au/MAPbBr <sub>3</sub> /Au	Planar	$\sim 10 \text{ A W}^{-1}$	$0.01 \text{ mW cm}^{-2}$	-2 V	138
Cr/MAPbI <sub>3</sub> /Cr	Planar	$\sim 20 \text{ A W}^{-1}$	$0.1 \text{ mW cm}^{-2}$	-1 V	139
Au/MAPbI <sub>3</sub> /Au	Planar	$\sim 20.4 \text{ A W}^{-1}$	$2 \mu\text{W cm}^{-2}$	-1.5 V	140
Au/MAPbBr <sub>3</sub> /Au	Planar	$40 \text{ A W}^{-1}$	$54 \mu\text{W}$	-5 V	141
Au/ (BA) <sub>2</sub> (MA) <sub>n-1</sub> Pb <sub>n</sub> I <sub>3n+1</sub> NWs/Au	Planar	$2 \times 10^4$ $\text{A W}^{-1}$	$10^{-6} \text{ mW cm}^{-2}$	-2 V	106
Au/FAPbI <sub>3</sub> /ITO	Vertical	$1.3 \times 10^6$ $\text{A W}^{-1}$	$1.1 \times 10^{-7} \text{ W cm}^{-2}$	-1 V	This Work

1306



1307

1308

1309

1310

1311

1312

1313

1314

1315

1316

1317

1318

1319

1320

1321

1322

1323

1324

1325

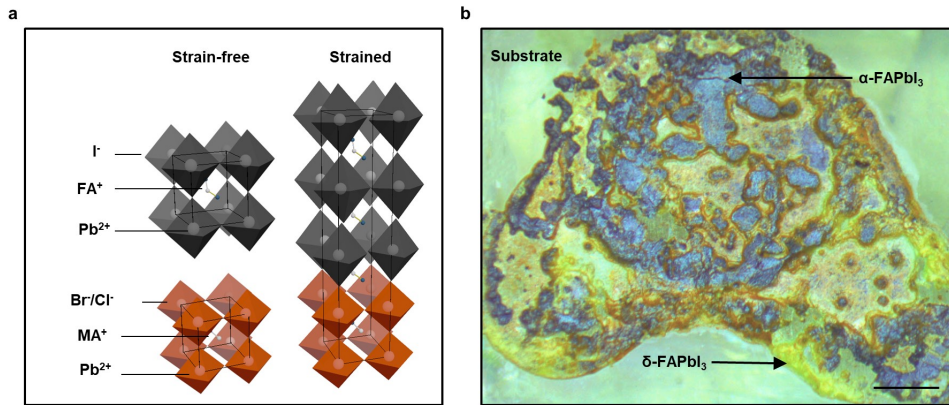
1326

1327

1328

1329

**Supplementary Fig. 1 | Characterization of the lattice parameters and the study of growth condition.** **a**, Powder XRD pattern of  $\alpha$ -FAPbI<sub>3</sub>, which is used as a reference of strain-free  $\alpha$ -FAPbI<sub>3</sub>. The lattice parameter of cubic  $\alpha$ -FAPbI<sub>3</sub> is calculated to be 6.35 Å using the (001) diffraction peak at 13.92°. Peaks from {001} directions are labeled in red. **b**, Powder XRD patterns of substrates with different ratios of the composition. By tuning the Cl/Br molar ratio in the growth solution, we can change the Cl/Br ratio as well as the lattice parameter of the substrate crystal. We note that MAPbCl<sub>3.00</sub>Br<sub>0.00</sub>, MAPbCl<sub>0.00</sub>Br<sub>3.00</sub>, and their alloys all have cubic structures. Lattice parameters can be directly calculated by the 2 $\theta$  peak positions. The inset is an optical image of the corresponding substrates with different Cl/Br ratios. All powders are made by grinding the bulk single crystals. Scale bar: 5 mm. **c**, XRD (100) peak positions of  $\alpha$ -FAPbI<sub>3</sub> at different growth temperatures. The temperature to grow  $\alpha$ -FAPbI<sub>3</sub> with the highest strain is found to be ~180°C. Further increasing the growth temperature results in a high growth rate and a thick epitaxial layer of  $\alpha$ -FAPbI<sub>3</sub> and therefore low crystal quality that relaxes the strain. Decreasing the growth temperature below 180°C can lead to slow crystallization and thus a mixed epitaxial alloy layer at the interface, which shifts the XRD peak position to higher angles. **d**, XRD (100) peak positions of  $\alpha$ -FAPbI<sub>3</sub> at different growth solution concentrations. Concentrations above 1.2 mol L<sup>-1</sup> result in high defect concentration and therefore strain relaxation, due to the fast crystallization rate and the thick epitaxial layer. Concentrations below 1.0 mol L<sup>-1</sup> will slow down the crystallization process and lead to a mixed epitaxial alloy layer at the interface. The vertical dash lines in **c** and **d** show the peak position of a strain-free powder sample. (a.u., arbitrary units).



1330

1331

1332

1333

1334

1335

1336

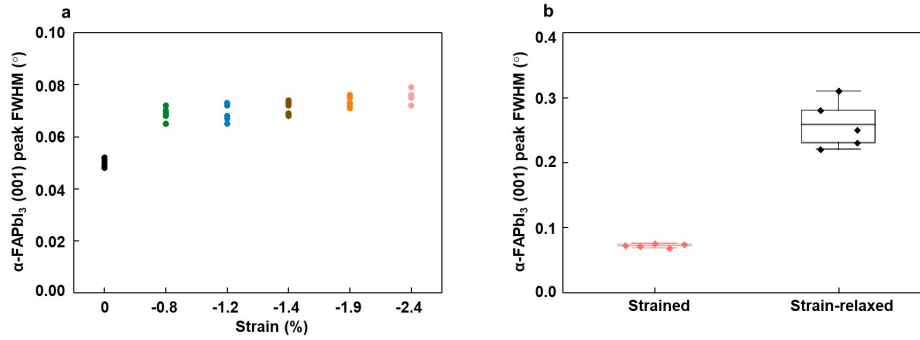
1337

1338

1339

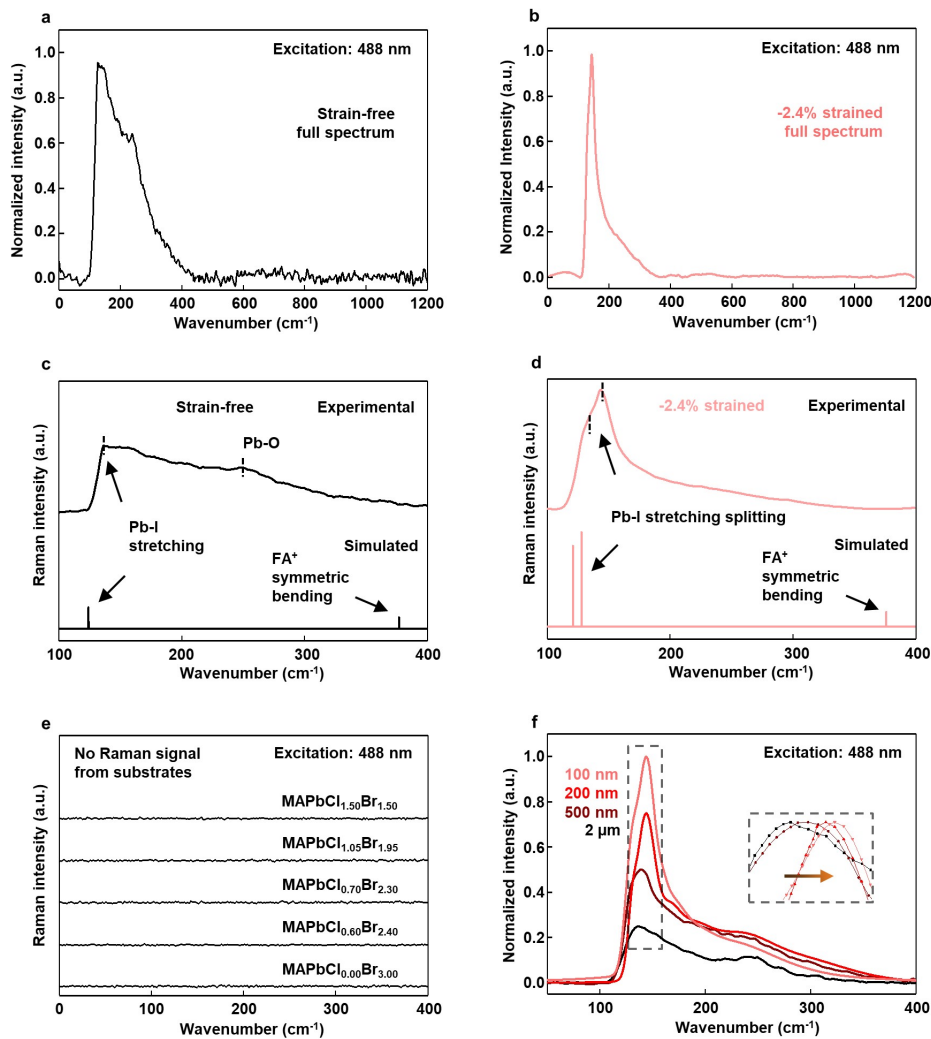
1340

**Supplementary Fig. 2 | Schematic crystal structures of epitaxial  $\alpha$ -FAPbI<sub>3</sub> on MAPbCl<sub>x</sub>Br<sub>3-x</sub> and the optical image of  $\alpha$ -FAPbI<sub>3</sub> on a Cl-rich substrate. a**, Schematic crystal structures of  $\alpha$ -FAPbI<sub>3</sub>, MAPbCl<sub>x</sub>Br<sub>3-x</sub>, and the epitaxial heterostructure showing the crystallographic orientation of the epitaxial  $\alpha$ -FAPbI<sub>3</sub> and the MAPbCl<sub>x</sub>Br<sub>3-x</sub> substrate, with distorted PbI<sub>6</sub> octahedron inorganic framework in the epitaxial layer under compressive interfacial strain. **b**, An optical image of FAPbI<sub>3</sub> grown on MAPbCl<sub>2.00</sub>Br<sub>1.00</sub> substrate using the same growth method as the other substrates. Due to the large lattice mismatch between the substrate and  $\alpha$ -FAPbI<sub>3</sub>, the  $\alpha$ -FAPbI<sub>3</sub> crystallizes randomly rather than epitaxially on the substrate surface. The lack of epitaxial stabilization leads to quick phase transformation from metastable  $\alpha$ -FAPbI<sub>3</sub> to  $\delta$ -FAPbI<sub>3</sub> at room temperature. Scale bar: 200  $\mu$ m.



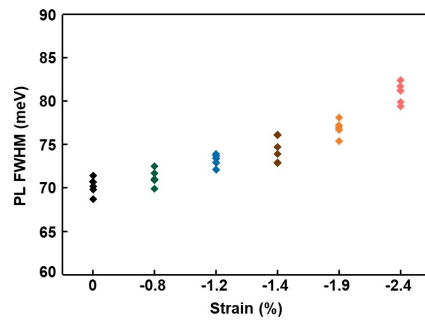
1341  
1342  
1343  
1344  
1345  
1346  
1347  
1348  
1349  
1350

**Supplementary Fig. 3 | XRD diffraction peak FWHM.** **a**, Diffraction peak FWHM study of the epitaxial  $\alpha$ -FAPb<sub>3</sub> thin films under different strain magnitudes. Results show that the epitaxially strained  $\alpha$ -FAPb<sub>3</sub> thin films have a relatively higher diffraction peak FWHM than that of the strain-free  $\alpha$ -FAPb<sub>3</sub> crystal due to the lattice strain and the reduced dimension. **b**, statistical study of the  $\alpha$ -FAPb<sub>3</sub> (001) peak FWHM of the strained and the strain-relaxed samples. Results show that the diffraction peak FWHM of the strained epitaxial  $\alpha$ -FAPb<sub>3</sub> thin films ( $\sim 0.07^\circ$ ) is  $\sim 3$  times smaller than that of the strain-relaxed one ( $\sim 0.25^\circ$ ). Note the strain-relaxed epitaxial  $\alpha$ -FAPb<sub>3</sub> thin films come from Extended Data Fig. 1g. Number of experiments  $n = 5$  for each strain value.



1351  
 1352 **Supplementary Fig. 4 | Raman spectra of  $\alpha$ -FAPbI<sub>3</sub> and the substrates.** Raman full  
 1353 spectra of **a**, strain-free  $\alpha$ -FAPbI<sub>3</sub> bulk crystal and **b**, -2.4% strained  $\alpha$ -FAPbI<sub>3</sub> thin film  
 1354 showing the absence of other peaks outside the range of 100 to 400 cm<sup>-1</sup>. The strain-free  
 1355  $\alpha$ -FAPbI<sub>3</sub> crystal is less Raman-active than the strained  $\alpha$ -FAPbI<sub>3</sub> thin film, so the relative  
 1356 peak intensity of the strain-free crystal is much weaker. The comparison of the experimental  
 1357 and simulated Raman spectra of the **c**, strain-free, and **d**, -2.4% strained  $\alpha$ -FAPbI<sub>3</sub> lattices.  
 1358 The discrepancy between experimental and simulated Pb-I stretching wavenumbers may be  
 1359 due to the anharmonicity of the bonds and the van der Waals interactions between the  
 1360 inorganic cages and organic cations. For the strained lattice, an obvious peak splitting takes  
 1361 place in both the experimental and the simulated spectra. The splitting of the Pb-I symmetric  
 1362 stretching peak originates from the in-plane compression and out-of-plane stretching, while  
 1363 the intensity enhancement comes from the breakage of the cubic symmetry. The weak FA<sup>+</sup>  
 1364 cation bending peak at 377 cm<sup>-1</sup> fails to be detected, which is due to the dynamic FA<sup>+</sup> cation  
 1365 rotation at room temperature. **e**, Raman spectra of MAPbCl<sub>0.00</sub>Br<sub>3.00</sub>, MAPbCl<sub>0.60</sub>Br<sub>2.40</sub>,  
 1366 MAPbCl<sub>0.70</sub>Br<sub>2.30</sub>, MAPbCl<sub>1.05</sub>Br<sub>1.95</sub>, and MAPbCl<sub>1.50</sub>Br<sub>1.50</sub> substrates with a 488-nm laser as  
 1367 the excitation source. No Raman signals can be detected in the wavenumber range of interest.  
 1368 Therefore, possible interference from the substrates can be excluded. **f**, Thickness-dependent  
 1369 Raman spectra of -2.4% strained  $\alpha$ -FAPbI<sub>3</sub> samples. Strained  $\alpha$ -FAPbI<sub>3</sub> thin film has a sharp

1370 and strong signal, which can be attributed to the increased tetragonality of the crystal  
1371 structure. As the film thickness increases, the strain gets gradually relaxed and the lattice  
1372 transforms back to less Raman-active cubic structure. The Raman peak position also shifts to  
1373 lower wavenumbers because of the softer and longer Pb-I bonds (inset image).



1374

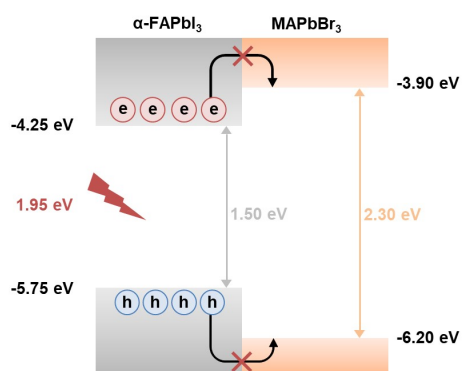
1375

1376

1377

1378

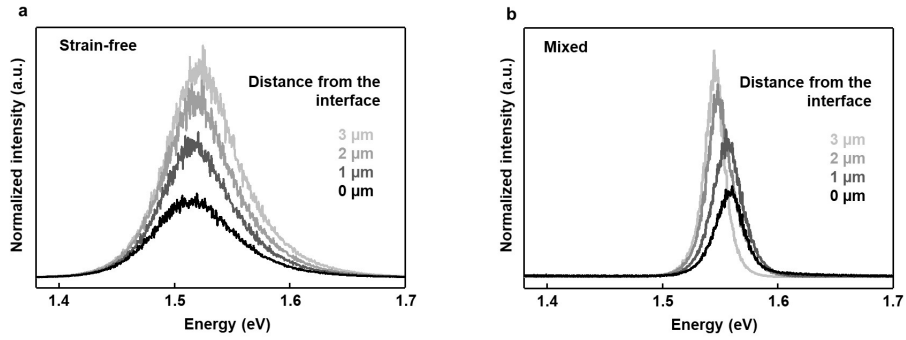
**Supplementary Fig. 5 | FWHM of the PL peaks of epitaxial layers under different strains.** The results show that the FWHM of the PL peak increases with the strain, due to the strain-induced dislocations that broaden the PL peak. A bulk  $\alpha$ -FAPbI<sub>3</sub> single crystal is used as the strain-free reference. Note the number of experiments  $n = 5$  for each strain value.



1379

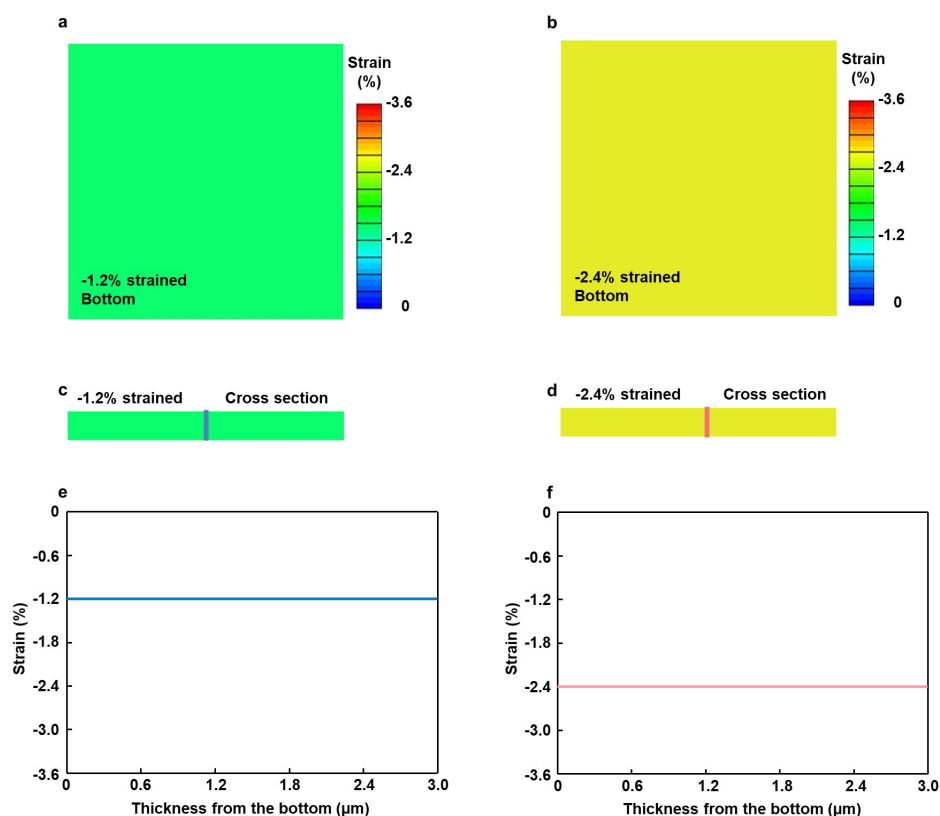
1380 **Supplementary Fig. 6 | Band diagram of the heterostructure and the interfacial charge**  
 1381 **transfer.** Excited carriers in the  $\alpha$ -FAPbI<sub>3</sub> will not transfer to the MAPbBr<sub>3</sub> due to the energy  
 1382 barrier. The analysis shows that the charged carrier transfer in the heterojunction can be  
 1383 excluded due to the straddling band alignment with a prohibited carrier transfer direction and  
 1384 a large energy barrier.





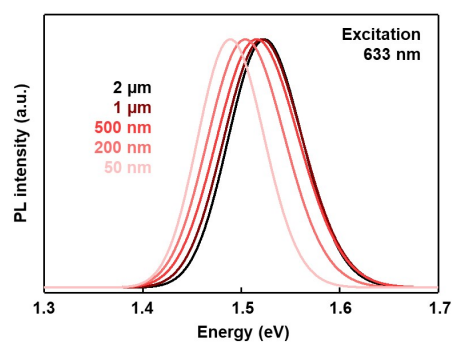
1385  
 1386  
 1387  
 1388  
 1389  
 1390  
 1391  
 1392  
 1393  
 1394

**Supplementary Fig. 7 | Focal point dependent PL measurements of strain-free and mixed  $\alpha$ -FAPbI<sub>3</sub>.** **a**, Focal-point-dependent confocal PL spectra of a strain-free  $\alpha$ -FAPbI<sub>3</sub> bulk crystal. The redshift of the PL peak from  $\sim 1.523$  eV to  $\sim 1.516$  eV, less pronounced than the PL peak redshift of the strained sample in Fig. 2b, is due to reabsorption. **b**, Focal-point-dependent confocal PL spectra of a mixed epitaxial  $\alpha$ -FAPbI<sub>3</sub> grown at a low temperature. Note the mixed sample came from the mixed epitaxial growth with low temperature and low concentration in Supplementary Fig. 1. The increase of focus depth causes the PL peak to blueshift, due to the increase of Br and Cl incorporation in the epitaxial layer.



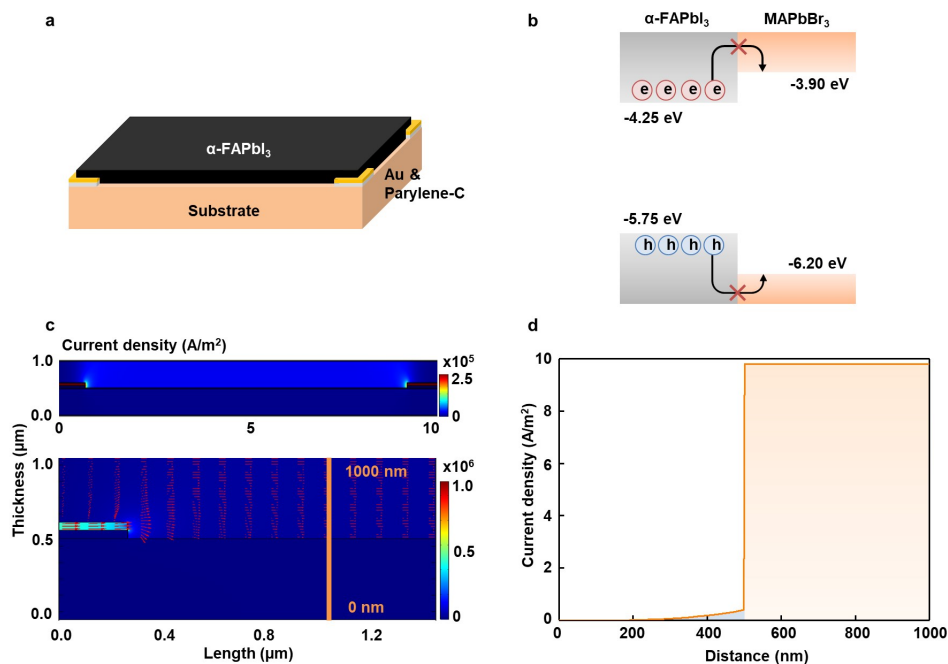
1395

1396 **Supplementary Fig. 8 | Elastic strain relaxation study of the epitaxial  $\alpha$ -FAPbI<sub>3</sub> thin**  
 1397 **films.** Planar strain distribution of the  $\alpha$ -FAPbI<sub>3</sub> with **a**, -1.2% and **b**, -2,4% strain. Vertical  
 1398 strain distribution of the  $\alpha$ -FAPbI<sub>3</sub> with **c**, -1.2% and **d**, -2,4% strain. Results show uniform  
 1399 strain distribution in both  $\alpha$ -FAPbI<sub>3</sub> thin films. Thickness-dependent strain distribution of the  
 1400  $\alpha$ -FAPbI<sub>3</sub> with **e**, -1.2% and **f**, -2,4% strain. Colors are correlated with the lines in **c** and **d**.  
 1401 Results indicate that the elastic strain relaxations in both  $\alpha$ -FAPbI<sub>3</sub> thin film are 0.096% and  
 1402 0.093%, respectively.



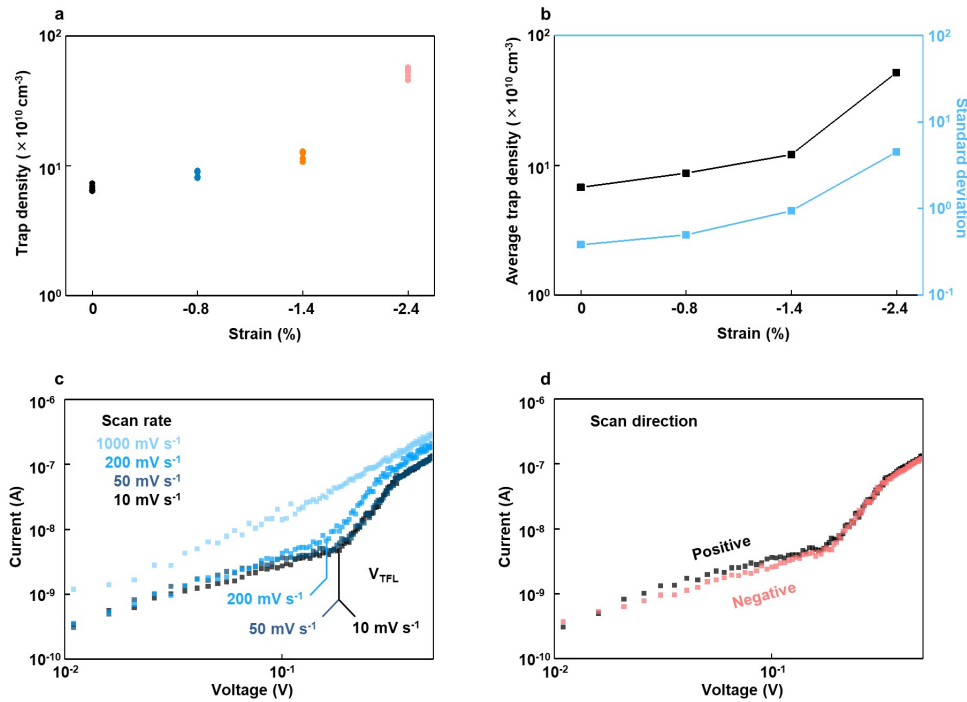
1403

1404 **Supplementary Fig. 9 | Film-thickness-dependent PL measurements of epitaxial**  
1405  **$\alpha$ -FAPbI<sub>3</sub> on MAPbCl<sub>1.50</sub>Br<sub>1.50</sub>.** The PL properties of strained  $\alpha$ -FAPbI<sub>3</sub> films show a  
1406 strong thickness dependence. As the film thickness increases, the PL position gradually shifts  
1407 back to the position of the free-standing bulk crystals. This can be attributed to the plastic  
1408 strain relaxation as the film gets thicker.



1409  
 1410  
 1411  
 1412  
 1413  
 1414  
 1415  
 1416  
 1417  
 1418  
 1419  
 1420

**Supplementary Fig. 10 | Possible carrier collection by the interfacial carrier transfer during Hall effect measurements.** **a**, The schematic structure of the device. Parylene-C (grey) is used as an insulating layer to prevent the injection of carriers from the Au electrode (yellow) to the substrate. **b**, The bandgap diagram of the heterostructure shows that the large energy barrier between the  $\alpha$ -FAPbI<sub>3</sub> and the MAPbBr<sub>3</sub> blocks the carrier injection to the MAPbBr<sub>3</sub>. **c**, Current density distribution by FEA simulation. The upper panel shows the current mapping where the current density in the epitaxial layer is much higher than that of the substrate. The lower panel shows the zoomed-in current distribution image around the electrode. Red arrows show the direction of current flow, which suggests a minimal carrier injection into the substrate due to the energy. **d**, Current density distribution along the vertical orange line in **c**, where the current in the substrate takes 0.8% of the total current.



1421

1422

1423

1424

1425

1426

1427

1428

1429

1430

1431

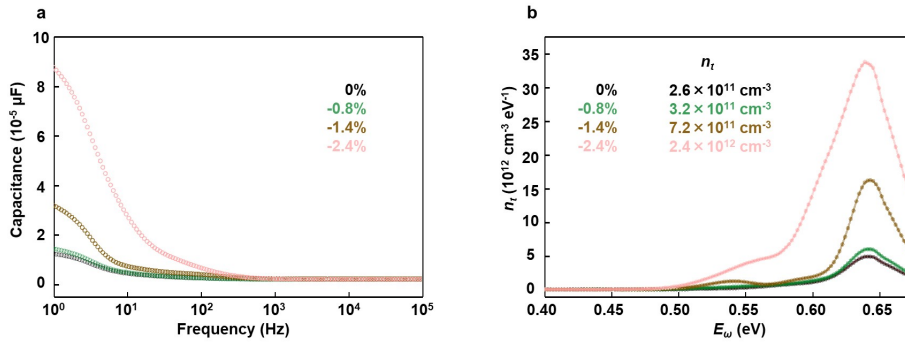
1432

1433

1434

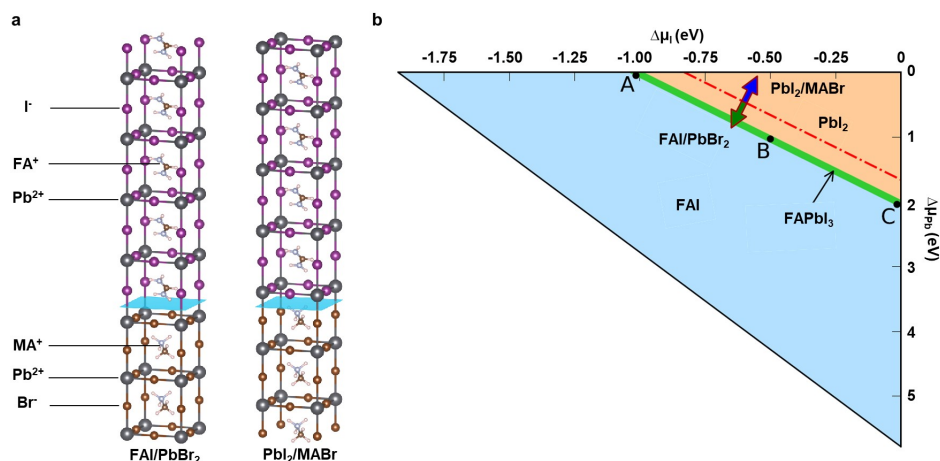
1435

**Supplementary Fig. 11 | SCLC measurements of the epitaxial  $\alpha$ -FAPbI<sub>3</sub> with different strains.** **a**, Strain-dependent trap density of the epitaxial  $\alpha$ -FAPbI<sub>3</sub>. Note the number of experiments  $n = 5$  for each strain value. **b**, Statistics of the strain-dependent trap density. Results show that the average trap density will increase with increasing the strain, which can be attributed to the strain-induced defects. Meanwhile, the standard deviation of the trap density values also increases with the strain, indicating the increased disorder due to the higher defect density with the strain. **c**, Scan-rate-dependent  $I$ - $V$  curves.  $I$ - $V$  curves with 10  $\text{mV s}^{-1}$  and 50  $\text{mV s}^{-1}$  scan rates are similar, indicating that these scan rates are sufficiently slow to avoid artificial results. The  $I$ - $V$  curve with 200  $\text{mV s}^{-1}$  results in a smaller  $V_{TFL}$  because of the limited response of free carriers from the fast scan. Further increasing the scan rate to 1000  $\text{mV s}^{-1}$  leads to the vanish of the trap-filling process. **d**,  $I$ - $V$  curves with different scan directions of the same device. The high similarity of the two curves concludes that the scan direction will not affect the SCLC measurements due to the symmetric Au/Perovskite/Au device structure.



1436  
 1437  
 1438  
 1439  
 1440  
 1441  
 1442  
 1443  
 1444  
 1445

**Supplementary Fig. 12 |  $C$ - $\omega$  measurements of the epitaxial  $\alpha$ -FAPbI<sub>3</sub> to evaluate the trap density.** **a**,  $C$ - $\omega$  spectra of the epitaxial  $\alpha$ -FAPbI<sub>3</sub> thin films with different strain magnitudes. The low-frequency capacitance originates from the carrier trapping/detrapping processes. The larger capacitance at a higher strain magnitude suggests a higher density of traps. The high-frequency capacitance is attributed to the geometrical capacitance and the depletion capacitance. **b**, Trap density distribution extracted from the  $C$ - $\omega$  spectra. An obvious trap density increment is evident with increasing the strain magnitude. The fitted trap densities ( $n_t$ ) by the Gaussian distribution equation indicate a higher trap density at a higher strain magnitude.



1446

1447 **Supplementary Fig. 13 | First-principles calculations of epitaxial stabilization. a,**

1448 Schematic heterostructural models used to calculate the epitaxial  $\alpha$ -FAPbI<sub>3</sub> (001)/MAPbBr<sub>3</sub>

1449 (001) interface. The two interface terminations studied are FAI/PbBr<sub>2</sub> and PbI<sub>2</sub>/MABr. In

1450 each model, the blue plane indicates the interface, the upper section indicates the FAPbI<sub>3</sub> film,

1451 and the lower section indicates the MAPbBr<sub>3</sub> substrate. **b,** Calculated phase diagram for

1452  $\alpha$ -FAPbI<sub>3</sub> and epitaxial  $\alpha$ -FAPbI<sub>3</sub> (001)/MAPbBr<sub>3</sub> interface. The long, narrow region marked

1453 in green depicts the thermodynamically stable range for equilibrium growth of  $\alpha$ -FAPbI<sub>3</sub>

1454 under different I and Pb chemical potentials. Outside this region, the compound decomposes

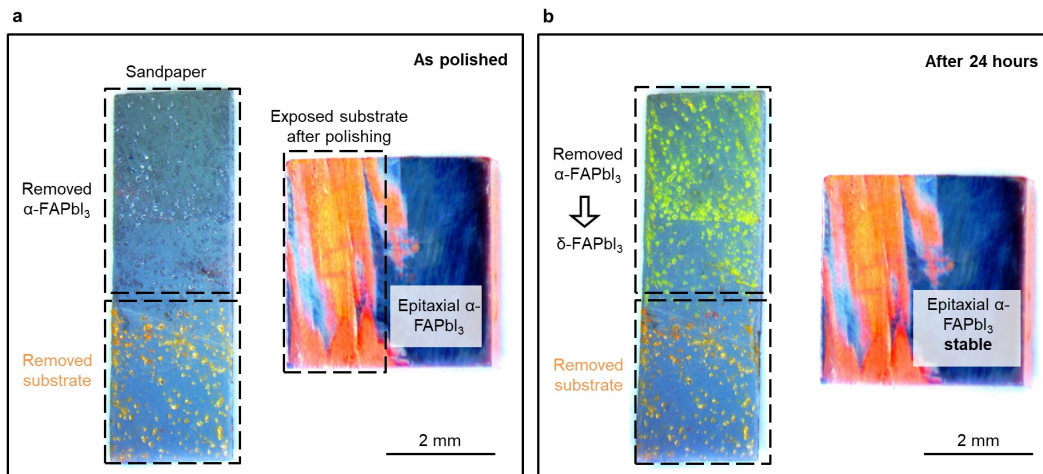
1455 into FAI or PbI<sub>2</sub>. Three representative points A ( $\Delta\mu_I = -1.02$  eV,  $\Delta\mu_{Pb} = 0$  eV), B ( $\Delta\mu_I =$

1456  $-0.50$  eV,  $\Delta\mu_{Pb} = -1.03$  eV), and C ( $\Delta\mu_I = 0$  eV,  $\Delta\mu_{Pb} = -2.04$  eV) are selected for calculating

1457 the interfacial energy. The red dashed line separates the phase diagram into stability regions

1458 of the two different interfacial terminations in **a**.  $\mu$  represents the chemical potentials of the

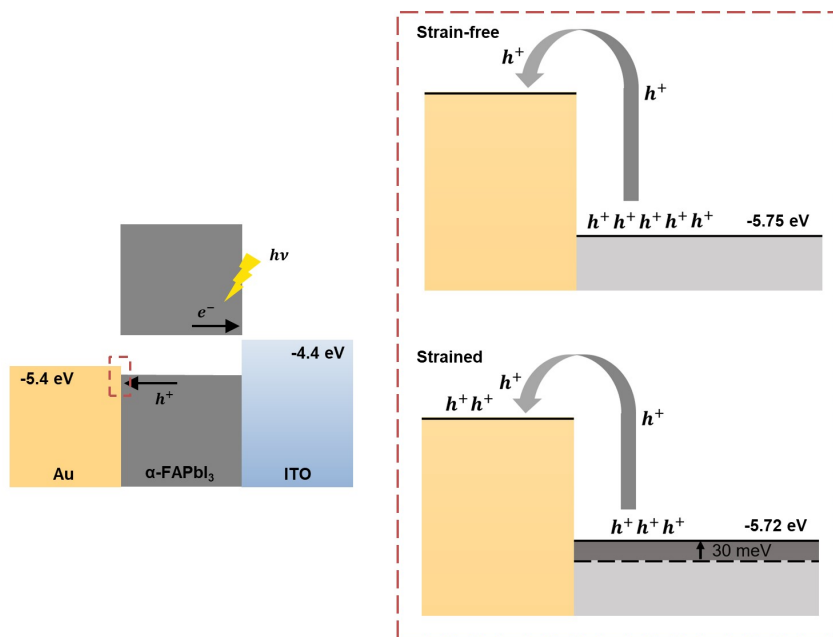
1459 corresponding atoms.



1460  
 1461  
 1462  
 1463  
 1464  
 1465  
 1466  
 1467  
 1468

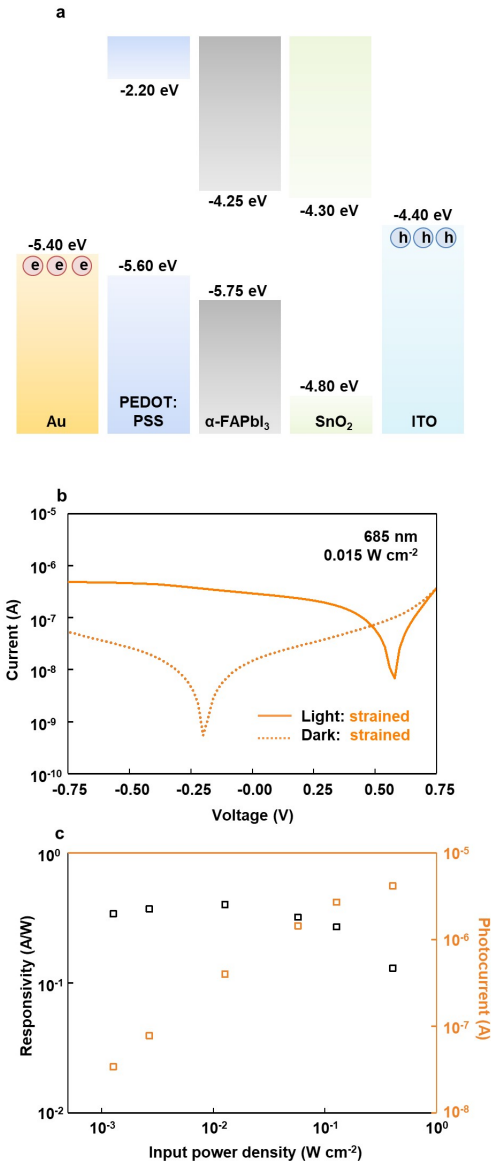
**Supplementary Fig. 14 | Stability investigation of the epitaxial and the removed  $\alpha$ -FAPbI<sub>3</sub>.** Images of the **a**, as-polished and the **b**, 24-hour aged epitaxial  $\alpha$ -FAPbI<sub>3</sub> thin film. The left half of the epitaxial  $\alpha$ -FAPbI<sub>3</sub> thin film is removed by a sandpaper while the right half of the epitaxial  $\alpha$ -FAPbI<sub>3</sub> thin film remains on the substrate. Removed  $\alpha$ -FAPbI<sub>3</sub> that is attached to the upper half of the sandpaper suffers from phase transition from black  $\alpha$  phase to yellow  $\delta$  phase after 24 hours. The epitaxial  $\alpha$ -FAPbI<sub>3</sub> thin film remains on the substrate is stable without phase transition. Results show the epitaxial stabilization of the epitaxial  $\alpha$ -FAPbI<sub>3</sub> thin film relies on the constraint from the substrate lattices.





1469  
 1470  
 1471  
 1472  
 1473  
 1474

**Supplementary Fig. 15 | Schematic band diagrams of photodetectors.** Left panel is the flat band diagram of the photodetector. Due to the compressive strain, the VBM of  $\alpha$ -FAPbI<sub>3</sub> at the interface will be pushed up and align better with the Au Fermi level (-5.4 eV), which allows better hole transfer from  $\alpha$ -FAPbI<sub>3</sub> to Au and therefore enhances the device performance.



1475

1476

1477

1478

1479

1480

1481

1482

**Supplementary Fig. 16 | Photodiode-type photodetector characterizations.** **a**, The band diagram of the photodetector. An Au/PEDOT:PSS/ $\alpha$ -FAPbI<sub>3</sub>/SnO<sub>2</sub>/ITO structure is used to build a photodiode. In this structure, the injection of external carriers under reverse bias is efficiently blocked due to the large energy barrier. **b**,  $I$ - $V$  curves of the photodetector. The dark current is reduced to  $\sim 10^{-8}$  A due to the diode structure. **c**, Responsivity and photocurrent of the photodetector under different illumination power levels. Results show that the responsivity is lower than 1 with the diode structure.

1483 **References**

1484

1485 1 Sun, M. *et al.* All-Inorganic Perovskite Nanowires-InGaZnO Heterojunction for  
1486 High-Performance Ultraviolet-Visible Photodetectors. *ACS Appl Mater Interfaces* **10**,  
1487 7231-7238, (2018).

1488 2 Chen, J. *et al.* Single-Crystal Thin Films of Cesium Lead Bromide Perovskite Epitaxially Grown  
1489 on Metal Oxide Perovskite (SrTiO<sub>3</sub>). *Journal of the American Chemical Society* **139**,  
1490 13525-13532, (2017).

1491 3 Oksenberg, E., Sanders, E., Popovitz-Biro, R., Houben, L. & Joselevich, E. Surface-Guided  
1492 CsPbBr<sub>3</sub> Perovskite Nanowires on Flat and Faceted Sapphire with Size-Dependent  
1493 Photoluminescence and Fast Photoconductive Response. *Nano Lett* **18**, 424-433, (2018).

1494 4 Wang, Y. *et al.* Nontrivial strength of van der Waals epitaxial interaction in soft perovskites.  
1495 *Physical Review Materials* **2**, 076002, (2018).

1496 5 Wang, Y. *et al.* High-Temperature Ionic Epitaxy of Halide Perovskite Thin Film and the Hidden  
1497 Carrier Dynamics. *Advanced Materials* **29**, (2017).

1498 6 Wang, L. *et al.* Unlocking the Single-Domain Epitaxy of Halide Perovskites. *Advanced*  
1499 *Materials Interfaces*, (2017).

1500 7 Li, X., Luo, Y., Holt, M. V., Cai, Z. & Fenning, D. P. Residual Nanoscale Strain in Cesium Lead  
1501 Bromide Perovskite Reduces Stability and Shifts Local Luminescence. *Chemistry of Materials*,  
1502 (2019).

1503 8 Wang, Y. *et al.* Defect-engineered epitaxial VO<sub>2</sub>±δ in strain engineering of heterogeneous soft  
1504 crystals. *Science Advances* **4**, eaar3679, (2018).

1505 9 Saidaminov, M. I. *et al.* Suppression of atomic vacancies via incorporation of isovalent small  
1506 ions to increase the stability of halide perovskite solar cells in ambient air. *Nature Energy*,  
1507 (2018).

1508 10 Zheng, X. *et al.* Improved Phase Stability of Formamidinium Lead Triiodide Perovskite by  
1509 Strain Relaxation. *ACS Energy Letters* **1**, 1014-1020, (2016).

1510 11 Shai, X. *et al.* Achieving ordered and stable binary metal perovskite via strain engineering.  
1511 *Nano Energy* **48**, 117-127, (2018).

1512 12 Tsai, H. *et al.* Light-induced lattice expansion leads to high-efficiency perovskite solar cells.  
1513 *Science* **360**, 67-70, (2018).

1514 13 Jones, T. W. *et al.* Lattice strain causes non-radiative losses in halide perovskites. *Energy &*  
1515 *Environmental Science* **12**, 596-606, (2019).

1516 14 Zhao, J. *et al.* Strained hybrid perovskite thin films and their impact on the intrinsic stability of  
1517 perovskite solar cells. *Science Advances* **3**, eaao5616, (2017).

1518 15 Zhu, C. *et al.* Strain engineering in perovskite solar cells and its impacts on carrier dynamics.  
1519 *Nature Communications* **10**, 815, (2019).

1520 16 Steele, J. A. *et al.* Thermal nonequilibrium of strained black CsPbI<sub>3</sub> thin films. *Science*,  
1521 eaax3878, (2019).

1522 17 Lü, X. *et al.* Enhanced Structural Stability and Photo Responsiveness of CH<sub>3</sub>NH<sub>3</sub>SnI<sub>3</sub>  
1523 Perovskite via Pressure-Induced Amorphization and Recrystallization. *Advanced Materials* **28**,  
1524 8663-8668, (2016).

1525 18 Liu, G. *et al.* Pressure-Induced Bandgap Optimization in Lead-Based Perovskites with  
1526 Prolonged Carrier Lifetime and Ambient Retainability. *Advanced Functional Materials* **27**,

1527 (2017).

1528 19 Liu, S. *et al.* Manipulating efficient light emission in two-dimensional perovskite crystals by  
1529 pressure-induced anisotropic deformation. *Science Advances* **5**, eaav9445, (2019).

1530 20 Ma, Z. *et al.* Pressure-induced emission of cesium lead halide perovskite nanocrystals. *Nature*  
1531 *Communications* **9**, 4506, (2018).

1532 21 Jaffe, A., Lin, Y., Mao, W. L. & Karunadasa, H. I. Pressure-induced metallization of the halide  
1533 perovskite (CH<sub>3</sub>NH<sub>3</sub>) PbI<sub>3</sub>. *Journal of the American Chemical Society* **139**, 4330-4333,  
1534 (2017).

1535 22 Han, Q. *et al.* Single Crystal Formamidinium Lead Iodide (FAPbI<sub>3</sub>): Insight into the Structural,  
1536 Optical, and Electrical Properties. *Advanced Materials* **28**, 2253-2258, (2016).

1537 23 Wang, W. F. *et al.* Growth of mixed-halide perovskite single crystals. *Crystengcomm* **20**,  
1538 1635-1643, (2018).

1539 24 Fang, Y., Dong, Q., Shao, Y., Yuan, Y. & Huang, J. Highly narrowband perovskite  
1540 single-crystal photodetectors enabled by surface-charge recombination. *Nature Photonics* **9**,  
1541 679, (2015).

1542 25 Saidaminov, M. I. *et al.* High-quality bulk hybrid perovskite single crystals within minutes by  
1543 inverse temperature crystallization. *Nature Communications* **6**, 7586, (2015).

1544 26 Lei, Y. *et al.* Controlled Homoepitaxial Growth of Hybrid Perovskites. *Advanced Materials* **30**,  
1545 1705992, (2018).

1546 27 Suryanarayana, C. & Norton, M. G. *X-ray diffraction: a practical approach*. (Springer Science  
1547 & Business Media, 2013).

1548 28 Birkholz, M. *Thin film analysis by X-ray scattering*. (John Wiley & Sons, 2006).

1549 29 Gubicza, J. *X-ray line profile analysis in materials science*. (IGI Global, 2014).

1550 30 Hartmann, J. M., Abbadie, A. & Favier, S. Critical thickness for plastic relaxation of SiGe on  
1551 Si(001) revisited. *Journal of Applied Physics* **110**, 083529, (2011).

1552 31 Steele, J. A. *et al.* Direct Laser Writing of  $\delta$ - to  $\alpha$ -Phase Transformation in Formamidinium  
1553 Lead Iodide. *ACS Nano* **11**, 8072-8083, (2017).

1554 32 Frank, O. *et al.* Raman 2D-Band Splitting in Graphene: Theory and Experiment. *ACS Nano* **5**,  
1555 2231-2239, (2011).

1556 33 Chen, J. *et al.* Probing Strain in Bent Semiconductor Nanowires with Raman Spectroscopy.  
1557 *Nano Letters* **10**, 1280-1286, (2010).

1558 34 Mohiuddin, T. M. G. *et al.* Uniaxial strain in graphene by Raman spectroscopy: Gpeak splitting,  
1559 Grüneisen parameters, and sample orientation. *Physical Review B* **79**, 205433, (2009).

1560 35 Quarti, C. *et al.* The Raman spectrum of the CH<sub>3</sub>NH<sub>3</sub>PbI<sub>3</sub> hybrid perovskite: interplay of  
1561 theory and experiment. *The journal of physical chemistry letters* **5**, 279-284, (2013).

1562 36 Pérez-Osorio, M. A. *et al.* Raman Spectrum of the Organic-Inorganic Halide Perovskite  
1563 CH<sub>3</sub>NH<sub>3</sub>PbI<sub>3</sub> from First Principles and High-Resolution Low-Temperature Raman  
1564 Measurements. *The Journal of Physical Chemistry C*, (2018).

1565 37 Pering, S. R. *et al.* Azetidinium lead iodide for perovskite solar cells. *Journal of Materials*  
1566 *Chemistry A* **5**, 20658-20665, (2017).

1567 38 Steele, J. A. *et al.* Direct Laser Writing of  $\delta$ -to  $\alpha$ -Phase Transformation in Formamidinium Lead  
1568 Iodide. *ACS nano*, (2017).

1569 39 Niemann, R. G. *et al.* Halogen Effects on Ordering and Bonding of CH<sub>3</sub>NH<sub>3</sub><sup>+</sup> in CH<sub>3</sub>NH<sub>3</sub>PbX<sub>3</sub>  
1570 (X = Cl, Br, I) Hybrid Perovskites: A Vibrational Spectroscopic Study. *The Journal of Physical*

1571 *Chemistry C* **120**, 2509-2519, (2016).

1572 40 Chen, T. *et al.* Entropy-driven structural transition and kinetic trapping in formamidinium lead  
1573 iodide perovskite. *Science advances* **2**, e1601650, (2016).

1574 41 Taylor, V. C. A. *et al.* Investigating the Role of the Organic Cation in Formamidinium Lead  
1575 Iodide Perovskite Using Ultrafast Spectroscopy. *The Journal of Physical Chemistry Letters* **9**,  
1576 895-901, (2018).

1577 42 Govinda, S. *et al.* Critical Comparison of FAPbX<sub>3</sub> and MAPbX<sub>3</sub> (X = Br and Cl): How Do They  
1578 Differ? *The Journal of Physical Chemistry C* **122**, 13758-13766, (2018).

1579 43 Nakada, K., Matsumoto, Y., Shimoi, Y., Yamada, K. & Furukawa, Y. Temperature-Dependent  
1580 Evolution of Raman Spectra of Methylammonium Lead Halide Perovskites, CH<sub>3</sub>NH<sub>3</sub>PbX<sub>3</sub> (X  
1581 = I, Br). *Molecules* **24**, 626, (2019).

1582 44 Ledinský, M. *et al.* Raman Spectroscopy of Organic–Inorganic Halide Perovskites. *The Journal*  
1583 *of Physical Chemistry Letters* **6**, 401-406, (2015).

1584 45 Li, D. *et al.* Size-dependent phase transition in methylammonium lead iodide perovskite  
1585 microplate crystals. *Nature Communications* **7**, 11330, (2016).

1586 46 Sarmah, S. P. *et al.* Double Charged Surface Layers in Lead Halide Perovskite Crystals. *Nano*  
1587 *Letters* **17**, 2021-2027, (2017).

1588 47 Kanemitsu, Y. Luminescence spectroscopy of lead-halide perovskites: materials properties  
1589 and application as photovoltaic devices. *Journal of Materials Chemistry C* **5**, 3427-3437,  
1590 (2017).

1591 48 Xie, L.-Q. *et al.* Understanding the Cubic Phase Stabilization and Crystallization Kinetics in  
1592 Mixed Cations and Halides Perovskite Single Crystals. *Journal of the American Chemical*  
1593 *Society* **139**, 3320-3323, (2017).

1594 49 Wenger, B. *et al.* Consolidation of the optoelectronic properties of CH<sub>3</sub>NH<sub>3</sub>PbBr<sub>3</sub> perovskite  
1595 single crystals. *Nature communications* **8**, 590, (2017).

1596 50 Gershon, T. *et al.* Relationship between Cu<sub>2</sub>ZnSnS<sub>4</sub> quasi donor-acceptor pair density and  
1597 solar cell efficiency. *Applied Physics Letters* **103**, 193903, (2013).

1598 51 Nayak, P. *et al.* The impact of Bi<sup>3+</sup> heterovalent doping in organic-inorganic metal halide  
1599 perovskite crystals. *Journal of the American Chemical Society*, (2017).

1600 52 Mičić, O. I. *et al.* Size-Dependent Spectroscopy of InP Quantum Dots. *The Journal of Physical*  
1601 *Chemistry B* **101**, 4904-4912, (1997).

1602 53 Wehrenfennig, C., Liu, M., Snaith, H. J., Johnston, M. B. & Herz, L. M. Homogeneous  
1603 Emission Line Broadening in the Organo Lead Halide Perovskite CH<sub>3</sub>NH<sub>3</sub>PbI<sub>3-x</sub>Cl<sub>x</sub>. *The*  
1604 *Journal of Physical Chemistry Letters* **5**, 1300-1306, (2014).

1605 54 Yan, Z.-Z., Jiang, Z.-H., Lu, J.-P. & Ni, Z.-H. Interfacial charge transfer in WS<sub>2</sub>  
1606 monolayer/CsPbBr<sub>3</sub> microplate heterostructure. *Frontiers of Physics* **13**, 138115, (2018).

1607 55 Zi-Yu, P., Jian-Long, X., Jing-Yue, Z., Xu, G. & Sui-Dong, W. Solution-Processed High-  
1608 Performance Hybrid Photodetectors Enhanced by Perovskite/MoS<sub>2</sub> Bulk Heterojunction.  
1609 *Advanced Materials Interfaces* **0**, 1800505, (2018).

1610 56 Li, H., Zheng, X., Liu, Y., Zhang, Z. & Jiang, T. Ultrafast interfacial energy transfer and  
1611 interlayer excitons in the monolayer WS<sub>2</sub>/CsPbBr<sub>3</sub> quantum dot heterostructure. *Nanoscale*  
1612 **10**, 1650-1659, (2018).

1613 57 Zhu, H. *et al.* Interfacial Charge Transfer Circumventing Momentum Mismatch at  
1614 Two-Dimensional van der Waals Heterojunctions. *Nano Letters* **17**, 3591-3598, (2017).

1615 58 Rigosi, A. F., Hill, H. M., Li, Y., Chernikov, A. & Heinz, T. F. Probing Interlayer Interactions in  
1616 Transition Metal Dichalcogenide Heterostructures by Optical Spectroscopy: MoS<sub>2</sub>/WS<sub>2</sub> and  
1617 MoSe<sub>2</sub>/WSe<sub>2</sub>. *Nano Letters* **15**, 5033-5038, (2015).

1618 59 Comin, R. *et al.* Structural, optical, and electronic studies of wide-bandgap lead halide  
1619 perovskites. *Journal of Materials Chemistry C* **3**, 8839-8843, (2015).

1620 60 Rudin, S., Reinecke, T. L. & Segall, B. Temperature-dependent exciton linewidths in  
1621 semiconductors. *Physical Review B* **42**, 11218-11231, (1990).

1622 61 Wright, A. D. *et al.* Electron–phonon coupling in hybrid lead halide perovskites. *Nature*  
1623 *Communications* **7**, 11755, (2016).

1624 62 Lee, J., Koteles, E. S. & Vassell, M. O. Luminescence linewidths of excitons in GaAs quantum  
1625 wells below 150 K. *Physical Review B* **33**, 5512-5516, (1986).

1626 63 Dar, M. I. *et al.* Origin of unusual bandgap shift and dual emission in organic-inorganic lead  
1627 halide perovskites. *Science Advances* **2**, (2016).

1628 64 Ni, L. *et al.* Real-Time Observation of Exciton–Phonon Coupling Dynamics in Self-Assembled  
1629 Hybrid Perovskite Quantum Wells. *ACS Nano* **11**, 10834-10843, (2017).

1630 65 Thirumal, K. *et al.* Morphology-Independent Stable White-Light Emission from Self-Assembled  
1631 Two-Dimensional Perovskites Driven by Strong Exciton–Phonon Coupling to the Organic  
1632 Framework. *Chemistry of Materials* **29**, 3947-3953, (2017).

1633 66 Ferreira, A. C. *et al.* Elastic Softness of Hybrid Lead Halide Perovskites. *Physical Review*  
1634 *Letters* **121**, 085502, (2018).

1635 67 Zienkiewicz, O. C., Taylor, R. L., Nithiarasu, P. & Zhu, J. *The finite element method*. Vol. 3  
1636 (McGraw-hill London, 1977).

1637 68 Katan, C., Mohite, A. D. & Even, J. Entropy in halide perovskites. *Nature materials* **17**, 377,  
1638 (2018).

1639 69 Matthews, J. W. & Blakeslee, A. E. Defects in epitaxial multilayers: I. Misfit dislocations.  
1640 *Journal of Crystal Growth* **27**, 118-125, (1974).

1641 70 People, R. & Bean, J. C. Calculation of critical layer thickness versus lattice mismatch for  
1642 GeSi<sub>1-x</sub>/Si strained-layer heterostructures. *Applied Physics Letters* **47**, 322-324, (1985).

1643 71 Kosyachenko, L. A. *Solar Cells: New Aspects and Solutions*. (BoD–Books on Demand,  
1644 2011).

1645 72 Jiang, S. *et al.* Phase Transitions of Formamidinium Lead Iodide Perovskite under Pressure.  
1646 *Journal of the American Chemical Society*, (2018).

1647 73 Chen, Z. *et al.* Remote Phononic Effects in Epitaxial Ruddlesden–Popper Halide Perovskites.  
1648 *The Journal of Physical Chemistry Letters*, 6676-6682, (2018).

1649 74 Ge, C. *et al.* Ultralow Thermal Conductivity and Ultrahigh Thermal Expansion of Single-Crystal  
1650 Organic–Inorganic Hybrid Perovskite CH<sub>3</sub>NH<sub>3</sub>PbX<sub>3</sub> (X = Cl, Br, I). *The Journal of Physical*  
1651 *Chemistry C* **122**, 15973-15978, (2018).

1652 75 Yin, W.-J., Yang, J.-H., Kang, J., Yan, Y. & Wei, S.-H. Halide perovskite materials for solar  
1653 cells: a theoretical review. *Journal of Materials Chemistry A* **3**, 8926-8942, (2015).

1654 76 Wang, C., Ecker, B. R., Wei, H., Huang, J. & Gao, Y. Environmental Surface Stability of the  
1655 MAPbBr<sub>3</sub> Single Crystal. *The Journal of Physical Chemistry C* **122**, 3513-3522, (2018).

1656 77 Shi, D. *et al.* Low trap-state density and long carrier diffusion in organolead trihalide perovskite  
1657 single crystals. *Science* **347**, 519-522, (2015).

1658 78 Dong, Q. *et al.* Electron-hole diffusion lengths > 175  $\mu\text{m}$  in solution-grown  $\text{CH}_3\text{NH}_3\text{PbI}_3$  single  
1659 crystals. *Science* **347**, 967-970, (2015).

1660 79 Wu, Z., Yao, W., London, A. E., Azoulay, J. D. & Ng, T. N. Elucidating the Detectivity Limits in  
1661 Shortwave Infrared Organic Photodiodes. *Advanced Functional Materials* **28**, 1800391,  
1662 (2018).

1663 80 Stolterfoht, M., Armin, A., Philippa, B. & Neher, D. The Role of Space Charge Effects on the  
1664 Competition between Recombination and Extraction in Solar Cells with Low-Mobility  
1665 Photoactive Layers. *The Journal of Physical Chemistry Letters* **7**, 4716-4721, (2016).

1666 81 Mihailetchi, V. D., Xie, H. X., de Boer, B., Koster, L. J. A. & Blom, P. W. M. Charge Transport  
1667 and Photocurrent Generation in Poly(3-hexylthiophene): Methanofullerene  
1668 Bulk-Heterojunction Solar Cells. *Advanced Functional Materials* **16**, 699-708, (2006).

1669 82 Herz, L. M. Charge-Carrier Mobilities in Metal Halide Perovskites: Fundamental Mechanisms  
1670 and Limits. *ACS Energy Letters* **2**, 1539-1548, (2017).

1671 83 Chen, B., Yang, M., Priya, S. & Zhu, K. Origin of J-V Hysteresis in Perovskite Solar Cells. *The*  
1672 *Journal of Physical Chemistry Letters* **7**, 905-917, (2016).

1673 84 Wei, J. *et al.* Hysteresis Analysis Based on the Ferroelectric Effect in Hybrid Perovskite Solar  
1674 Cells. *The Journal of Physical Chemistry Letters* **5**, 3937-3945, (2014).

1675 85 Tress, W. *et al.* Understanding the rate-dependent J-V hysteresis, slow time component, and  
1676 aging in  $\text{CH}_3\text{NH}_3\text{PbI}_3$  perovskite solar cells: the role of a compensated electric field. *Energy &*  
1677 *Environmental Science* **8**, 995-1004, (2015).

1678 86 Bain, A. K. & Chand, P. *Ferroelectrics: Principles and Applications*. (John Wiley & Sons,  
1679 2017).

1680 87 Li, C., Guerrero, A., Huettner, S. & Bisquert, J. Unravelling the role of vacancies in lead halide  
1681 perovskite through electrical switching of photoluminescence. *Nature Communications* **9**,  
1682 5113, (2018).

1683 88 Li, C. *et al.* Real-Time Observation of Iodide Ion Migration in Methylammonium Lead Halide  
1684 Perovskites. *Small* **13**, 1701711, (2017).

1685 89 Shao, Y. *et al.* Grain boundary dominated ion migration in polycrystalline organic-inorganic  
1686 halide perovskite films. *Energy & Environmental Science* **9**, 1752-1759, (2016).

1687 90 Lee, J.-W., Kim, S.-G., Yang, J.-M., Yang, Y. & Park, N.-G. Verification and mitigation of ion  
1688 migration in perovskite solar cells. *APL Materials* **7**, 041111, (2019).

1689 91 Yun, J. S. *et al.* Critical Role of Grain Boundaries for Ion Migration in Formamidinium and  
1690 Methylammonium Lead Halide Perovskite Solar Cells. *Advanced Energy Materials* **6**, 1600330,  
1691 (2016).

1692 92 Xing, J. *et al.* Ultrafast ion migration in hybrid perovskite polycrystalline thin films under light  
1693 and suppression in single crystals. *Physical Chemistry Chemical Physics* **18**, 30484-30490,  
1694 (2016).

1695 93 Kang, K. *et al.* High-Performance Solution-Processed Organo-Metal Halide Perovskite  
1696 Unipolar Resistive Memory Devices in a Cross-Bar Array Structure. *Advanced Materials* **31**,  
1697 1804841, (2019).

1698 94 Hu, Y. *et al.* Ultrathin  $\text{Cs}_3\text{Bi}_2\text{I}_9$  Nanosheets as an Electronic Memory Material for Flexible  
1699 Memristors. *Advanced Materials Interfaces* **4**, (2017).

1700 95 Calado, P. *et al.* Evidence for ion migration in hybrid perovskite solar cells with minimal  
1701 hysteresis. *Nature Communications* **7**, 13831, (2016).

1702 96 Zimmermann, E. *et al.* Characterization of perovskite solar cells: Towards a reliable  
1703 measurement protocol. *APL Materials* **4**, 091901, (2016).

1704 97 Ayers, J. E., Kujofsa, T., Rago, P. & Raphael, J. *Heteroepitaxy of semiconductors: theory,*  
1705 *growth, and characterization.* (CRC press, 2016).

1706 98 Pohl, U. W. *Epitaxy of Semiconductors: Introduction to Physical Principles.* (Springer  
1707 Science & Business Media, 2013).

1708 99 Ball, J. M. & Petrozza, A. Defects in perovskite-halides and their effects in solar cells. *Nature*  
1709 *Energy* **1**, 16149, (2016).

1710 100 Liu, Z. *et al.* Gas-solid reaction based over one-micrometer thick stable perovskite films for  
1711 efficient solar cells and modules. *Nature Communications* **9**, 3880, (2018).

1712 101 Wang, K.-L. *et al.* Tailored Phase Transformation of CsPbI<sub>2</sub>Br Films by Copper(II) Bromide for  
1713 High-Performance All-Inorganic Perovskite Solar Cells. *Nano Letters* **19**, 5176-5184, (2019).

1714 102 Wang, L. *et al.* A Eu(3+)-Eu(2+) ion redox shuttle imparts operational durability to Pb-I  
1715 perovskite solar cells. *Science* **363**, 265-270, (2019).

1716 103 Zhao, Y. *et al.* Perovskite seeding growth of formamidinium-lead-iodide-based perovskites for  
1717 efficient and stable solar cells. *Nature Communications* **9**, 1607, (2018).

1718 104 Yang, D. *et al.* High efficiency planar-type perovskite solar cells with negligible hysteresis  
1719 using EDTA-complexed SnO<sub>2</sub>. *Nature Communications* **9**, 3239, (2018).

1720 105 Wu, W.-Q. *et al.* Bilateral alkylamine for suppressing charge recombination and improving  
1721 stability in blade-coated perovskite solar cells. *Science Advances* **5**, eaav8925, (2019).

1722 106 Feng, J. *et al.* Single-crystalline layered metal-halide perovskite nanowires for ultrasensitive  
1723 photodetectors. *Nature Electronics* **1**, 404-410, (2018).

1724 107 Kong, W. *et al.* Organic Monomolecular Layers Enable Energy-Level Matching for Efficient  
1725 Hole Transporting Layer Free Inverted Perovskite Solar Cells. *ACS Nano* **13**, 1625-1634,  
1726 (2019).

1727 108 Liu, X. *et al.* 20.7% highly reproducible inverted planar perovskite solar cells with enhanced fill  
1728 factor and eliminated hysteresis. *Energy & Environmental Science* **12**, 1622-1633, (2019).

1729 109 Saidaminov, M. I. *et al.* High-quality bulk hybrid perovskite single crystals within minutes by  
1730 inverse temperature crystallization. *Nature communications* **6**, (2015).

1731 110 Leijtens, T. *et al.* Carrier trapping and recombination: the role of defect physics in enhancing  
1732 the open circuit voltage of metal halide perovskite solar cells. *Energy & Environmental Science*  
1733 **9**, 3472-3481, (2016).

1734 111 Brenes, R. *et al.* Metal Halide Perovskite Polycrystalline Films Exhibiting Properties of Single  
1735 Crystals. *Joule* **1**, 155-167, (2017).

1736 112 Yao, W. *et al.* Organic Bulk Heterojunction Infrared Photodiodes for Imaging Out to 1300 nm.  
1737 *ACS Applied Electronic Materials*, (2019).

1738 113 Street, R. A., Yang, Y., Thompson, B. C. & McCulloch, I. Capacitance Spectroscopy of Light  
1739 Induced Trap States in Organic Solar Cells. *The Journal of Physical Chemistry C* **120**,  
1740 22169-22178, (2016).

1741 114 Hwang, T. *et al.* Electronic Traps and Their Correlations to Perovskite Solar Cell Performance  
1742 via Compositional and Thermal Annealing Controls. *ACS Applied Materials & Interfaces* **11**,  
1743 6907-6917, (2019).

1744 115 Kovalenko, A., Pospisil, J., Zmeskal, O., Krajcovic, J. & Weiter, M. Ionic origin of a negative  
1745 capacitance in lead halide perovskites. *physica status solidi (RRL) – Rapid Research Letters*



1746 11, 1600418, (2017).

1747 116 Khan, M. T., Salado, M., Almohammed, A., Kazim, S. & Ahmad, S. Elucidating the Impact of  
1748 Charge Selective Contact in Halide Perovskite through Impedance Spectroscopy. *Advanced*  
1749 *Materials Interfaces* **0**, 1901193, (2019).

1750 117 Han, C. *et al.* Unraveling surface and bulk trap states in lead halide perovskite solar cells using  
1751 impedance spectroscopy. *Journal of Physics D: Applied Physics* **51**, 095501, (2018).

1752 118 Samiee, M. *et al.* Defect density and dielectric constant in perovskite solar cells. *Applied*  
1753 *Physics Letters* **105**, 153502, (2014).

1754 119 Yi, C. *et al.* Entropic stabilization of mixed A-cation ABX<sub>3</sub> metal halide perovskites for high  
1755 performance perovskite solar cells. *Energy & Environmental Science* **9**, 656-662, (2016).

1756 120 Yang, W. S. *et al.* High-performance photovoltaic perovskite layers fabricated through  
1757 intramolecular exchange. *Science* **348**, 1234-1237, (2015).

1758 121 Jeon, N. J. *et al.* Compositional engineering of perovskite materials for high-performance solar  
1759 cells. *Nature* **517**, 476-480, (2015).

1760 122 Lee, J.-W. *et al.* 2D perovskite stabilized phase-pure formamidinium perovskite solar cells.  
1761 *Nature Communications* **9**, 3021, (2018).

1762 123 Yuan, S. *et al.* NbF<sub>5</sub>: A Novel  $\alpha$ -Phase Stabilizer for FA-Based Perovskite Solar Cells with  
1763 High Efficiency. *Advanced Functional Materials* **0**, 1807850, (2019).

1764 124 Fu, Y. *et al.* Stabilization of the metastable lead iodide perovskite phase via surface  
1765 functionalization. *Nano letters* **17**, 4405-4414, (2017).

1766 125 Gu, L. *et al.* Significantly improved black phase stability of FAPbI<sub>3</sub> nanowires via spatially  
1767 confined vapor phase growth in nanoporous templates. *Nanoscale* **10**, 15164-15172, (2018).

1768 126 Zhou, Y., Kwun, J., Garcés, H. F., Pang, S. & Padture, N. P. Observation of phase-retention  
1769 behavior of the HC (NH<sub>2</sub>)<sub>2</sub>PbI<sub>3</sub> black perovskite polymorph upon mesoporous TiO<sub>2</sub>  
1770 scaffolds. *Chemical Communications* **52**, 7273-7275, (2016).

1771 127 Li, B. *et al.* Surface passivation engineering strategy to fully-inorganic cubic CsPbI<sub>3</sub>  
1772 perovskites for high-performance solar cells. *Nat Commun* **9**, 1076, (2018).

1773 128 Ma, S. *et al.* Strain-Mediated Phase Stabilization: A New Strategy for Ultrastable  $\alpha$ -CsPbI<sub>3</sub>  
1774 Perovskite by Nanoconfined Growth. *Small* **0**, 1900219, (2019).

1775 129 Liu, M. *et al.* Lattice anchoring stabilizes solution-processed semiconductors. *Nature*, (2019).

1776 130 Lee, J. H. *et al.* Epitaxial Stabilization of a New Multiferroic Hexagonal Phase of TbMnO<sub>3</sub> Thin  
1777 Films. *Advanced Materials* **18**, 3125-3129, (2006).

1778 131 Vaillonis, A., Siemons, W. & Koster, G. Room temperature epitaxial stabilization of a  
1779 tetragonal phase in ARuO<sub>3</sub> (A=Ca and Sr) thin films. *Applied Physics Letters* **93**, 051909,  
1780 (2008).

1781 132 Xu, Z., Salvador, P. & Kitchin, J. R. First-Principles Investigation of the Epitaxial Stabilization of  
1782 Oxide Polymorphs: TiO<sub>2</sub> on (Sr,Ba)TiO<sub>3</sub>. *ACS Applied Materials & Interfaces* **9**, 4106-4118,  
1783 (2017).

1784 133 Liu, B., Long, M., Cai, M.-Q., Hao, X. & Yang, J. Ferroelectric Polarization in CsPbI<sub>3</sub>/CsSnI<sub>3</sub>  
1785 Perovskite Heterostructure. *The Journal of Physical Chemistry C*, (2018).

1786 134 Ahmadi, M., Wu, T. & Hu, B. A Review on Organic-Inorganic Halide Perovskite  
1787 Photodetectors: Device Engineering and Fundamental Physics. *Advanced Materials*, (2017).

1788 135 Yang, Z. *et al.* High-Performance Single-Crystalline Perovskite Thin-Film Photodetector.  
1789 *Advanced Materials*, (2018).

1790 136 Zhao, Y., Li, C. & Shen, L. Recent advances on organic-inorganic hybrid perovskite  
1791 photodetectors with fast response. *InfoMat* **0**, (2019).  
1792 137 Li, Y. & Yang, K. High-throughput computational design of organic-inorganic hybrid halide  
1793 semiconductors beyond perovskites for optoelectronics. *Energy & Environmental Science* **12**,  
1794 2233-2243, (2019).  
1795 138 Haihua, Z. *et al.* A Two-Dimensional Ruddlesden-Popper Perovskite Nanowire Laser Array  
1796 based on Ultrafast Light-Harvesting Quantum Wells. *Angewandte Chemie International Edition*  
1797 **0**, 7748-7752, (2018).  
1798 139 Ye, F. *et al.* High-Quality Cuboid CH<sub>3</sub>NH<sub>3</sub>PbI<sub>3</sub> Single Crystals for High Performance X-Ray  
1799 and Photon Detectors. *Advanced Functional Materials* **0**, 1806984, (2018).  
1800 140 Ji, L., Hsu, H.-Y., Lee, J., Bard, A. J. & Yu, E. T. High performance photodetectors based on  
1801 solution-processed epitaxial grown hybrid halide perovskites. *Nano letters*, (2018).  
1802 141 Zhang, Y. *et al.* Trash into Treasure:  $\delta$ -FAPbI<sub>3</sub> Polymorph Stabilized MAPbI<sub>3</sub> Perovskite with  
1803 Power Conversion Efficiency beyond 21%. *Advanced Materials* **0**, 1707143, (2018).  
1804